4

Biomechanics

Joseph L. Palladino, PhD, and Roy B. Davis III, PhD

AT THE CONCLUSION OF THIS CHAPTER, STUDENTS WILL BE ABLE TO:

- Understand the application of engineering kinematic relations to biomechanical problems.
- Understand the application of engineering kinetic relations to biomechanical problems.
- Understand the application of engineering mechanics of materials to biological structures.
- Use MATLAB to write and solve biomechanical static and dynamic equations.
- Use Simulink to study viscoelastic properties of biological tissues.

- Understand how kinematic equations of motion are used in clinical analysis of human gait.
- Understand how kinetic equations of motion are used in clinical analysis of human gait.
- Explain how biomechanics applied to human gait is used to quantify pathological conditions, to suggest surgical and clinical treatments, and to quantify their effectiveness.
- Understand basic rheology of biological fluids.
- Understand the development of models that describe blood vessel mechanics.

- Understand basic heart mechanics.
- Explain how biomechanics applied to the cardiovascular system is used to quantify the effectiveness of the heart as a pump, to study heart-vessel interaction, and to develop clinical applications.

4.1 INTRODUCTION

Biomechanics combines engineering and the life sciences by applying principles from classical mechanics to the study of living systems. This relatively new field covers a broad range of topics, including strength of biological materials, biofluid mechanics in the cardio-vascular and respiratory systems, material properties and interactions of medical implants and the body, heat and mass transfer into biological tissues, biocontrol systems regulating metabolism or voluntary motion, and kinematics and kinetics applied to study human gait. The great breadth of the field of biomechanics arises from the complexities and variety of biological organisms and systems.

The goals of this chapter are twofold: to apply basic engineering principles to biological structures and to develop clinical applications. Section 4.2 provides a review of concepts from introductory statics and dynamics. Section 4.3 presents concepts from mechanics of material that are fundamental for engineers and accessible to those with only a statics/dynamics background. Section 4.4 introduces viscoelastic complexities characteristic of biological materials, with the concepts further applied in Section 4.5. The last two sections bring all of this information together in two "real-world" biomechanics applications: human gait analysis and cardiovascular dynamics. The human body is a complex machine, with the skeletal system and ligaments forming the framework and the muscles and tendons serving as the motors and cables. Human gait biomechanics may be viewed as a structure (skeleton) composed of levers (bones) with pivots (joints) that move as the result of net forces produced by pairs of agonist and antagonist muscles, a concept with origins as early as 1680, as depicted in Figure 4.1 from Borelli's *De Motu Animalium* (*On the Motion of Animals*). Consequently, the strength of the structure and the action of muscles will be of fundamental importance. Using a similar functional model, the cardiovascular system may be viewed as a complex pump (heart) pumping a complex fluid (blood) into a complex set of pipes (blood vessels). An extensive suggested reading list for both gait and cardiovascular dynamics permits the reader to go beyond the very introductory nature of this textbook.

The discipline of mechanics has a long history. For lack of more ancient records, the history of mechanics starts with the ancient Greeks and Aristotle (384–322 BC). Hellenic mechanics devised a correct concept of statics, but those of dynamics, fundamental in living systems, did not begin until the end of the Middle Ages and the beginning of the modern era. Starting in the sixteenth century, the field of dynamics advanced rapidly with work by Kepler, Galileo, Descartes, Huygens, and Newton. Dynamic laws were subsequently codified by Euler, LaGrange, and LaPlace (see *A History of Mechanics* by Dugas).
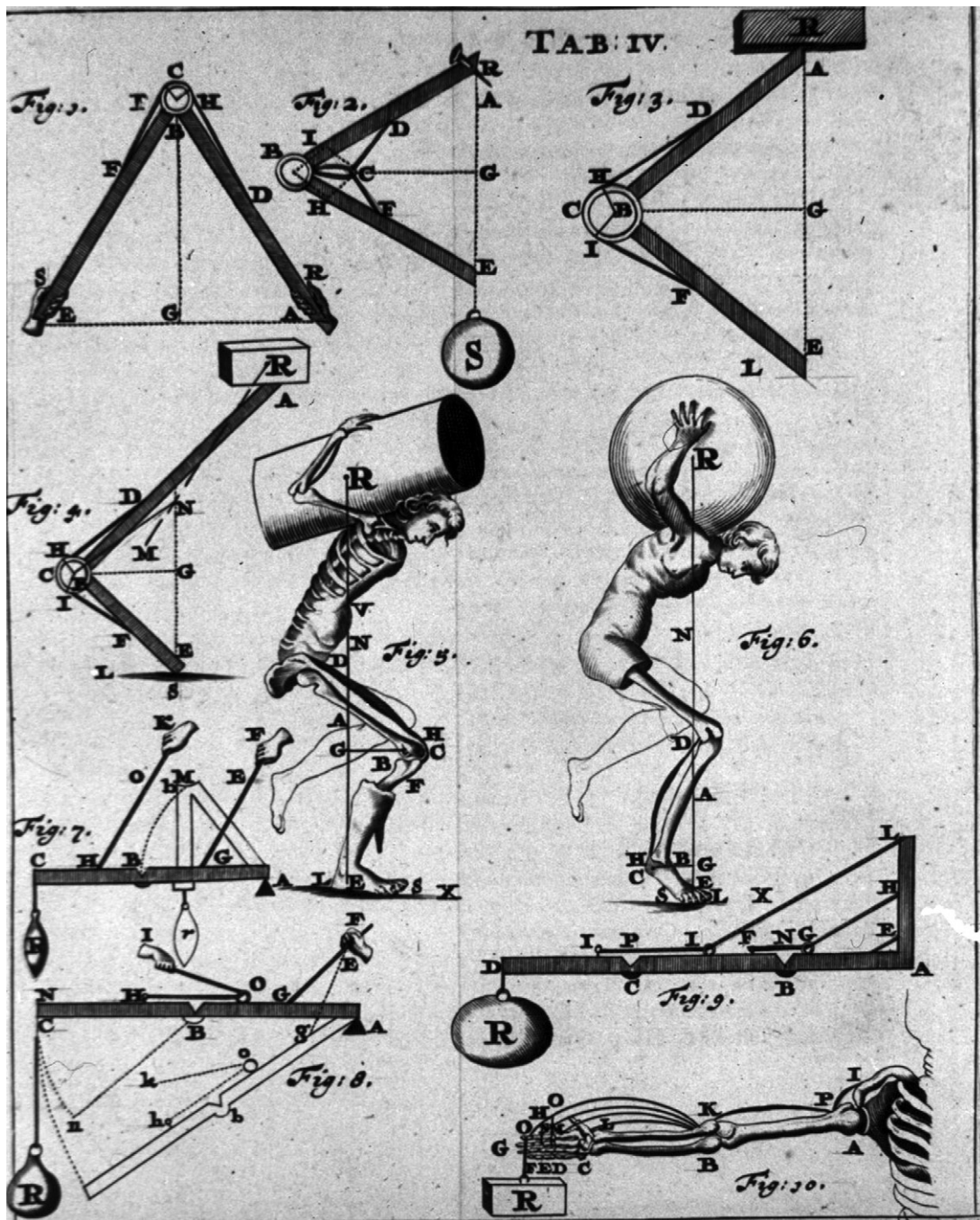
FIGURE 4.1 Plate reproduced from Borelli's *De Motu Animalium*, showing animal (human) motion resulting from the action of muscle pairs on bones, serving as levers, allowed to move at joints. *From* Images from the History of Medicine (IHM), *National Library of Medicine, National Institutes of Health,* http://www.nlm.nih.gov/hmd/ihm/.

In Galileo's *Two New Sciences* (1638), the subtitle *Attenenti all Mecanica & i Movimenti Locali* (*Pertaining to Mechanics and Local Motions*) refers to force, motion, and strength of materials. Since then, "mechanics" has been extended to describe the forces and motions of any system, ranging from quanta, atoms, molecules, gases, liquids, solids, structures, stars, and galaxies. The biological world is consequently a natural object for the study of mechanics.

The relatively new field of biomechanics applies mechanical principles to the study of living systems. The eminent professor of biomechanics Dr. Y. C. Fung describes the role of biomechanics in biology, physiology, and medicine as follows:

> Physiology can no more be understood without biomechanics than an airplane can without aerodynamics. For an airplane, mechanics enables us to design its structure and predict its performance. For an organ, biomechanics helps us to understand its normal function, predict changes due to alteration, and propose methods of artificial intervention. Thus, diagnosis, surgery, and prosthesis are closely associated with biomechanics.[1]

Clearly, biomechanics is essential to assessing and improving human health.

The following is a brief list of biomechanical milestones, especially those related to the topics in this chapter:

- **Galen of Pergamon (129–199)** Published extensively in medicine, including *De Motu Muscularum* (*On the Movements of Muscles*). He realized that motion requires muscle contraction.
- **Leonardo da Vinci (1452–1519)** Made the first accurate descriptions of ball-and-socket joints, such as the shoulder and hip, calling the latter the "*polo dell'omo*" (pole of man). His drawings depicted mechanical force acting along the line of muscle filaments.
- **Andreas Vesalius (1514–1564)** Published *De Humani Corporis Fabrica* (*The Fabric of the Human Body*). Based on human cadaver dissections, his work led to a more accurate anatomical description of human musculature than Galen's and demonstrated that motion results from the contraction of muscles that shorten and thicken.
- **Galileo Galilei (1564–1642)** Studied medicine and physics, integrated measurement and observation in science, and concluded that mathematics is an essential tool of science. His analyses included the biomechanics of jumping and the gait analysis of horses and insects, as well as dimensional analysis of animal bones.
- **Santorio Santorio (1561–1636)** Used Galileo's method of measurement and analysis and found that the human body changes weight with time. This observation led to the study of metabolism and, thereby, ushered in the scientific study of medicine.
- **William Harvey (1578–1657)** Developed an experimental basis for the modern circulation concept of a closed path between arteries and veins. The structural basis, the capillary, was discovered by Malpighi in 1661.
- **Giovanni Borelli (1608–1679)** A mathematician who studied body dynamics, muscle contraction, animal movement, and motion of the heart and intestines. He published *De Motu Animalium* (*On the Motion of Animals*) in 1680.

---

[1]*Biomechanics: Mechanical Properties of Living Tissues,* 2nd ed., Y. C. Fung, 1993.

- **Jan Swammerdam (1637–1680)** Introduced the nerve-muscle preparation, stimulating muscle contraction by pinching the attached nerve in the frog leg. He also showed that muscles contract with little change in volume, refuting the previous belief that muscles contract when "animal spirits" fill them, causing bulging.
- **Robert Hooke (1635–1703)** Devised Hooke's Law, relating the stress and elongation of elastic materials, and used the term "cell" in biology.
- **Isaac Newton (1642–1727)** Not known for biomechanics work, but he developed calculus, the classical laws of motion, and the constitutive equation for viscous fluid, all of which are fundamental to biomechanics.
- **Nicholas André (1658–1742)** Coined the term "orthopaedics" at the age of 80 and believed that muscular imbalances cause skeletal deformities.
- **Stephen Hales (1677–1761)** Was likely the first to measure blood pressure, as described in his book *Statistical Essays: Containing Haemostaticks, or an Account of Some Hydraulick and Hydrostatical Experiments Made on the Blood and Blood-Vessels of Animals; etc.*, in 1733.
- **Leonard Euler (1707–1783)** Generalized Newton's laws of motion to continuum representations that are used extensively to describe rigid body motion, and studied pulse waves in arteries.
- **Thomas Young (1773–1829)** Studied vibrations and voice, wave theory of light and vision, and devised Young's modulus of elasticity.
- **Ernst Weber (1795–1878) and Eduard Weber (1806–1871)** Published *Die Mechanik der meschlichen Gerwerkzeuge* (*On the Mechanics of the Human Gait Tools*) in 1836, pioneering the scientific study of human gait.
- **Hermann von Helmholtz (1821–1894)** Studied an immense array of topics, including optics, acoustics, thermodynamics, electrodynamics, physiology, and medicine, including ophthalmoscopy, fluid mechanics, nerve conduction speed, and the heat of muscle contraction.
- **Etienne Marey (1830–1904)** Analyzed the motion of horses, birds, insects, fish, and humans. His inventions included force plates to measure ground reaction forces and the "*Chronophotographe a pellicule*," or motion picture camera.
- **Wilhelm Braune and Otto Fischer (research conducted from 1895–1904)** Published *Der Gang des Menschen* (*The Human Gait*), containing the mathematical analysis of human gait and introducing methods still in use. They invented "cyclography" (now called interrupted-light photography with active markers), pioneered the use of multiple cameras to reconstruct 3-D motion data, and applied Newtonian mechanics to estimate joint forces and limb accelerations.

4.2 BASIC MECHANICS

This section reviews some of the main points from any standard introductory mechanics (statics and dynamics) course. Good references abound, such as *Engineering Mechanics* by Merriam and Kraige (2008). A review of vector mathematics is followed by matrix coordinate transformations, a topic new to some students. Euler's equations of motion (see Section 4.2.5) may also be new material. For both topics, *Principles of Dynamics* by Greenwood provides a comprehensive reference.
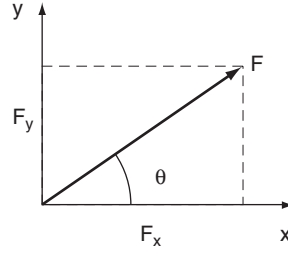
FIGURE 4.2   Two-dimensional representation of vector **F**.

4.2.1 Vector Mathematics

Forces may be written in terms of scalar components and unit vectors, of magnitude equal to one, or in polar form with magnitude and direction. Figure 4.2 shows that the two-dimensional vector **F** is composed of the **i** component, F_x, in the x-direction, and the **j** component, F_y, in the y-direction, or

$$\mathbf{F} = F_x\mathbf{i} + F_y\mathbf{j} \tag{4.1}$$

as in $20\mathbf{i} + 40\mathbf{j}$ lb. In this chapter, vectors are set in bold type. This same vector may be written in polar form in terms of the vector's magnitude $|F|$, also called the *norm*, and the vector's angle of orientation, θ:

$$|F| = \sqrt{F_x^2 + F_y^2} \tag{4.2}$$

$$\theta = \arctan\frac{F_y}{F_x} \tag{4.3}$$

yielding $|F| = 44.7$ lb and $\theta = 63.4°$. Vectors are similarly represented in three dimensions in terms of their **i**, **j**, and **k** components:

$$\mathbf{F} = F_x\mathbf{i} + F_y\mathbf{j} + F_z\mathbf{k} \tag{4.4}$$

with **k** in the z-direction.

Often, a vector's magnitude and two points along its line of action are known. Consider the three-dimensional vector in Figure 4.3. **F** has magnitude of 10 lb, and its line of action passes from the origin (0,0,0) to the point (2,6,4). **F** is written as the product of the magnitude $|F|$ and a unit vector $\mathbf{e_F}$ that points along its line of action:

$$\mathbf{F} = |F|\mathbf{e_F}$$
$$= 10 \text{ lb} \left(\frac{2\mathbf{i} + 6\mathbf{j} + 4\mathbf{k}}{\sqrt{2^2 + 6^2 + 4^2}} \right)$$
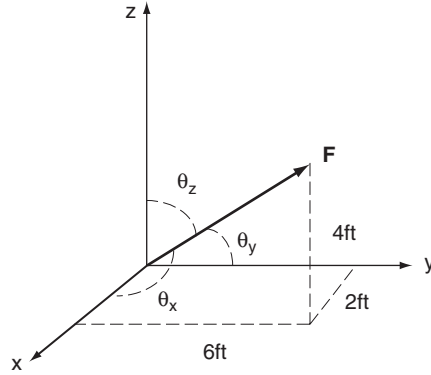$$\mathbf{F} = 2.67\mathbf{i} + 8.02\mathbf{j} + 5.34\mathbf{k} \text{ lb}$$

FIGURE 4.3 Three-dimensional vector defined by its magnitude and line of action.

The quantity in parentheses is the unit vector of **F**, or

$$\mathbf{e_F} = \left(\frac{2\mathbf{i} + 6\mathbf{j} + 4\mathbf{k}}{\sqrt{2^2 + 6^2 + 4^2}} \right) = 0.267\mathbf{i} + 0.802\mathbf{j} + 0.534\mathbf{k}$$

and the magnitude of **F** is

$$|F| = \sqrt{2.67^2 + 8.02^2 + 5.34^2}$$
$$= 10 \text{ lb}$$

The vector **F** in Figure 4.3 may also be defined in 3-D space in terms of the angles between its line of action and each coordinate axis. Consider the angles θ_x, θ_y, and θ_z that are measured from the positive x, y, and z axes, respectively, to **F**. Then

$$\cos \theta_x = \frac{F_x}{|F|} \tag{4.5}$$

$$\cos \theta_y = \frac{F_y}{|F|} \tag{4.6}$$

$$\cos \theta_z = \frac{F_z}{|F|} \tag{4.7}$$

These ratios are termed the *direction cosines* of **F**. The unit vector $\mathbf{e_F}$ is equivalent to

$$\mathbf{e_F} = \cos \theta_x \mathbf{i} + \cos \theta_y \mathbf{j} + \cos \theta_z \mathbf{k} \tag{4.8}$$

or, in general

$$\mathbf{e_F} = \left(\frac{F_x \mathbf{i} + F_y \mathbf{j} + F_z \mathbf{k}}{\sqrt{F_x^2 + F_y^2 + F_z^2}} \right) \tag{4.9}$$

The angles θ_x, θ_y, and θ_z for this example are consequently

$$\theta_x = \arccos\left(\frac{2.67}{10}\right) = 74.5°$$

$$\theta_y = \arccos\left(\frac{8.02}{10}\right) = 36.7°$$

$$\theta_z = \arccos\left(\frac{5.34}{10}\right) = 57.7°$$

Vectors are added by summing their components:

$$\mathbf{A} = A_x\mathbf{i} + A_y\mathbf{j} + A_z\mathbf{k}$$
$$\mathbf{B} = B_x\mathbf{i} + B_y\mathbf{j} + B_z\mathbf{k}$$
$$\mathbf{C} = \mathbf{A} + \mathbf{B} = (A_x + B_x)\mathbf{i} + (A_y + B_y)\mathbf{j} + (A_z + B_z)\mathbf{k}$$

In general, a set of forces may be combined into an equivalent force denoted the resultant **R**, where

$$\mathbf{R} = \sum F_x\mathbf{i} + \sum F_y\mathbf{j} + \sum F_z\mathbf{k} \tag{4.10}$$

as will be illustrated in subsequent sections. Vectors are subtracted similarly by subtracting vector components.

Vector multiplication consists of two distinct operations: the *dot* and *cross* products. The dot, or scalar, product of vectors **A** and **B** produces a scalar via

$$\mathbf{A} \cdot \mathbf{B} = AB\cos\theta \tag{4.11}$$

where θ is the angle between the vectors. For an orthogonal coordinate system, where all axes are 90° apart, all like terms alone remain, since

$$\mathbf{i} \cdot \mathbf{i} = \mathbf{j} \cdot \mathbf{j} = \mathbf{k} \cdot \mathbf{k} = 1$$
$$\mathbf{i} \cdot \mathbf{j} = \mathbf{j} \cdot \mathbf{k} = \mathbf{k} \cdot \mathbf{i} = \cdots = 0 \tag{4.12}$$

For example:

$$\mathbf{A} = 3\mathbf{i} + 2\mathbf{j} + \mathbf{k} \text{ ft}$$
$$\mathbf{B} = -2\mathbf{i} + 3\mathbf{j} + 10\mathbf{k} \text{ lb}$$
$$\mathbf{A} \cdot \mathbf{B} = 3(-2) + 2(3) + 1(10) = 10 \text{ ft lb}$$

Note that the dot product is commutative—that is, $\mathbf{A} \cdot \mathbf{B} \equiv \mathbf{B} \cdot \mathbf{A}$.

The physical interpretation of the dot product $\mathbf{A} \cdot \mathbf{B}$ is the projection of **A** onto **B**, or, equivalently, the projection of **B** onto **A**. For example, *work* is defined as the force that acts in the same direction as the motion of a body. Figure 4.4 (left) shows a force vector **F** dotted with a direction of motion vector **d**. The work W done by **F** is given by $\mathbf{F} \cdot \mathbf{d} \equiv Fd\cos\theta$. Dotting **F** with **d** yields the component of **F** acting in the same direction as **d**.
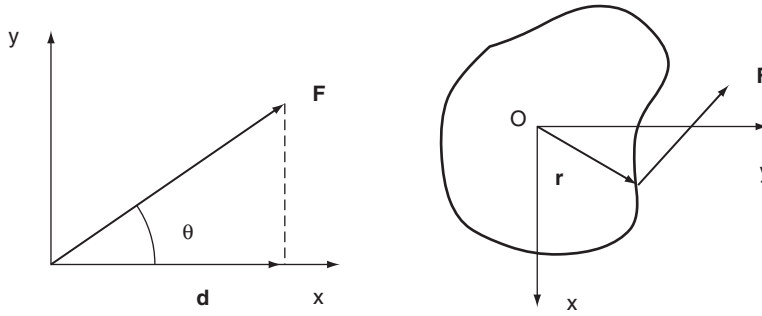
FIGURE 4.4 (Left) The dot, or scalar, product of vectors **F** and **d** is equivalent to the projection of **F** onto **d**. (Right) The cross, or vector, product of vectors **r** and **F** is a vector that points along the axis of rotation, the z-axis coming out of the page.

The *moment* of a force about a point or axis is a measure of its tendency to cause rotation. The cross, or vector, product of two vectors yields a new vector that points along the axis of rotation. For example, Figure 4.4 (right) shows a vector **F** acting in the x-y plane at a distance from the body's coordinate center O. The vector **r** points from O to the line of action of **F**. The cross product **r** × **F** is a vector that points in the z direction along the body's axis of rotation. If **F** and **r** are three-dimensional, thereby including **k** components, their cross product will have additional components of rotation about the x and y axes. The moment **M** resulting from crossing **r** into **F** is written

$$\mathbf{M} = M_x\mathbf{i} + M_y\mathbf{j} + M_z\mathbf{k} \tag{4.13}$$

where M_x, M_y, and M_z cause rotation of the body about the x, y, and z axes, respectively.

Cross products may be taken by crossing each vector component term by term—for example:

$$\begin{aligned}
\mathbf{A} \times \mathbf{B} = {} & 3(-2)\mathbf{i} \times \mathbf{i} + 3(3)\mathbf{i} \times \mathbf{j} + 3(10)\mathbf{i} \times \mathbf{k} \\
& + 2(-2)\mathbf{j} \times \mathbf{i} + 2(3)\mathbf{j} \times \mathbf{j} + 2(10)\mathbf{j} \times \mathbf{k} \\
& + 1(-2)\mathbf{k} \times \mathbf{i} + 1(3)\mathbf{k} \times \mathbf{j} + 1(10)\mathbf{k} \times \mathbf{k}
\end{aligned}$$

The magnitude $|\mathbf{A} \times \mathbf{B}| = AB \sin\theta$, where θ is the angle between **A** and **B**. Consequently, for an orthogonal coordinate system, the cross products of all like terms equal zero, and $\mathbf{i} \times \mathbf{j} = \mathbf{k}$, $\mathbf{j} \times \mathbf{k} = \mathbf{i}$, $\mathbf{k} \times \mathbf{i} = \mathbf{j}$, $\mathbf{i} \times \mathbf{k} = -\mathbf{j}$, and so on. The previous example yields

$$\begin{aligned}
\mathbf{A} \times \mathbf{B} &= 9\mathbf{k} - 30\mathbf{j} + 4\mathbf{k} + 20\mathbf{i} - 2\mathbf{j} - 3\mathbf{i} \\
&= 17\mathbf{i} - 32\mathbf{j} + 13\mathbf{k} \text{ lb ft}
\end{aligned}$$

Note that the cross product is *not* commutative—in other words, $\mathbf{A} \times \mathbf{B} \neq \mathbf{B} \times \mathbf{A}$.

Cross products of vectors are commonly computed using matrices. The previous example **A**×**B** is given by the matrix

$$\mathbf{A} \times \mathbf{B} = \begin{vmatrix} \mathbf{i} & \mathbf{j} & \mathbf{k} \\ A_x & A_y & A_z \\ B_x & B_y & B_z \end{vmatrix}$$

$$= \begin{vmatrix} \mathbf{i} & \mathbf{j} & \mathbf{k} \\ 3 & 2 & 1 \\ -2 & 3 & 10 \end{vmatrix} \tag{4.14}$$

$$= \mathbf{i}[(2)(10) - (1)(3)] - \mathbf{j}[(3)(10) - (1)(-2)] + \mathbf{k}[(3)(3) - (2)(-2)]$$

$$= \mathbf{i}(20 - 3) - \mathbf{j}(30 + 2) + \mathbf{k}(9 + 4)$$

$$= 17\mathbf{i} - 32\mathbf{j} + 13\mathbf{k} \text{ lb ft}$$

EXAMPLE PROBLEM 4.1

The vector **F** in Figure 4.5 has a magnitude of 10 kN and points along the dashed line as shown. (a) Write **F** as a vector. (b) What is the component of **F** in the *x-z* plane? (c) What moment does **F** generate about the origin (0,0,0)?
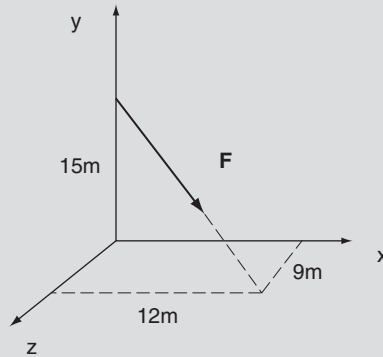

FIGURE 4.5   Force vector **F** has magnitude of 10 kN.

Solution

This example problem is solved using MATLAB. The $>>$ prompt denotes input, and the percent sign, %, precedes comments ignored by MATLAB. Lines that begin without the $>>$ prompt are MATLAB output. Some spaces in the following output were omitted to conserve space.

```
>> %(a) First write the direction vector d that points along F
>> % as a 1D array:
>> d = [12 -15 9]

d = 12 -15 9
>> % Now write the unit vector of F, giving its direction:
>> unit_vector = d/norm(d)
unit_vector = 0.5657 -0.7071 0.4243
```

```
>> % F consists of the magnitude 10 kN times this unit vector
>> F = 10*unit_vector

F = 5.6569  -7.0711  4.2426

>> % Or, more directly
>> F = 10*(d/norm(d))

F = 5.6569  -7.0711  4.2426

>> % (b) First write the vector r_xz that points from the origin
>> % to the intersection of F and the xz plane:
>> r_xz = [12 0 9]
r_xz = 12  0  9

>> % The dot product is given by the sum of all the term by term
>> % multiplications of elements of vectors F and r_xz
>> % F_dot_r_xz = sum(F.*r_xz)
>> % or simply, dot(F,r_xz)
>> F_dot_r_xz = dot(F,r_xz)

F_dot_r_xz = 106.0660

>> % (c) Cross F with a vector that points from the origin to
>> % any point along the line of action of vector F.
>> % The cross product is given by the cross function
>> r_xz_cross_F = cross(r_xz,F)

r_xz_cross_F = 63.6396  0  -84.8528

>> % Note that the cross product is not commutative
>> % resulting in different +- signs.
>> cross(F,r_xz)
ans = -63.6396  0  84.8528
```

EXAMPLE PROBLEM 4.2

Pointers are sometimes used in biomechanics labs to measure the location of a point in space. The pointer in Figure 4.6 consists of a rod equipped with two reflective markers, A and B. The locations of the two reflective markers are provided by a camera-based motion capture system. Given marker locations A = (629, −35, 190) mm and B = (669, 191, 120) mm, determine the location of the pointer tip, T, if marker B is a fixed distance, D, of 127 mm from the pointer tip.

Solution

Given marker locations

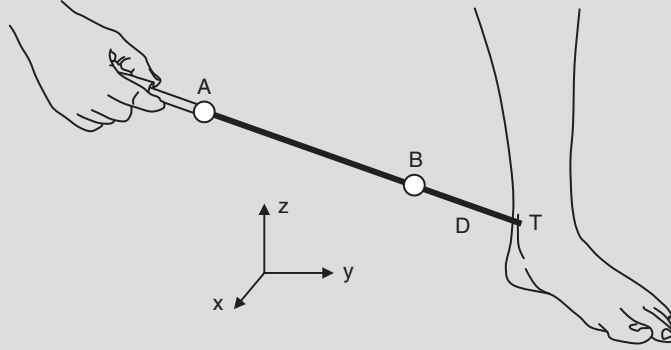A = (629, –35, 190) mm
B = (669, 191, 120) mm

Continued

FIGURE 4.6   Pointer with reflective markers A and B and with tip T located a fixed distance D = 127 mm from marker B.

then the vector from marker A to marker B is

$$\mathbf{r_{B/A}} = \mathbf{r_B} - \mathbf{r_A}$$
$$= (669\mathbf{i} + 191\mathbf{j} + 120\mathbf{k}) - (629\mathbf{i} - 35\mathbf{j} + 190\mathbf{k}) \text{ mm}$$
$$= 40\mathbf{i} + 226\mathbf{j} - 70\mathbf{k} \text{ mm}$$

with an associated unit vector,

$$\mathbf{e_{B/A}} = \frac{\mathbf{r_{B/A}}}{|\mathbf{r_{B/A}}|}$$
$$= \frac{40\mathbf{i} + 226\mathbf{j} - 70\mathbf{k}}{\sqrt{(40)^2 + (226)^2 + (-70)^2}}$$
$$= 0.167\mathbf{i} + 0.942\mathbf{j} - 0.292\mathbf{k}$$

Pointer tip T (Figure 4.7) is located by

$$\mathbf{r_T} = \mathbf{r_B} + \mathbf{r_{T/B}}$$
$$= \mathbf{r_B} + D\,\mathbf{e_{T/B}} \equiv \mathbf{r_B} + D\,\mathbf{e_{B/A}}$$
$$= (669\mathbf{i} + 191\mathbf{j} + 120\mathbf{k}) + 127(0.167\mathbf{i} + 0.942\mathbf{j} - 0.292\mathbf{k}) \text{ mm}$$
$$= 690\mathbf{i} + 311\mathbf{j} + 83\mathbf{k} \text{ mm}$$

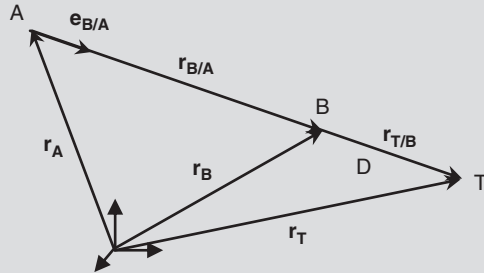FIGURE 4.7   Pointer tip T can be located using vector r_B, the unit vector $\mathbf{e_{B/A}}$ and the distance D from B to T.

4.2.2 Coordinate Transformations

3-D Direction Cosines

When studying the kinematics of human motion, it is often necessary to transform body or body segment coordinates from one coordinate system to another. For example, coordinates corresponding to a coordinate system determined by markers on the body, a moving coordinate system, must be translated to coordinates with respect to the fixed laboratory, an inertial coordinate system. These three-dimensional transformations use direction cosines that are computed as follows.

Consider the vector $\mathbf{A}$ measured in terms of the uppercase coordinate system XYZ, shown in Figure 4.8 in terms of the unit vectors $\mathbf{I}$, $\mathbf{J}$, $\mathbf{K}$:

$$\mathbf{A} = A_x\mathbf{I} + A_y\mathbf{J} + A_z\mathbf{K} \tag{4.15}$$

The unit vectors $\mathbf{I}$, $\mathbf{J}$, $\mathbf{K}$ can be written in terms of $\mathbf{i}$, $\mathbf{j}$, $\mathbf{k}$ in the xyz system

$$\mathbf{I} = \cos\theta_{xX}\mathbf{i} + \cos\theta_{yX}\mathbf{j} + \cos\theta_{zX}\mathbf{k} \tag{4.16}$$

$$\mathbf{J} = \cos\theta_{xY}\mathbf{i} + \cos\theta_{yY}\mathbf{j} + \cos\theta_{zY}\mathbf{k} \tag{4.17}$$

$$\mathbf{K} = \cos\theta_{xZ}\mathbf{i} + \cos\theta_{yZ}\mathbf{j} + \cos\theta_{zZ}\mathbf{k} \tag{4.18}$$

where θ_{xX} is the angle between $\mathbf{i}$ and $\mathbf{I}$, and similarly for the other angles.

Substituting Eqs. (4.16)–(4.18) into Eq. (4.15) gives

$$\begin{aligned}
\mathbf{A} = A_x\big[&\cos\theta_{xX}\mathbf{i} + \cos\theta_{yX}\mathbf{j} + \cos\theta_{zX}\mathbf{k}\big] \\
+ A_y\big[&\cos\theta_{xY}\mathbf{i} + \cos\theta_{yY}\mathbf{j} + \cos\theta_{zY}\mathbf{k}\big] \\
+ A_z\big[&\cos\theta_{xZ}\mathbf{i} + \cos\theta_{yZ}\mathbf{j} + \cos\theta_{zZ}\mathbf{k}\big]
\end{aligned} \tag{4.19}$$

or

$$\begin{aligned}
\mathbf{A} = \big(&A_x\cos\theta_{xX} + A_y\cos\theta_{xY} + A_z\cos\theta_{xZ}\big)\mathbf{i} \\
+ \big(&A_x\cos\theta_{yX} + A_y\cos\theta_{yY} + A_z\cos\theta_{yZ}\big)\mathbf{j} \\
+ \big(&A_x\cos\theta_{zX} + A_y\cos\theta_{zY} + A_z\cos\theta_{zZ}\big)\mathbf{k}
\end{aligned} \tag{4.20}$$

Consequently, $\mathbf{A}$ may be represented in terms of $\mathbf{I}$, $\mathbf{J}$, $\mathbf{K}$ or $\mathbf{i}$, $\mathbf{j}$, $\mathbf{k}$.
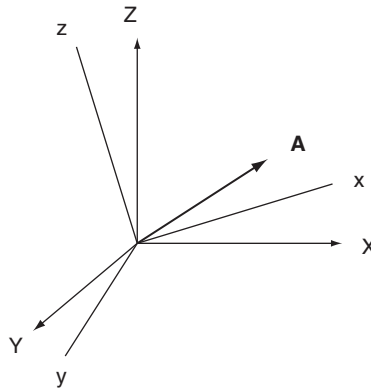

FIGURE 4.8   Vector $\mathbf{A}$, measured with respect to coordinate system XYZ is related to coordinate system xyz via the nine direction cosines of Eq. (4.20).

Euler Angles

The coordinates of a body in one orthogonal coordinate system may be related to another orthogonal coordinate system via Euler angle transformation matrices. For example, one coordinate system might correspond to markers placed on the patient's pelvis, and the other coordinate system might correspond to the patient's thigh. The two coordinate systems are related by a series of rotations about each original axis in turn. Figure 4.9 shows
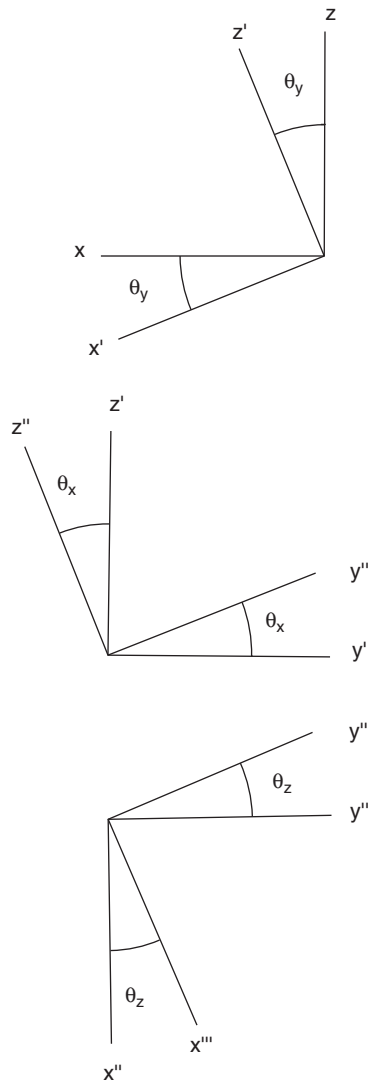

FIGURE 4.9 The unprimed coordinate system xyz undergoes three rotations: about the y-axis (top), about the x-axis (middle), and about the z-axis (bottom), yielding the new triple-primed coordinate system $x''' \, y''' \, z'''$ for a y-x-z rotation sequence.

the *xyz* coordinate axes with a *y-x-z* rotation sequence. First, *xyz* is rotated about the *y*-axis (top), transforming the **ijk** unit vectors into the **i′j′k′** unit vectors, via the equations

$$\mathbf{i}' = \cos\theta_y \mathbf{i} - \sin\theta_y \mathbf{k} \tag{4.21}$$

$$\mathbf{j}' = \mathbf{j} \tag{4.22}$$

$$\mathbf{k}' = \sin\theta_y \mathbf{i} + \cos\theta_y \mathbf{k} \tag{4.23}$$

This new primed coordinate system is then rotated about the *x*-axis (Figure 4.9, middle), giving the double-primed system

$$\mathbf{i}'' = \mathbf{i}' \tag{4.24}$$

$$\mathbf{j}'' = \cos\theta_x \mathbf{j}' + \sin\theta_x \mathbf{k}' \tag{4.25}$$

$$\mathbf{k}'' = -\sin\theta_x \mathbf{j}' + \cos\theta_x \mathbf{k}' \tag{4.26}$$

Finally, the double-primed system is rotated about the *z*-axis, giving the triple-primed system

$$\mathbf{i}''' = \cos\theta_z \mathbf{i}'' + \sin\theta_z \mathbf{j}'' \tag{4.27}$$

$$\mathbf{j}''' = -\sin\theta_z \mathbf{i}'' + \cos\theta_z \mathbf{j}'' \tag{4.28}$$

$$\mathbf{k}''' = \mathbf{k}'' \tag{4.29}$$

The three rotations may be written in matrix form to directly translate **ijk** into **i′′′j′′′k′′′**:

$$\begin{bmatrix} \mathbf{i}''' \\ \mathbf{j}''' \\ \mathbf{k}''' \end{bmatrix} = \begin{bmatrix} \cos\theta_z & \sin\theta_z & 0 \\ -\sin\theta_z & \cos\theta_z & 0 \\ 0 & 0 & 1 \end{bmatrix} \begin{bmatrix} 1 & 0 & 0 \\ 0 & \cos\theta_x & \sin\theta_x \\ 0 & -\sin\theta_x & \cos\theta_x \end{bmatrix} \begin{bmatrix} \cos\theta_y & 0 & -\sin\theta_y \\ 0 & 1 & 0 \\ \sin\theta_y & 0 & \cos\theta_y \end{bmatrix} \begin{bmatrix} \mathbf{i} \\ \mathbf{j} \\ \mathbf{k} \end{bmatrix} \tag{4.30}$$

$$= \begin{bmatrix} \cos\theta_z & \sin\theta_z\cos\theta_x & \sin\theta_z\sin\theta_x \\ -\sin\theta_z & \cos\theta_z\cos\theta_x & \cos\theta_z\sin\theta_x \\ 0 & -\sin\theta_x & \cos\theta_x \end{bmatrix} \begin{bmatrix} \cos\theta_y & 0 & -\sin\theta_y \\ 0 & 1 & 0 \\ \sin\theta_y & 0 & \cos\theta_y \end{bmatrix} \begin{bmatrix} \mathbf{i} \\ \mathbf{j} \\ \mathbf{k} \end{bmatrix}$$

$$\begin{bmatrix} \mathbf{i}''' \\ \mathbf{j}''' \\ \mathbf{k}''' \end{bmatrix} = \begin{bmatrix} \cos\theta_z\cos\theta_y + \sin\theta_z\sin\theta_x\sin\theta_y & \sin\theta_z\cos\theta_x & -\cos\theta_z\sin\theta_y + \sin\theta_z\sin\theta_x\cos\theta_y \\ -\sin\theta_z\cos\theta_y + \cos\theta_z\sin\theta_x\sin\theta_y & \cos\theta_z\cos\theta_x & \sin\theta_z\sin\theta_y + \cos\theta_z\sin\theta_x\cos\theta_y \\ \cos\theta_x\sin\theta_y & -\sin\theta_x & \cos\theta_x\cos\theta_y \end{bmatrix} \begin{bmatrix} \mathbf{i} \\ \mathbf{j} \\ \mathbf{k} \end{bmatrix} \tag{4.31}$$

If the angles of coordinate system rotation ($\theta_x, \theta_y, \theta_z$) are known, coordinates in the *xyz* system can be transformed into the *x′′′y′′′z′′′* system. Alternatively, if both the unprimed and triple-primed coordinates are known, the angles may be computed as follows:

$$\mathbf{k}''' \cdot \mathbf{j} = -\sin\theta_x$$

$$\theta_x = -\arcsin(\mathbf{k}''' \cdot \mathbf{j}) \tag{4.32}$$

$$\mathbf{k}''' \cdot \mathbf{i} = \cos\theta_x \sin\theta_y$$

$$\theta_y = \arcsin\left[\frac{\mathbf{k}''' \cdot \mathbf{i}}{\cos\theta_x}\right] \tag{4.33}$$

$$\mathbf{i}''' \cdot \mathbf{j} = \sin\theta_z \cos\theta_x$$

$$\theta_z = \arcsin\left[\frac{\mathbf{i}''' \cdot \mathbf{j}}{\cos\theta_x}\right] \tag{4.34}$$

Walking produces tri-planar hip, knee, and ankle motion: flexion/extension (FE), abduction/adduction (AA), and internal/external transverse rotation (TR). Euler angles offer an opportunity to quantify these coordinated motions. The order of the Euler angle rotation sequence FE-AA-TR, corresponding to a *y-x-z* axis rotation sequence, or tilt-obliquity-rotation, was chosen to correlate to the largest to smallest joint excursions during walking [6]. More recently, research suggests that for pelvic motion, an Euler angle *z-x-y* rotation sequence corresponding to rotation-obliquity-tilt is more consistent with clinical observations [1].

EXAMPLE PROBLEM 4.3

Write the Euler angle transformation matrices for the *y-x-z* rotation sequence using the MATLAB symbolic math toolbox.

Solution

The following MATLAB script, or m-file, is a collection of MATLAB commands that can be run by invoking the m-file name "eulerangles" in the command line.

```
% eulerangles.m
%
% Euler angles for y-x-z rotation sequence
% using MATLAB symbolic math toolbox
%
% x, y and z are thetax, thetay and thetaz, respectively
% First define them as symbolic variables

syms x y z

% Writing equations 4.21-23 as a matrix A

A = [ cos(y), 0, -sin(y);
      0,      1,       0;
      sin(y), 0,   cos(y)]

% equations 4.24-26 as matrix B

B = [ 1      0,        0;
      0, cos(x), sin(x);
      0, -sin(x), cos(x)]
```

```
% and equations 4.27-29 as matrix C
C = [ cos(z), sin(z), 0;
     -sin(z), cos(z), 0;
        0,       0,    1]
```

```
% The matrix equation 4.30 is created by multiplying matrices C, B
% and A
```

```
D=C*B*A
```

The resulting transformation matrix from the preceding m-file is

```
D =
[cos(z)*cos(y)+sin(z)*sin(x)*sin(y), sin(z)*cos(x), -cos(z)
*sin(y)+sin(z)*sin(x)*cos(y)]
[-sin(z)*cos(y)+cos(z)*sin(x)*sin(y), cos(z)*cos(x), sin(z)
*sin(y)+cos(z)*sin(x)*cos(y)]
[cos(x)*sin(y),    -sin(x),    cos(x)*cos(y)]
```

which is the same as Eq. (4.31).

The Euler transformation matrices are used differently depending on the available data. For example, if the body coordinates in both the fixed (unprimed) and body (triple primed) systems are known, the body angles θ_x, θ_y, and θ_z can be computed, for example, using Eqs. (4.32)–(4.34) for a y-x-z rotation sequence. Alternatively, the body's initial position and the angles θ_x, θ_y, and θ_z may be used to compute the body's final position.

EXAMPLE PROBLEM 4.4

An aircraft undergoes 30 degrees of pitch (θ_x), then 20 degrees of roll (θ_y), and finally 10 degrees of yaw (θ_z). Write a MATLAB function that computes the Euler angle transformation matrix for this series of angular rotations.

Solution

Since computers use radians for trigonometric calculations, first write two simple functions to compute cosines and sines in degrees:

```
function y = cosd(x)
%COSD(X) cosines of the elements of X measured in degrees.
y = cos(pi*x/180);
```

```
function y = sind(x)
%SIND(X) sines of the elements of X measured in degrees.
y = sin(pi*x/180);
```

Next write the x-y-z rotation sequence transformation matrix:

```
function D = eulangle(thetax, thetay, thetaz)
%EULANGLE matrix of rotations by Euler's angles.
% EULANGLE(thetax, thetay, thetaz) yields the matrix of
```

Continued

```
% rotation of a system of coordinates by Euler's
% angles thetax, thetay and thetaz, measured in degrees.

% Now the first rotation is about the x-axis, so we use eqs. 4.24-26

A = [ 1    0                 0
      0    cosd(thetax)    sind(thetax)
      0   -sind(thetax)   cosd(thetax) ];

% Next is the y-axis rotation (eqs. 4.21-23)

B = [ cosd(thetay)    0    -sind(thetay)
      0               1    0
      sind(thetay)    0    cosd(thetay) ];

% Finally, the z-axis rotation (eqs. 4.27-29)

C = [ cosd(thetaz)     sind(thetaz)    0
     -sind(thetaz)     cosd(thetaz)    0
      0                0               1 ];
% Multiplying rotation matrices C, B and A as in Eq. 4.30 gives the
solution:

D=C*B*A;
```

Now use this function to compute the numerical transformation matrix:

```
>> eulangle(30,20,10)
ans =
   0.9254     0.3188    -0.2049
  -0.1632     0.8232     0.5438
   0.3420    -0.4698     0.8138
```

This matrix can be used to convert any point in the initial coordinate system (premaneuver) to its position after the roll, pitch, and yaw maneuvers have been executed.

4.2.3 Static Equilibrium

Newton's equations of motion applied to a structure in static equilibrium reduce to the following vector equations:

$$\sum \mathbf{F} = 0 \tag{4.35}$$

$$\sum \mathbf{M} = 0 \tag{4.36}$$

These equations are applied to biological systems in the same manner as standard mechanical structures. Analysis begins with a drawing of the free-body diagram of the body segments of interest with all externally applied loads and reaction forces at the supports. Orthopedic joints can be modeled with appropriate ideal joints, such as hinge, ball-and-socket, and so forth, as discussed in Chapter 3 (see Figure 3.33).

EXAMPLE PROBLEM 4.5

Figure 4.10 (top) shows a Russell's traction rig used to apply an axial tensile force to a fractured femur for immobilization. (a) What magnitude weight w must be suspended from the free end of the cable to maintain the leg in static equilibrium? (b) Compute the average tensile force applied to the thigh under these conditions.

Solution

The free-body diagram for this system is shown in the lower panel of Figure 4.10. If the pulleys are assumed frictionless and of small radius, the cable tension T is constant throughout. Using Eq. (4.35),

$$\mathbf{F}_1 + \mathbf{F}_2 + \mathbf{F}_3 + \mathbf{F}_{\text{femur}} - mg\mathbf{j} = 0$$

Writing each force in vector form,

$$\mathbf{F}_1 = -F_1\mathbf{i} = -T\mathbf{i}$$
$$\begin{aligned}\mathbf{F}_2 &= (-F_2\cos 30°)\mathbf{i} + (F_2\sin 30°)\mathbf{j} \\ &= (-T\cos 30°)\mathbf{i} + (T\sin 30°)\mathbf{j}\end{aligned}$$
$$\begin{aligned}\mathbf{F}_3 &= (F_3\cos 40°)\mathbf{i} + (F_3\sin 40°)\mathbf{j} \\ &= (T\cos 40°)\mathbf{i} + (T\sin 40°)\mathbf{j}\end{aligned}$$
$$\mathbf{F}_{\text{femur}} = (F_{\text{femur}}\cos 20°)\mathbf{i} = (F_{\text{femur}}\sin 20°)\mathbf{j}$$
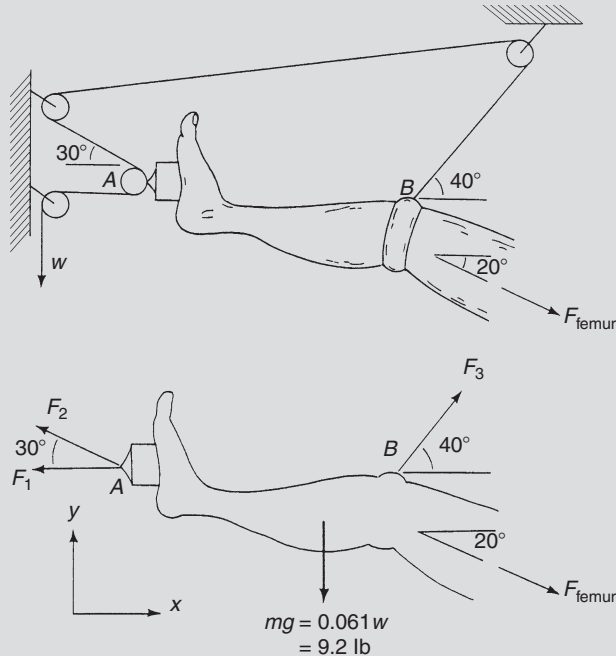

FIGURE 4.10 (Top) Russell's traction mechanism for clinically loading lower-extremity limbs. (Bottom) Free-body diagram of the leg in traction. *Adapted from [5].*

Continued

Using Table 4.1, and neglecting the weight of the thigh, the weight of the foot and leg is 0.061 multiplied by total body weight, yielding

$$m g \mathbf{j} = (0.061)(150\mathbf{j} \text{ lb}) = 9.2\mathbf{j} \text{ lb}$$

Summing the x components gives

$$-T - T \cos 30° + T \cos 40° + F_{\text{femur}} \cos 20° = 0$$

Summing the y components gives

$$T \sin 30° + T \sin 40° - F_{\text{femur}} \sin 20° - mg = 0$$

The last two expressions may be solved simultaneously, giving both T, which is equal to the required externally applied weight, and the axial tensile force, F_{femur}

$$T = 12.4 \text{ lb}$$
$$F_{\text{femur}} = 14.5 \text{ lb}$$

EXAMPLE PROBLEM 4.6

The force plate depicted in Figure 4.11 has four sensors, one at each corner, that read the vertical forces F_1, F_2, F_3, and F_4. If the plate is square with side of length ℓ and forces $F_1 - F_4$ are known, write two expressions that will give the x and y locations of the resultant force R.

Solution

The resultant magnitude R can be computed from the sum of forces in the z-direction:

$$\sum F_z = 0$$
$$F_1 + F_2 + F_3 + F_4 - R = 0$$
$$R = F_1 + F_2 + F_3 + F_4$$
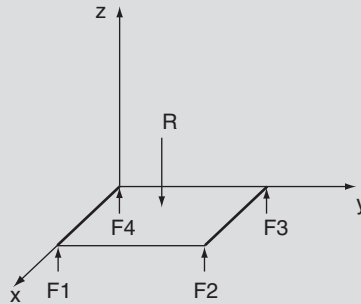

FIGURE 4.11 A square force plate with sides of length ℓ is loaded with resultant force R and detects the vertical forces at each corner, $F_1 - F_4$.

The force plate remains horizontal, so the sum of the moments about the x and y axes must each be zero. Taking moments about the x-axis,

$$\sum M_x = 0$$
$$F_2\ell + F_3\ell - Ry = 0$$
$$y = \frac{(F_2 + F_3)\ell}{R}$$

Similarly, summing moments about the y-axis,

$$\sum M_y = 0$$

$$F_1 \ell + F_2 \ell - Rx = 0$$

$$x = \frac{(F_1 + F_2)\ell}{R}$$

The coordinates x and y locate the resultant R.

4.2.4 Anthropomorphic Mass Moments of Inertia

A body's mass resists linear motion; its mass moment of inertia resists rotation. The resistance of a body, or a body segment such as a thigh in gait analysis, to rotation is quantified by the body or body segment's moment of inertia I:

$$I = \int_m r^2 dm \tag{4.37}$$

where m is the body mass and r is the moment arm to the axis of rotation. The elemental mass dm can be written ρdV. For a body with constant density ρ, the moment of inertia can be found by integrating over the body's volume V:

$$I = \rho \int_V r^2 dV \tag{4.38}$$

This general expression can be written in terms of rotation about the x, y, and z axes:

$$\begin{aligned} I_{xx} &= \int_V (y^2 + z^2)\rho dV \\ I_{yy} &= \int_V (x^2 + z^2)\rho dV \\ I_{zz} &= \int_V (x^2 + y^2)\rho dV \end{aligned} \tag{4.39}$$

The *radius of gyration* k is the moment arm between the axis of rotation and a single point where all of the body's mass is concentrated. Consequently, a body segment may be treated as a point mass with moment of inertia

$$I = mk^2 \tag{4.40}$$

where m is the body segment mass. The moment of inertia with respect to a parallel axis I is related to the moment of inertia with respect to the body's center of mass I_{cm} via the *parallel axis theorem*:

$$I = I_{cm} + md^2 \tag{4.41}$$

where d is the perpendicular distance between the two parallel axes. Anthropomorphic data for various body segments are listed in Table 4.1.

TABLE 4.1   Anthropomorphic Data

Segment	Definition	Segment Weight/ Body Weight	Center Mass/ Segment Length		Radius Gyration/ Segment Length	
			Proximal	Distal	Proximal	Distal
Hand	Wrist axis/knuckle II middle finger	0.006	0.506	0.494	0.587	0.577
Forearm	Elbow axis/ulnar styloid	0.016	0.430	0.570	0.526	0.647
Upper arm	Glenohumeral axis/elbow axis	0.028	0.436	0.564	0.542	0.645
Forearm and hand	Elbow axis/ulnar styloid	0.022	0.682	0.318	0.827	0.565
Total arm	Glenohumeral joint/ulnar styloid	0.050	0.530	0.470	0.645	0.596
Foot	Lateral malleolus/head metatarsal II	0.0145	0.50	0.50	0.690	0.690
Leg	Femoral condyles/medial malleolus	0.0465	0.433	0.567	0.528	0.643
Thigh	Greater trochanter/femoral condyles	0.100	0.433	0.567	0.540	0.653
Foot and leg	Femoral condyles/medial malleolus	0.061	0.606	0.394	0.735	0.572
Total leg	Greater trochanter/medial malleolus	0.161	0.447	0.553	0.560	0.650
Head and neck	C7-T1 and 1st rib/ear canal	0.081	1.000		1.116	
Shoulder mass	Sternoclavicular joint/ glenohumeral axis		0.712	0.288		
Thorax	C7-T1/T12-L1 and diaphragm	0.216	0.82	0.18		
Abdomen	T12-L1/L4-L5	0.139	0.44	0.56		
Pelvis	L4-L5/greater trochanter	0.142	0.105	0.895		
Thorax and abdomen	C7-T1/L4-L5	0.355	0.63	0.37		
Abdomen and pelvis	T12-L1/greater trochanter	0.281	0.27	0.73		
Trunk	Greater trochanter/glenohumeral joint	0.497	0.50	0.50		
Trunk, head, neck	Greater trochanter/glenohumeral joint	0.578	0.66	0.34	0.830	0.607
Head, arm, trunk	Greater trochanter/glenohumeral joint	0.678	0.626	0.374	0.798	0.621

Adapted from Winter, 2009.

EXAMPLE PROBLEM 4.7

A person weighing 150 pounds has a thigh length of 17 inches. Find the moment of inertia of this body segment with respect to its center of mass in SI units.

Solution

Thigh length in SI units is

$$\ell_{\text{thigh}} = 17 \text{ in} = 0.432 \text{ m}$$

Table 4.1 lists ratios of segment weight to body weight for different body segments. Starting with body mass,

$$m_{\text{body}} = (150 \text{ lb})(0.454 \text{ kg/lb}) = 68.1 \text{ kg}$$

the thigh segment mass is

$$m_{\text{thigh}} = (0.100)(68.1 \text{ kg}) = 6.81 \text{ kg}$$

Table 4.1 also lists body segment center of mass and radius of gyration as ratios with respect to segment length for each body segment. Table 4.1 gives both proximal and distal segment length ratios. Note that "proximal" for the thigh refers toward the hip and "distal" refers toward the knee. Consequently, the proximal thigh segment length is the distance between the thigh center of mass and the hip, and the distal thigh segment length is the distance between the thigh center of mass and the knee. The moment of inertia of the thigh with respect to the hip is therefore

$$I_{\text{thigh/hip}} = mk^2 = (6.81 \text{ kg})[(0.540)(0.432 \text{ m})]^2 = 0.371 \text{ kg m}^2$$

The thigh's moment of inertia with respect to the hip is related to the thigh's moment of inertia with respect to its center of mass via the parallel axis theorem (Eq. (4.41)). Consequently, Table 4.1 data can be used to compute segment moments of inertia with respect to their centers of mass:

$$I_{\text{thigh/hip}} = I_{\text{thigh/cm}} + md^2$$

so

$$I_{\text{thigh/cm}} = I_{\text{thigh/hip}} - md^2$$

In this case, distance d is given by the proximal segment length data:

$$d = (0.432 \text{ m})(0.433) = 0.187 \text{ m}$$

and the final result is

$$I_{\text{thigh/cm}} = 0.371 \text{ kg m}^2 - (6.81 \text{ kg})(0.187 \text{ m})^2 = 0.133 \text{ kg m}^2$$

EXAMPLE PROBLEM 4.8

A person weighing 160 pounds is holding a 10-lb weight in his palm, with the elbow fixed at 90° flexion (Figure 4.12 (top)). (a) What force must the biceps generate to hold the forearm in static equilibrium? (b) What force(s) does the forearm exert on the humerus?
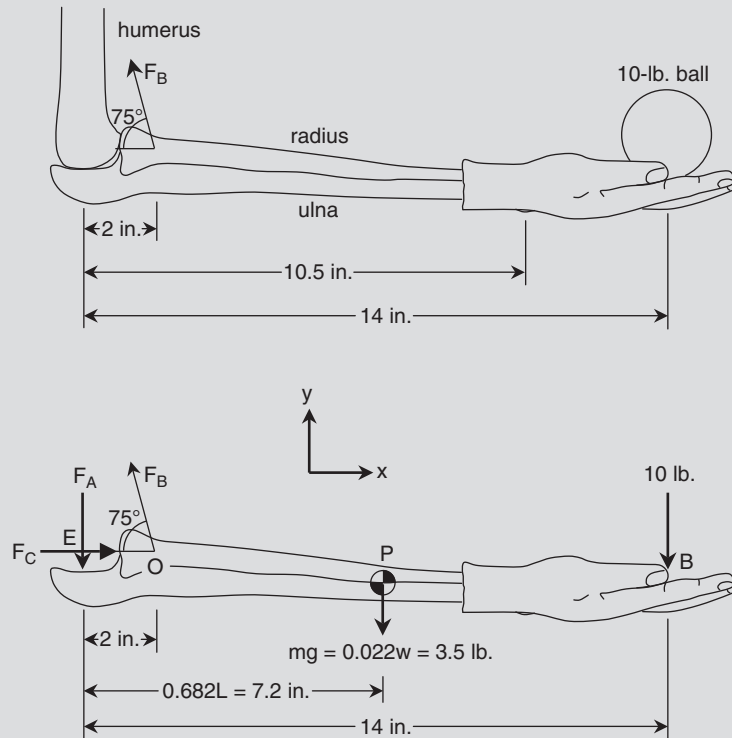
Continued

FIGURE 4.12 (Top) The forearm held statically fixed in 90° flexion while holding a 10 lb weight at the hand. (Bottom) Free-body diagram of the forearm system. *Adapted from [5].*

Solution

Figure 4.12 (bottom) shows the free-body diagram of this system. Due to the increased number of unknowns compared to the previous example, both Eqs. (4.35) and (4.36) will be used. From the anthropometric relationships in Table 4.1, the segment weight (forearm and hand) is approximated as 2.2 percent of total body weight, with the segment mass located 68.2 percent of the segment length away from the elbow axis. Note that the segment length for the "forearm and hand" segment in Table 4.1 is defined as the distance between the elbow axis and the ulnar styloid.

Summing moments about the elbow at point O, the equilibrium equation $\sum \mathbf{M} = 0$ can be written as

$$\mathbf{r}_{OE} \times \mathbf{F}_A + \mathbf{r}_{OB} \times (-10 \text{ lb})\mathbf{j} + \mathbf{r}_{OP} \times (-3.5 \text{ lb})\mathbf{j} = 0$$
$$(-2 \text{ in})\mathbf{i} \times (-F_A)\mathbf{j} + (12 \text{ in})\mathbf{i} \times (-10 \text{ lb})\mathbf{j} + (5.2 \text{ in})\mathbf{i} \times (-3.5 \text{ lb})\mathbf{j} = 0$$
$$(2 \text{ in})F_A\mathbf{k} - (120 \text{ lb in})\mathbf{k} - (18.2 \text{ lb in})\mathbf{k} = 0$$

Solving this last expression for the one unknown, F_A, the vertical force at the elbow:

$$F_A = 69.1 \text{ lb}$$

To find the unknown horizontal force at the elbow, F_C, and the unknown force the biceps must generate, F_B, the other equation of equilibrium $\sum \mathbf{F} = 0$ is used:

$$F_C \mathbf{i} - F_A \mathbf{j} + (-F_B \cos 75°\mathbf{i} + F_B \sin 75°\mathbf{j}) - 10 \text{ lb}\mathbf{j} - 3.5 \text{ lb}\mathbf{j} = 0$$

Summing the x and y components gives

$$F_C - F_B \cos(75°) = 0$$
$$-F_A + F_B \sin(75°) - 10 \text{ lb} - 3.5 \text{ lb} = 0$$

Solving these last two equations simultaneously and using $F_A = 69.1$ lb gives the force of the biceps muscle, F_B, and the horizontal elbow force, F_C:

$$F_B = 85.5 \text{ lb}$$
$$F_C = 22.1 \text{ lb}$$

4.2.5 Equations of Motion

Vector equations of motion are used to describe the translational and rotational kinetics of bodies.

Newton's Equations of Motion

Newton's second law relates the net force **F** and the resulting translational motion as

$$\mathbf{F} = m\mathbf{a} \tag{4.42}$$

where **a** is the linear acceleration of the body's center of mass for translation. For rotation

$$\mathbf{M} = \mathbf{I}\boldsymbol{\alpha} \tag{4.43}$$

where $\mathbf{I}\boldsymbol{\alpha}$ is the body's angular momentum. Hence, the rate of change of a body's angular momentum is equal to the net moment **M** acting on the body. These two vector equations of motion are typically written as a set of six x, y, and z component equations.

Euler's Equations of Motion

Newton's equations of motion describe the motion of the center of mass of a body. More generally, Euler's equations of motion describe the motion of a rigid body with respect to its center of mass. For the special case where the xyz coordinate axes are chosen to coincide with the body's principal axes, that is, a cartesian coordinate system whose origin is located at the body's center of mass, Euler's equations are

$$\sum M_x = I_{xx}\alpha_x + (I_{zz} - I_{yy})\omega_y\omega_z \tag{4.44}$$

$$\sum M_y = I_{yy}\alpha_y + (I_{xx} - I_{zz})\omega_z\omega_x \tag{4.45}$$

$$\sum M_z = I_{zz}\alpha_z + (I_{yy} - I_{xx})\omega_x\omega_y \tag{4.46}$$

M_i is the net moment, I_{ii} is the body's moment of inertia with respect to the principal axes, and α_i and ω_i are the body's angular acceleration and angular velocity, respectively. Euler's equations require angular measurements in radians. Their derivation is outside the scope of this chapter but may be found in an intermediate dynamics book—for example, [12]. Equations (4.44)–(4.46) will be used in Section 4.6 to compute intersegmental or joint moments.

4.3 MECHANICS OF MATERIALS

Just as kinematic and kinetic relations may be applied to biological bodies to describe their motion and its associated forces, concepts from mechanics of materials may be used to quantify tissue deformation, to study distributed orthopedic forces, and to predict the performance of orthopedic implants and prostheses and of surgical corrections. Since this topic is very broad, some representative concepts will be illustrated with the following examples.

An orthopedic bone plate is a flat segment of stainless steel used to screw two failed sections of bone together. The bone plate in Figure 4.13 has a rectangular cross section, A, measuring 4.17 mm by 12 mm and made of 316L stainless steel. An applied axial load, F, of 500 N produces axial *stress*, σ, (force/area):

$$
\begin{aligned}
\sigma &= \frac{F}{A} \\
&= \frac{500 \text{ N}}{(4.17 \times 10^{-3} \text{ m})(12 \times 10^{-3} \text{ m})} = 10 \text{ MPa}
\end{aligned} \tag{4.47}
$$

The maximum shear stress, $\tau_{\max}$, occurs at a 45° angle to the applied load

$$
\begin{aligned}
\tau\max &= \frac{F_{45°}}{A_{45°}} \\
&= \frac{(500 \text{ N})\cos 45°}{\left[\dfrac{(0.00417 \text{ m})(0.012 \text{ m})}{\cos 45°}\right]} = 5 \text{ MPa}
\end{aligned} \tag{4.48}
$$

which is 0.5σ, as expected from mechanics of materials principles. Prior to loading, two points were punched 15 mm apart on the long axis of the plate, as shown. After the 500 N load is applied, those marks are an additional 0.00075 mm apart. The plate's *strain*, ε, relates the change in length, $\Delta\ell$ to the original length, ℓ:
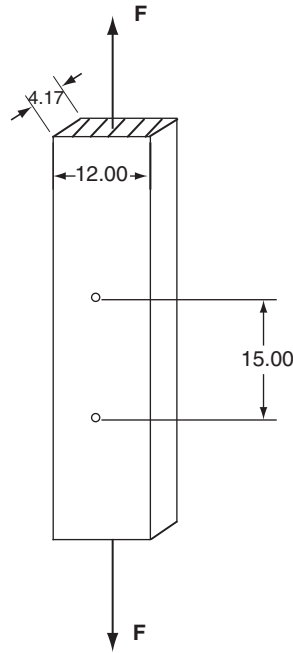
FIGURE 4.13 Bone plate used to fix bone fractures, with applied axial load. Dimensions are in mm. *Adapted from [2].*

$$\varepsilon = \frac{\Delta \ell}{\ell}$$
$$= \frac{0.00075 \text{ mm}}{15 \text{ mm}} = 50 \times 10^{-6} \tag{4.49}$$

often reported as 50 μ, where μ denotes microstrain (10^{-6}).

The *elastic modulus*, E, relates stress and strain and is a measure of a material's resistance to distortion by a tensile or compressive load. For linearly elastic (Hookean) materials, E is a constant, and a plot of σ as a function of ε is a straight line with slope E:

$$E = \frac{\sigma}{\varepsilon} \tag{4.50}$$

For the bone plate,

$$E = \frac{10 \times 10^6 \text{ Pa}}{50 \times 10^{-6}} = 200 \text{ GPa}$$

Materials such as metals and plastics display linearly elastic properties only in limited ranges of applied loads. Biomaterials have even more complex elastic properties. Figure 4.14 shows tensile stress-strain curves measured from longitudinal and transverse sections of
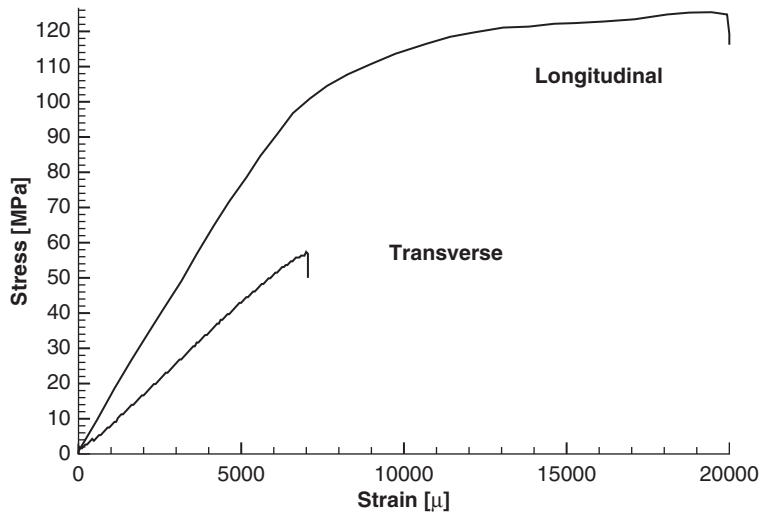
FIGURE 4.14   Tensile stress-strain curves for longitudinal and transverse sections of bone. *Adapted from [2].*

TABLE 4.2   Tensile Yield and Ultimate Stresses, and Elastic Moduli *E* for Some Common Orthopedic Materials

Material	σ_{yield} [MPa]	σ_{ultimate} [MPa]	E [GPa]
Stainless steel	700	850	180
Cobalt alloy	490	700	200
Titanium alloy	1,100	1,250	110
Bone	85	120	18
PMMA (fixative)		35	5
UHMWPE (bearing)	14	27	1
Patellar ligament		58	

Data from [2].

bone. Taking the longitudinal curve first, from 0 to 7,000μ, bone behaves as a purely elastic solid, with E $\approx$ 12 GPa. At a tensile stress of approximately 90 MPa, the stress-strain curve becomes nonlinear, yielding into the plastic region of deformation. This sample ultimately fails around 120 MPa. Table 4.2 shows elastic moduli, yield stresses, and ultimate stresses for some common orthopedic materials, both natural and implant.

Figure 4.14 also shows that the elastic properties of bone differ depending on whether the sample is cut in the longitudinal or transverse direction—that is, bone is anisotropic. Bone is much weaker and less stiff in the transverse compared to the longitudinal direction, as is illustrated by the large differences in the yield and ultimate stresses and the slopes of the stress-strain curves for the two samples.
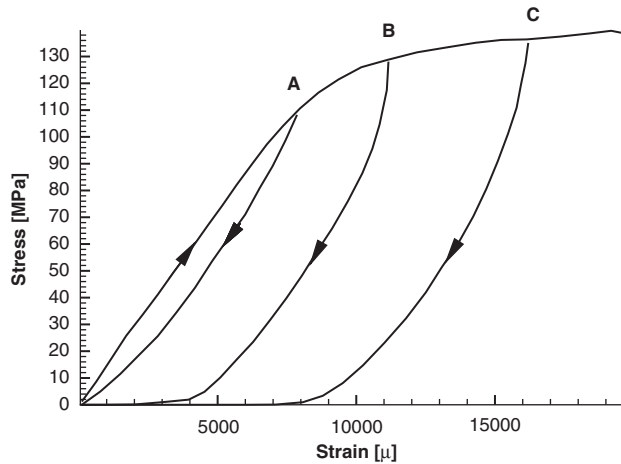
FIGURE 4.15 Bone shows hysteresis and shifting of stress-strain curves with repeated loading and unloading. *Adapted from [2].*

Figure 4.15 shows that the elastic properties of bone also vary depending on whether the load is being applied or removed, displaying hysteresis. From a thermodynamic view, the energy stored in the bone during loading is not equal to the energy released during unloading. This energy difference becomes greater as the maximum load increases (curves A to B to C). The "missing" energy is dissipated as heat due to internal friction and damage to the material at high loads.

The anisotropic nature of bone is sufficient in that its ultimate stress in compression is 200 MPa, while in tension it is only 140 MPa and in torsion 75 MPa. For torsional loading, the *shear modulus* or *modulus of rigidity*, denoted G, relates the shear stress to the shear strain. The modulus of rigidity is related to the elastic modulus via *Poisson's ratio*, v, where

$$v = \frac{\varepsilon_{\text{transverse}}}{\varepsilon_{\text{longitudinal}}} \tag{4.51}$$

Typically, $v \approx 0.3$, meaning that longitudinal deformation is three times greater than transverse deformation. For linearly elastic materials, E, G, and v are related by

$$G = \frac{E}{2(1 + v)} \tag{4.52}$$

One additional complexity of predicting biomaterial failure is the complexity of physiological loading. For example, consider "boot-top" fractures in skiing. If the forward motion of a skier is abruptly slowed or stopped, such as by suddenly running into wet or soft snow, his forward momentum causes a moment over the ski boot top, producing three-point bending of the tibia. In this bending mode the anterior tibia undergoes compression, while the posterior is in tension and potentially in failure, since bone is much stronger in compression than in tension. Contraction of the triceps surae muscle produces high compressive stress at the posterior side, reducing the amount of bone tension and helping to prevent injury. Example Problem 4.9 shows how topics from statics and mechanics of materials may be applied to biomechanical problems.

EXAMPLE PROBLEM 4.9

Figure 4.16 (left) shows an orthopedic nail-plate used to fix an intertrochanteric fracture. The hip applies an external force of 400 N during static standing, as shown. The nail-plate is rectangular stainless steel with cross-sectional dimensions of 10 mm (width) by 5 mm (height), and is well-fixed with screws along its vertical axis and friction fit into the trochanteric head (along the x-axis). What forces, moments, stresses, and strains will develop in this orthopedic device?

Solution

As for any statics problem, the first task is constructing a free-body diagram, including all applied forces and moments and all reaction forces and moments that develop at the supports. Because of the instability at the fracture site, the nail-plate may be required to carry the entire 400 N load. Consequently, one reasonable model of the nail-plate is a cantilever beam of length 0.06 m with a combined loading, as depicted in Figure 4.16 (right, top). The applied 400 N load consists of both axial and transverse components:

$$F_x = 400 \text{ N} \cos 20° = 376 \text{ N}$$
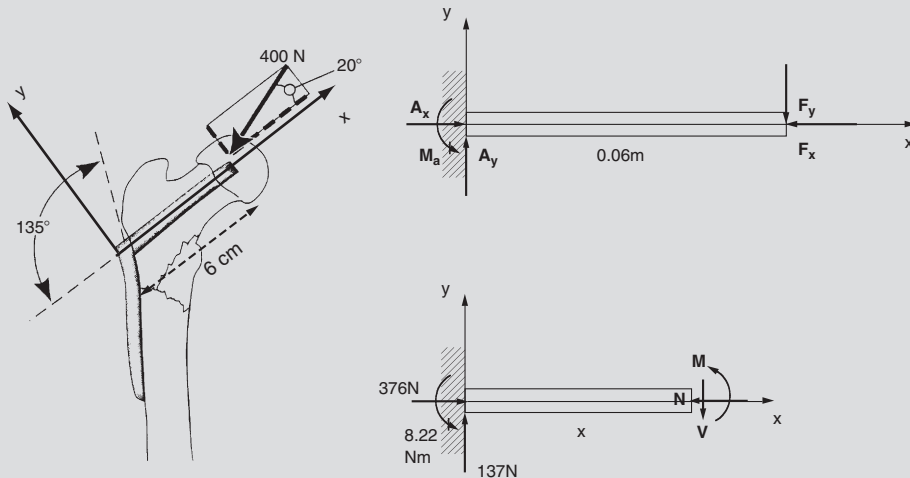$$F_y = 400 \text{ N} \sin 20° = 137 \text{ N}$$

FIGURE 4.16 (Left) An intertrochanteric nail plate used in bone repair. To the right is the free-body diagram of the upper section of this device, and below it is the free-body diagram of a section of this beam cut at a distance x from the left-hand support. *Adapted from [2].*

The axial load produces compressive normal stress; from Eq. (4.47),

$$\sigma_x = \frac{F_x}{A}$$

$$= \frac{376 \text{ N}}{(0.005 \text{ m})(0.01 \text{ m})} = 7.52 \text{ MPa}$$

in compression, which is only about 1 percent of the yield stress for stainless steel (see Table 4.2). The maximum shear stress due to the axial load is

$$\tau_{max} = \frac{\sigma_x}{2} = 3.76 \text{ MPa}$$

and occurs at $45°$ from the long axis. The axial strain can be computed using the elastic modulus for stainless steel,

$$E = \frac{\sigma}{\varepsilon} = \frac{F/A}{\Delta\ell/\ell}$$

giving an expression for strain:

$$\varepsilon = \frac{F}{EA}$$

$$= \frac{376 \text{ N}}{180 \times 10^9 \text{Pa}(0.005 \text{ m})(0.01 \text{ m})} = 41.8 \times 10^{-6}$$

From this strain the axial deformation can be computed

$$\Delta\ell_{axial} = \varepsilon\ell = 2.51 \times 10^{-6}\text{m}$$

which is negligible.

The transverse load causes the cantilever section to bend. The equations describing beam bending can be found in any mechanics of materials text (e.g., [26]). Consider the beam in the left panel of Figure 4.17. If this beam is fixed at the left-hand side and subjected to a downward load on the right, it will bend with the top of the beam elongating and the bottom shortening. Consequently, the top of the beam is in tension, and the bottom in compression. The point of transition, where there is no bending force, is denoted the neutral axis, located at distance c. For a symmetric rectangular beam of height h, c is located at the midline $h/2$. The beam resists bending via its area moment of inertia I. For a rectangular cross section of width b and height h, $I = \frac{1}{12}bh^3$, depicted in the right panel of Figure 4.17.

Beam tip deflection δy is equal to
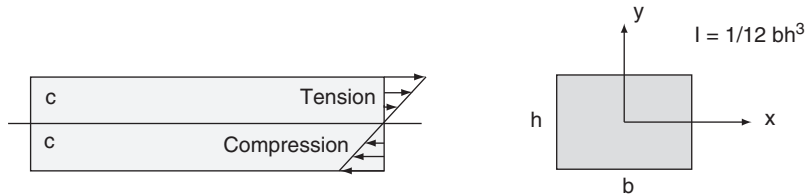
$$\delta y = \frac{Fx^2}{6EI}(3L - x) \tag{4.53}$$

FIGURE 4.17 (Left) A beam fixed on the left and subjected to a downward load on the right undergoes bending, with the top of the beam in tension and the bottom in compression. The position where tension changes to compression is denoted the neutral axis, located at c. (Right) A beam of rectangular cross section with width b and height h resists bending via the area moment of inertia $I = \frac{1}{12}bh^3$.

where x is the axial distance along the beam, L is the total beam length, and I is the beam's cross-sectional area moment of inertia. For this example,

$$I = \frac{1}{12}(10 \times 10^{-3} \text{ m})(5 \times 10^{-3} \text{ m})^3 = 1.042 \times 10^{-10} \text{ m}^4$$

Maximum deflection will occur at $x = L$,

$$\delta y_{\max} = \frac{FL^3}{3EI}$$

$$= \frac{137 \text{ N}(0.06 \text{ m})^3}{3(180 \times 10^9 \text{N/m}^2)(1.042 \times 10^{-10}\text{m}^4)} \tag{4.54}$$

$$= 5.26 \times 10^{-4} \text{ m} = 0.526 \text{ mm}$$

which is also negligible.

Computation of maximum shear and bending stresses requires maximum shear force V and bending moment M. Starting by static analysis of the entire free-body

$$\sum F_x \quad : \quad A_x - 376 \text{ N} = 0$$

$$\sum F_y \quad : \quad A_y - 137 \text{ N} = 0$$

$$\sum M_A \quad : \quad M_a - 137 \text{ N}(0.06 \text{ m}) = 0$$

Solving these equations gives $A_x = 376$ N, $A_y = 137$ N, and $M_a = 8.22$ N m. Taking a cut at any point x to the right of A and isolating the left-hand section gives the free-body in Figure 4.16 (right, bottom). Applying the equations of static equilibrium to this isolated section yields

$$\sum F_x \quad : \quad 376 \text{ N} - N = 0$$

$$N(x) \quad = \quad 376 \text{ N}$$

$$\sum F_y \quad : \quad 137 \text{ N} - V = 0$$

$$V(x) \quad = \quad 137 \text{ N}$$

$$\sum M_A \quad : \quad 8.22 \text{ N m} - (137 \text{ N})(x \text{ m}) + M = 0$$

$$M(x) \quad = \quad (137 \text{ N m})x - 8.22 \text{ N m}$$

These last equations can be plotted easily using MATLAB, giving the axial force, shear force, and bending moment diagrams shown in Figure 4.18.

```
% Use MATLAB to plot axial force, shear force and bending moment
% diagrams for Example Problem 9

x = [0:0.01:0.06];
N = x.*0 + 376;
```

```
V = x.*0 + 137;
M = 137.*x − 8.22;

figure
subplot(3,1,1), plot(x,N,x,N,'x')
xlabel('x [m]')
ylabel('N [N]')
title('Axial Force N')
subplot(3,1,2), plot(x,V,x,V,'x')
xlabel('x [m]')
ylabel('V [N]')
title('Shear Force V')
subplot(3,1,3), plot(x,M,x,M,'x')
xlabel('x [m]')
ylabel('M [N−m]')
title('Bending Moment M')
```
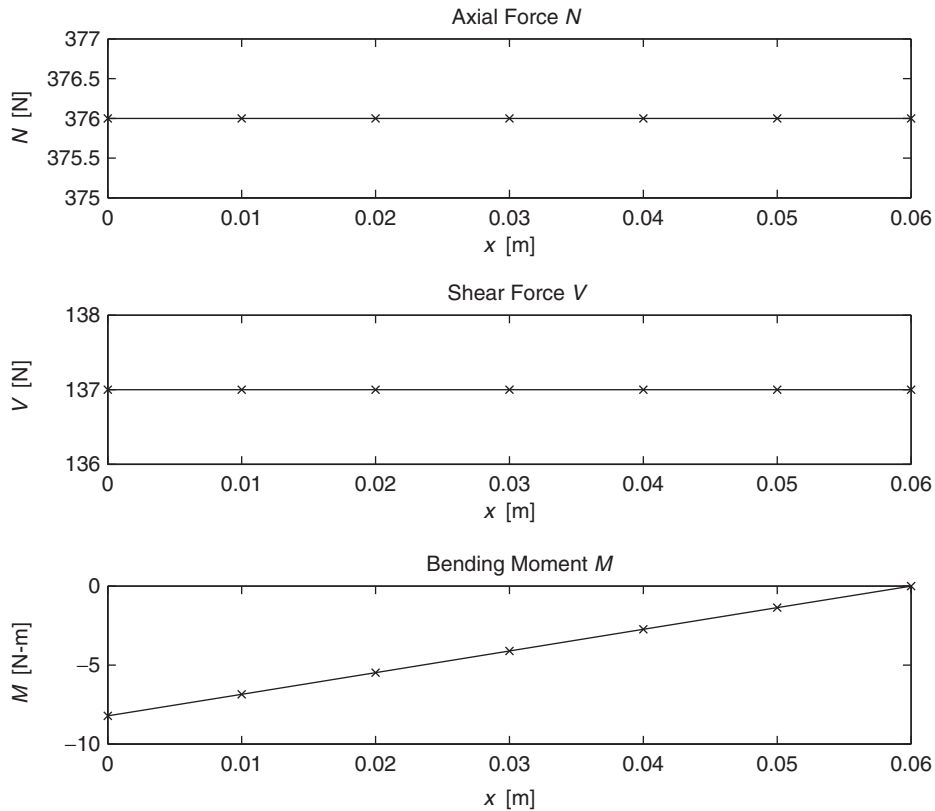

FIGURE 4.18 Axial force N (top), shear force V (middle), and bending moment M (bottom) computed for the nail plate in Figure 4.16 as functions of the distance x along the plate.

The maximum bending and shear stresses follow as

$$\sigma_{b\max} = \frac{M_{\max}c}{I} \tag{4.55}$$

where c, the distance to the beam's neutral axis, is $h/2$ for this beam:

$$\sigma_{b\max} = \frac{-8.22\ \text{Nm}[0.5(5 \times 10^{-3}\ \text{m})]}{1.042 \times 10^{-10}\ \text{m}^4} = -197\ \text{MPa}$$

$$\tau_{b\max} = \frac{V_{\max}h^2}{8I} \tag{4.56}$$

$$= \frac{137\ \text{N}(5 \times 10^{-3}\ \text{m})^2}{8(1.042 \times 10^{-10}\ \text{m}^4)} = 4.11\ \text{MPa}$$

All of these stresses are well below $\sigma_{\text{yield}} = 700\ \text{MPa}$ for stainless steel.

4.4 VISCOELASTIC PROPERTIES

The Hookean elastic solid is a valid description of materials only within a narrow loading range. For example, an ideal spring that relates force and elongation by a spring constant k is invalid in nonlinear low-load and high-load regions. Further, if this spring is coupled to a mass and set into motion, the resulting perfect harmonic oscillator will vibrate forever, which experience shows does not occur. Missing is a description of the system's viscous or damping properties. In this case, energy is dissipated as heat in the spring and air friction on the moving system.

Similarly, biomaterials all display viscoelastic properties. Different models of viscoelasticity have been developed to characterize materials with simple constitutive equations. For example, Figure 4.19 shows three such models that consist of a series ideal spring and dashpot (Maxwell), a parallel spring and dashpot (Voight), and a series spring and dashpot with a parallel spring (Kelvin). Each body contains a dashpot, which generates force in proportion to the derivative of its elongation. Consequently, the resulting models exhibit stress and strain properties that vary in time.

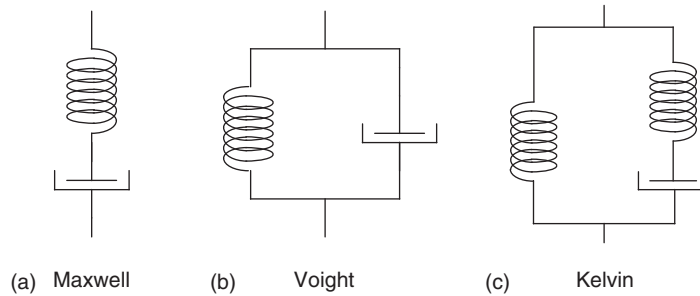(a) Maxwell   (b)   Voight   (c)   Kelvin

FIGURE 4.19   Three simple viscoelastic models: (a) the Maxwell model, (b) the Voight model, and (c) the Kelvin body or standard linear solid model.

The dynamic response of each model can be quantified by applying a step change in force F and noting the model's resulting change in length, or position x, denoted the *creep* response. The converse experiment applies a step change in x and measures the resulting change in F, denoted *stress relaxation*. Creep and stress relaxation tests for each dynamic model can be carried out easily using the Simulink program. Figure 4.20 shows a purely elastic material subjected to a step change in applied force F. The material's subsequent position x follows the change in force directly. This material exhibits no creep. Figure 4.21 shows the purely elastic material subjected to a step change in position x. Again, the material responds immediately with a step change in F (i.e., no stress relaxation is observed).

James Clerk Maxwell (1831–1879) used a series combination of ideal spring and dashpot to describe the viscoelastic properties of air. Figure 4.22 shows the Maxwell viscoelastic model subjected to a step change in applied force, and Figure 4.23 shows the Maxwell model's stress relaxation response. The latter exhibits an initial high stress followed by stress relaxation back to the initial stress level. The creep response, however, shows that this model is not bounded in displacement, since an ideal dashpot may be extended forever.

Woldemar Voight (1850–1919) used the parallel combination of an ideal spring and dashpot in his work with crystallography. Figure 4.24 shows the creep test of the Voight viscoelastic model. Figure 4.25 shows that this model is unbounded in force. That is, when a step change in length is applied, force goes to infinity, since the dashpot cannot immediately respond to the length change.

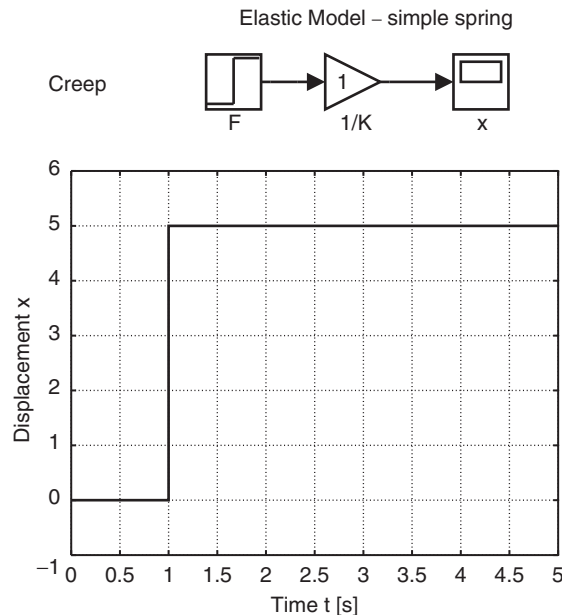**FIGURE 4.20** Simulink model of the creep test for a purely elastic material (an ideal spring). This model solves the equation $x=F/K$, where x is displacement, F is applied force, and K is the spring constant. Below is the elastic creep response to a step increase in applied force F with $K=1$ and force changed from 0 to 5 (arbitrary units). The displacement x linearly follows the applied force.
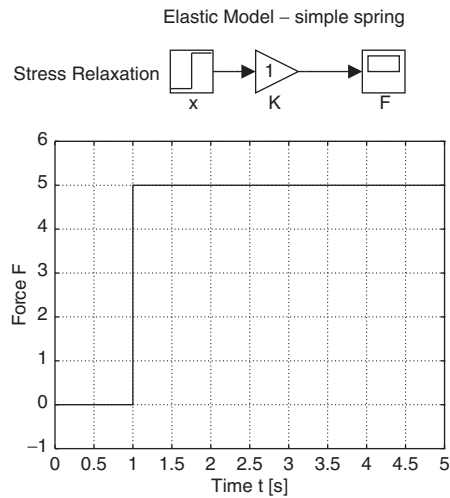
Elastic Model – simple spring

FIGURE 4.21   Simulink model (top) and stress relaxation test of the purely elastic model, which solves $F=Kx$. Applied step displacement $x=5$ and spring constant $K=1$. Force linearly follows displacement.

Maxwell Model of Viscoelasticity – series spring and dashpot

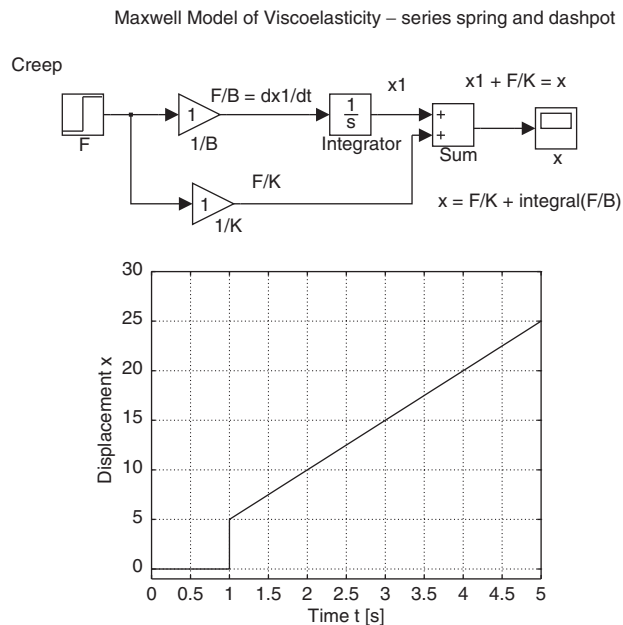**FIGURE 4.22**   Creep of the Maxwell viscoelastic model, a series combination of ideal spring and dashpot (Figure 4.19a). The spring constant $K=1$, and dashpot damping coefficient $B=1$ (arbitrary units). This system is subjected to a step change in force, and displacement x arises by solving $x = F/K + \int F/B$. The spring instantly responds, followed by creep of the ideal dashpot, which may extend as long as force is applied.
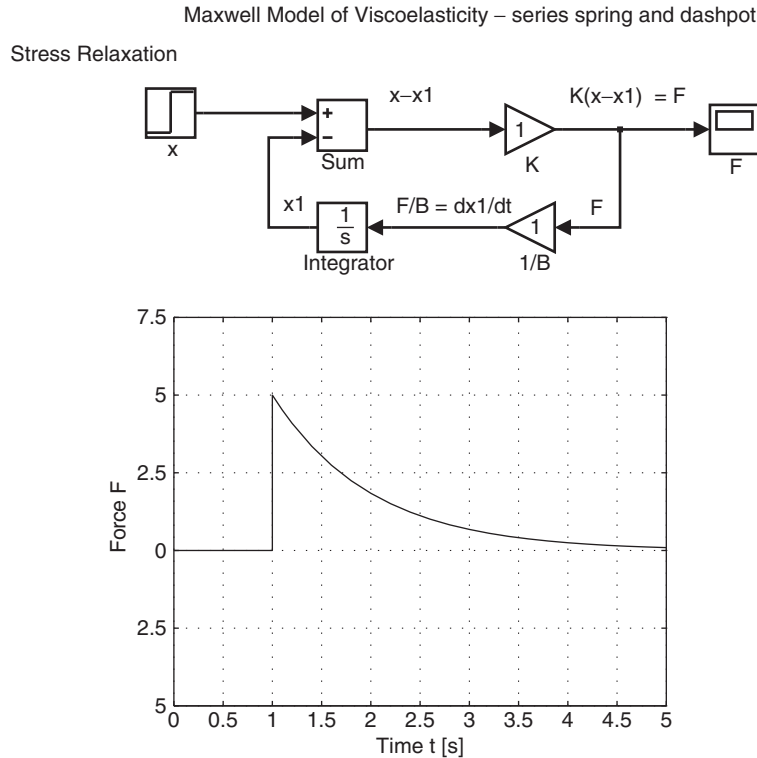
FIGURE 4.23 Stress relaxation of the Maxwell viscoelastic model. This model solves $F = K[x - \int F/B]$, again with $K=B=1$ and arbitrary units. The ideal spring instantly responds followed by stress relaxation via the dashpot to the steady-state force level.

William Thompson (Lord Kelvin, 1824–1907) used the three-element viscoelastic model (Figure 4.19c) to describe the mechanical properties of different solids in the form of a torsional pendulum. Figure 4.26 shows the three-element Kelvin model's creep response. This model has an initial rapid jump in position with subsequent slow creep. Figure 4.27 shows the Kelvin model stress relaxation test. Initially, the material is very stiff, with subsequent stress decay to a nonzero steady-state level that is due to the extension of the dashpot. The three-element Kelvin model is the simplest lumped viscoelastic model that is bounded both in extension and force.

The three-element viscoelastic model describes the basic features of stress relaxation and creep. Biological materials often exhibit more complex viscoelastic properties. For example, plotting hysteresis as a function of frequency of applied strain gives discrete curves for the lumped viscoelastic models. Biological tissues demonstrate broad, distributed hysteresis properties. One solution is to describe biomaterials with a distributed network of three-element models. A second method is to use the generalized viscoelastic model of Westerhof and Noordergraaf (1970) to describe the viscoelastic wall properties of blood vessels. Making the elastic modulus mathematically complex yields a model that includes the frequency dependent elastic modulus, stress relaxation, creep, and hysteresis exhibited by arteries. Further, the Voight and Maxwell models emerge as special (limited) cases of this general approach.

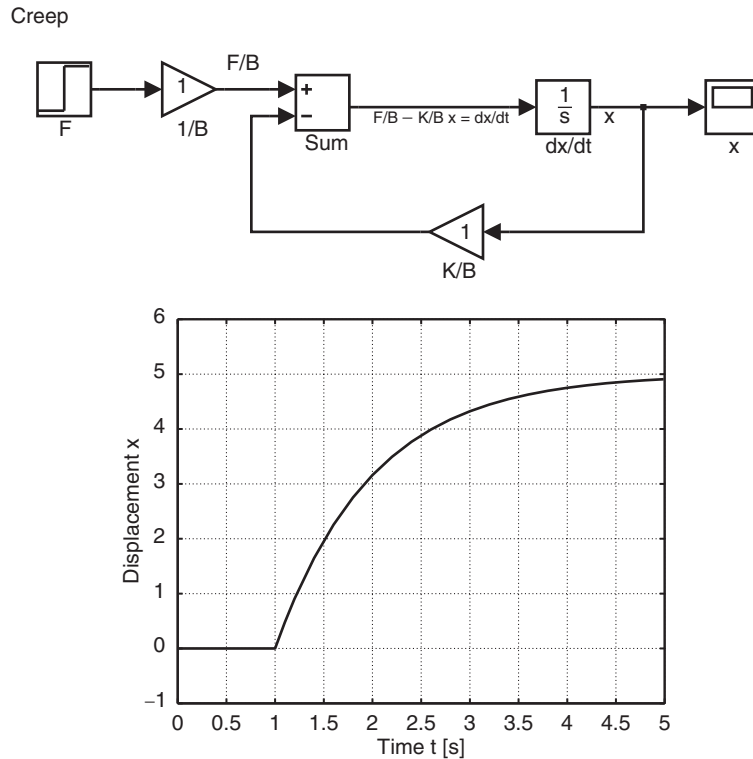Voight Model of Viscoelasticity – parallel spring and dashpot

Creep

FIGURE 4.24   Creep of the Voight viscoelastic model, a parallel combination of ideal spring and dashpot (Figure 4.19b). This model solves the differential equation $dx/dt = 1/B[F - Kx]$ for x. $K=B=1$, and the step applied force is 5 arbitrary units. Displacement slowly creeps toward its steady-state value.

4.5   CARTILAGE, LIGAMENT, TENDON, AND MUSCLE

The articulating surfaces of bones are covered with articular cartilage, a biomaterial composed mainly of collagen. Collagen is the main structural material of hard and soft tissues in animals. Isolated collagen fibers have high tensile strength that is comparable to nylon (50–100 MPa) and an elastic modulus of approximately 1 GPa. Elastin is a protein found in vertebrates and is particularly important in blood vessels and the lungs. Elastin is the most linearly elastic biosolid known, with an elastic modulus of approximately 0.6 MPa. It gives skin and connective tissue their elasticity.

4.5.1   Cartilage

Cartilage serves as the bearing surfaces of joints. It is porous, and its complex mechanical properties arise from the motion of fluid in and out of the tissue when subjected to joint loading. Consequently, articular cartilage is strongly viscoelastic, with stress relaxation times

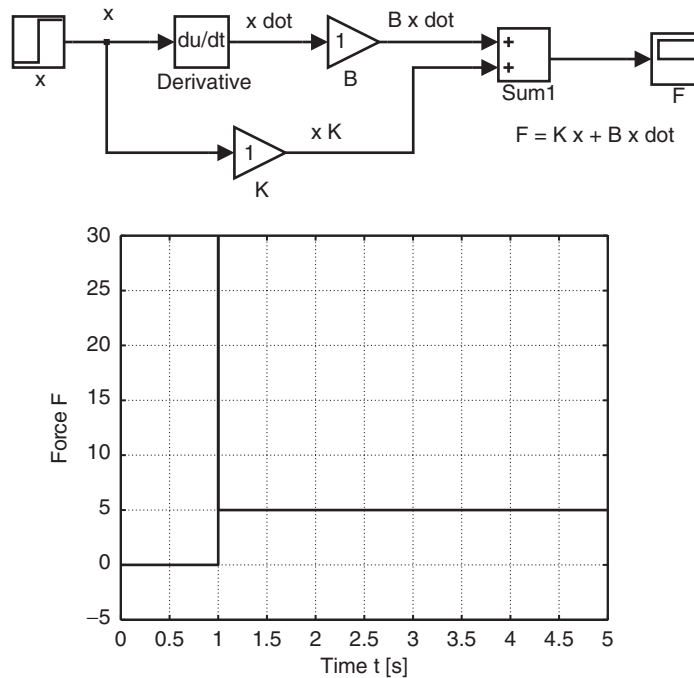Voight Model of Viscoelasticity – parallel spring and dashpot

Stress Relaxation

FIGURE 4.25 Stress relaxation of the Voight viscoelastic model. This model solves the equation $F = Kx + Bdx/dt$. Since the dashpot is in parallel with the spring, and since it cannot respond immediately to a step change in length, the model force goes to infinity.

in compression on the order of 1 to 5 seconds. Cartilage is anisotropic and displays hysteresis during cyclical loading. The ultimate compressive stress of cartilage is on the order of 5 MPa.

4.5.2 Ligaments and Tendons

Ligaments join bones together and consequently serve as part of the skeletal framework. Tendons join muscles to bones and transmit forces generated by contracting muscles to cause movement of the jointed limbs. Tendons and ligaments primarily transmit tension, so they are composed mainly of parallel bundles of collagen fibers and have similar mechanical properties. Human tendon has an ultimate stress of 50–100 MPa and exhibits very nonlinear stress-strain curves. The middle stress-strain range is linear, with an elastic modulus of approximately 1–2 GPa. Both tendons and ligaments exhibit hysteresis, viscoelastic creep, and stress relaxation. These materials may also be "preconditioned," whereby initial tensile loading can affect subsequent load-deformation curves. The material properties shift due to changes in the internal tissue structure with repeated loading.
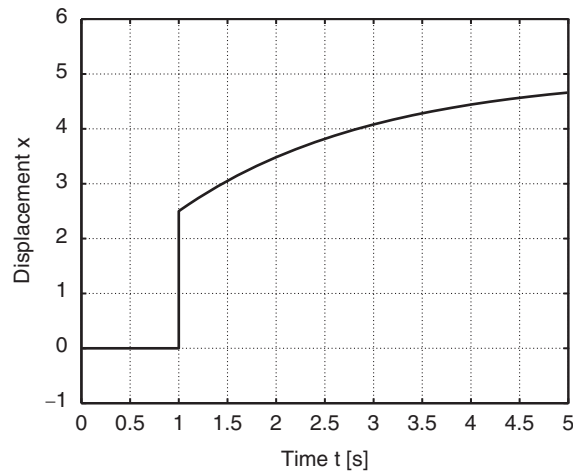
FIGURE 4.26   Creep of the Kelvin three-element viscoelastic model. This model's equations of motion are left to the reader to derive. After a step change in force, this model has an initial immediate increase in displacement, with a subsequent slow creep to a steady-state level.
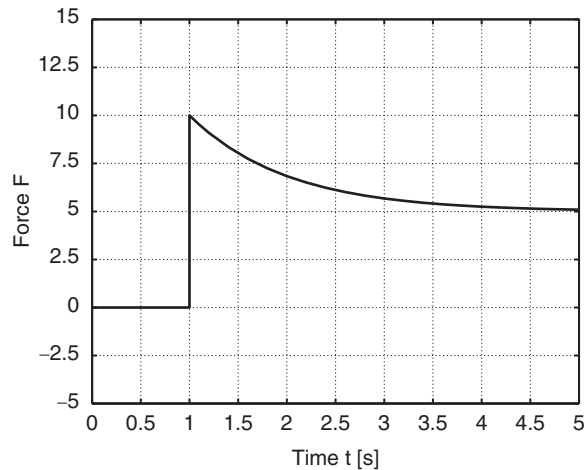
FIGURE 4.27   Stress relaxation of the Kelvin viscoelastic model. This model has an initial immediate increase in force followed by slower stress relaxation to a steady-state force level.

4.5.3 Muscle Mechanics

Chapter 3 introduced muscle as an active, excitable tissue that generates force by forming cross-bridge bonds between the interdigitating actin and myosin myofilaments. The quantitative description of muscle contraction has evolved into two separate foci: lumped descriptions based on A. V. Hill's contractile element and cross-bridge models based on A. F. Huxley's description of a single sarcomere [22]. The earliest quantitative descriptions of muscle are lumped whole muscle models, with the simplest mechanical description being a

purely elastic spring. Potential energy is stored when the spring is stretched, and shortening occurs when it is released. The idea of muscle elastance can be traced back to Ernst Weber [29], who considered muscle as an elastic material that changes state during activation via conversion of chemical energy. Subsequently, investigators retained the elastic description but ignored metabolic alteration of muscle stiffness. A purely elastic model of muscle can be refuted on thermodynamic grounds, since the potential energy stored during stretching is less than the sum of the energy released during shortening as work and heat. Still, efforts to describe muscle by a combination of traditional springs and dashpots continued. In 1922, Hill coupled the spring with a viscous medium, thereby reintroducing viscoelastic muscle descriptions that can be traced back to the 1840s.

Quick stretch and release experiments show that muscle's viscoelastic properties are strongly time dependent. In general, the faster a change in muscle length occurs, the more severely the contractile force is disturbed. Muscle contraction clearly arises from a more sophisticated mechanism than a damped elastic spring. In 1935, Fenn and Marsh added a series elastic element to Hill's damped elastic model and concluded that "muscle cannot properly be treated as a simple mechanical system." Subsequently, Hill embodied the empirical hyperbolic relation between load and initial velocity of shortening for skeletal muscle as a model building block, denoted the contractile element. Hill's previous viscoelastic model considered muscle to possess a fixed amount of potential energy whose rate of release is controlled by viscosity. Energy is now thought to be controlled by some undefined internal mechanism rather than by friction. This new feature of muscle dynamics varying with load was a step in the right direction; however, subsequent models, including heart studies, built models based essentially on the hyperbolic curve that was measured for tetanized skeletal muscle. This approach can be criticized on two grounds: (1) embodiment of the contractile element by a single force-velocity relation sets a single, fixed relation between muscle energetics and force; and (2) it yields no information on the contractile mechanism behind this relation. Failure of the contractile element to describe a particular loading condition led investigators to add passive springs and dashpots liberally, with the number of elements reaching at least nine by the late 1960s. Distributed models of muscle contraction, generally, have been conservative in design and have depended fundamentally on the Hill contractile element. Recent models are limited to tetanized, isometric contractions or to isometric twitch contractions.

A second, independent focus of muscle contraction research works at the ultrastructural level, with the sliding filament theory serving as the most widely accepted contraction mechanism. Muscle force generation is viewed as the result of crossbridge bonds formed between thick and thin filaments at the expense of biochemical energy. The details of bond formation and detachment are under considerable debate, with the mechanism for relaxation particularly uncertain. Prior to actual observation of crossbridges, A. F. Huxley [13] devised the crossbridge model based on structural and energetic assumptions. Bonds between myofilaments are controlled via rate constants f and g that dictate attachment and detachment, respectively. One major shortcoming of this idea was the inability to describe transients resulting from rapid changes in muscle length or load, similar to the creep and stress relaxation tests previously discussed.

Subsequent models adopt increasingly complex bond attachment and detachment rate functions and are often limited in scope to description of a single pair of myofilaments. Each tends

to focus on description of a single type of experiment. No model has been shown to broadly describe all types of contractile loading conditions. Crossbridge models have tended to rely on increasingly complex bond attachment and detachment rate functions. This trend has reversed the issue of describing complex muscle dynamics from the underlying, simpler cross-bridges to adopting complex crossbridge dynamics to describe a particular experiment.

Alternatively, Palladino and Noordergraaf [22] proposed a large-scale, distributed muscle model that manifests both contraction and relaxation as the result of fundamental mechanical properties of crossbridge bonds. As such, muscle's complex contractile properties emerge from its underlying ultrastructure dynamics—that is, function follows from structure. Bonds between myofilaments, which are biomaterials, are described as viscoelastic material. The initial stimulus for contraction is electrical. Electrical propagation through cardiac muscle occurs at finite speed, implying spatial asynchrony of stimulation. Furthermore, Ca^{++} release from the sarcoplasmic reticulum depends on diffusion for availability at the myosin heads. These effects, as well as nonuniformity of structure, strongly suggest that contraction is asynchronous throughout the muscle. Recognition of muscle's distributed properties by abandoning the assumption of perfect synchrony in contraction and consideration of myofilament mass allow for small movements of thick with respect to thin filaments. Such movements lead to bond detachment and heat production. Gross movement such as muscle shortening exacerbates this process. Quick transients in muscle length or applied load have particularly strong effects and have been observed experimentally. Muscle relaxation is thereby viewed as a consequence of muscle's distributed properties.

The distributed muscle model is built from the following main features: sarcomeres consist of overlapping thick and thin filaments connected by crossbridge bonds that form during activation and detach during relaxation. Figure 4.28 shows a schematic of a muscle fiber composed of a string of series sarcomeres. Crossbridge bonds are each described as three-element viscoelastic solids, and myofilaments as masses. Force is generated due to viscoelastic crossbridge bonds that form and are stretched between the interdigitating matrix of myofilaments.
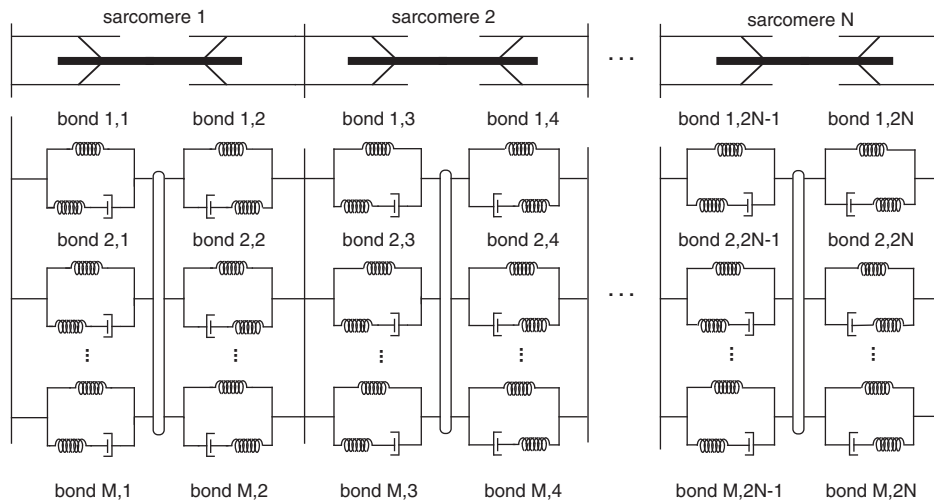

FIGURE 4.28 Schematic diagram of a muscle fiber built from a distributed network of N sarcomeres. Each sarcomere has M parallel pairs of crossbridge bonds. *Adapted from [22].*

The number of bonds formed depends on the degree of overlap between thick and thin filaments and is dictated spatially and temporally due to finite electrical and chemical activation rates. Asynchrony in bond formation and unequal numbers of bonds formed in each half sarcomere, as well as mechanical disturbances such as muscle shortening and imposed length transients, cause small movements of the myofilaments. Since myofilament masses are taken into account, these movements take the form of damped vibrations with a spectrum of frequencies due to the distributed system properties. When the stress in a bond goes to zero, the bond detaches. Consequently, myofilament motion and bond stress relaxation lead to bond detachment and produce relaxation without assumption of bond detachment rate functions. In essence, relaxation results from inherent system instability. Although the model is built from linear, time-invariant components (springs, dashpots, and masses), the highly dynamic structure of the model causes its mechanical properties to be highly nonlinear and time-varying, as is found in muscle fibers and strips.

Sensitivity of the model to mechanical disturbances is consistent with experimental evidence from muscle force traces, aequorin measurements of free calcium ion, and high-speed x-ray diffraction studies, which all suggest enhanced bond detachment. The model is also consistent with sarcomere length feedback studies in which reduced internal motion delays relaxation, and it predicted muscle fiber (cell) dynamics prior to their experimental measurement.

This model proposes a structural mechanism for the origin of muscle's complex mechanical properties and predicts new features of the contractile mechanism—for example, a mechanism for muscle relaxation and prediction of muscle heat generation. This approach computes muscle's complex mechanical properties from physical description of muscle anatomical structure, thereby linking subcellular structure to organ-level function.

This chapter describes some of the high points of biological tissues' mechanical properties. More comprehensive references include Fung's *Biomechanics: Mechanical Properties of Living Tissues*, Nigg and Herzog's *Biomechanics of the Musculo-Skeletal System*, and Mow and Hayes's *Basic Orthopaedic Biomechanics*. Muscle contraction research has a long history, as chronicled in the book *Machina Carnis* by Needham. For a more comprehensive history of medicine, see Singer and Underwood's book. The next two sections apply biomechanics concepts introduced in Sections 4.2–4.5 to human gait analysis and to the quantitative study of the cardiovascular system.

4.6 CLINICAL GAIT ANALYSIS

An example of applied dynamics in human movement analysis is clinical gait analysis. Clinical gait analysis involves the measurement of the parameters that characterize a patient's gait pattern, the interpretation of the collected and processed data, and the recommendation of treatment alternatives. It is a highly collaborative process that requires the cooperation of the patient and the expertise of a multidisciplinary team that typically includes a physician, a physical therapist or kinesiologist, and an engineer or technician. The engineer is presented with a number of challenges. The fundamental objective in data collection is to monitor the patient's movements accurately and with sufficient precision for clinical use without altering the patient's typical performance. While measurement devices for clinical gait analysis are established to some degree and are commercially available, the

protocols for the use of the equipment continue to develop. The validity of these protocols and associated models and the care with which they are applied ultimately dictate the meaning and quality of the resulting data provided for interpretation. This is one area in which engineers in collaboration with their clinical partners can have a significant impact on the clinical gait analysis process.

Generally, data collection for clinical gait analysis involves the placement of highly reflective markers on the surface of the patient's skin. These external markers reflect light to an array of video-based motion cameras that surround the measurement volume. The instantaneous location of each of these markers can then be determined stereometrically based on the images obtained simultaneously from two or more cameras. Other aspects of gait can be monitored as well, including ground reactions via force platforms embedded in the walkway and muscle activity via electromyography with either surface or intramuscular fine wire electrodes, depending on the location of the particular muscle.

In keeping with the other material presented in this chapter, the focus of this section will pertain to the biomechanical aspects of clinical gait analysis and includes an outline of the computation of segmental and joint kinematics and joint kinetics, and a brief illustration of how the data are interpreted.

4.6.1 The Clinical Gait Model

The gait model is the algorithm that transforms the data collected during walking trials into the information required for clinical interpretation. For example, the gait model uses the data associated with the three-dimensional displacement of markers on the patient to compute the angles that describe how the patient's body segment and lower-extremity joints are moving. The design of the gait model is predicated on a clear understanding of the needs of the clinical interpretation team—for example, the specific aspects of gait dynamics of interest. To meet these clinical specifications, gait model development is constrained both by the technical limitations of the measurement system and by the broad goal of developing protocols that may be appropriate for a wide range of patient populations that vary in age, gait abnormality, walking ability, and so on. An acceptable model must be sufficiently general to be used for many different types of patients (e.g., adults and children with varying physical and cognitive involvement), be sufficiently sophisticated to allow detailed biomechanical questions to be addressed, and be based on repeatable protocols that are feasible in a clinical setting.

4.6.2 Kinematic Data Analysis

Reflective markers placed on the surface of the patient's skin are monitored or tracked in space and time by a system of video-based cameras. These marker trajectories are used to compute coordinate systems that are anatomically aligned and embedded in each body segment under analysis. These anatomical coordinate systems provide the basis for computing the absolute spatial orientation, or attitude, of the body segment or the angular displacement of one segment relative to another, such as joint angles. For this analysis, at least three noncollinear markers or points of reference must be placed on or identified for each body segment included in the analysis. These markers form a plane from which a segmentally fixed coordinate system may be derived. Any three markers will allow the segment motion to be monitored, but unless these markers are referenced to the subject's anatomy, such

kinematic quantification is of limited clinical value. Markers must either be placed directly over palpable bony landmarks on the segment or at convenient (i.e., visible to the measurement cameras) locations on the segment that are referenced to the underlying bones. An examination of the pelvic and thigh segments illustrates these two alternatives.

Pelvic Anatomical Coordinate System

For the pelvis, markers placed over the right and left anterior-superior-iliac-spine (ASIS) and either the right or left posterior-superior-iliac-spine (PSIS) will allow for the computation of an anatomically aligned coordinate system, as described in Example Problem 4.10.

EXAMPLE PROBLEM 4.10

Given the following three-dimensional locations in meters for a set of pelvic markers expressed relative to an inertially fixed laboratory coordinate system (Figure 4.29),

$$\text{Right ASIS}: \mathbf{RASIS} = -0.850\mathbf{i} - 0.802\mathbf{j} + 0.652\mathbf{k}$$
$$\text{Left ASIS}: \mathbf{LASIS} = -0.831\mathbf{i} - 0.651\mathbf{j} + 0.652\mathbf{k}$$
$$\mathbf{PSIS} = -1.015\mathbf{i} - 0.704\mathbf{j} + 0.686\mathbf{k}$$

compute an anatomical coordinate system for the pelvis.

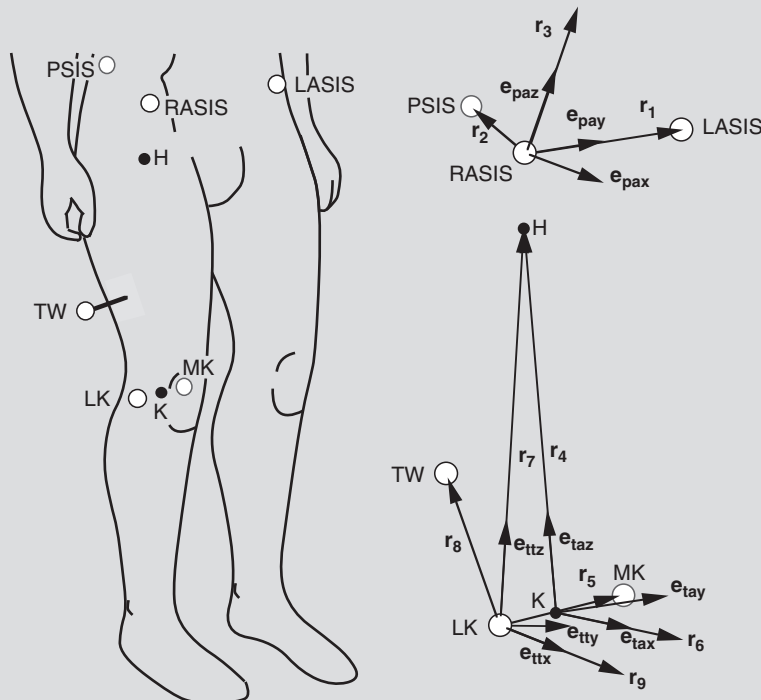FIGURE 4.29 Kinematic markers used to define pelvis and thigh coordinate systems. For the pelvis, PSIS denotes posterior-superior-iliac-spine, H is hip center, and RASIS and LASIS denote right and left anterior-superior-iliac-spine markers, respectively. For the thigh, TW is thigh wand, K is knee center, and MK and LK are medial and lateral knee (femoral condyle) markers, respectively.

Continued

Solution

These three anatomical markers form a plane. The line between the right ASIS and left ASIS represents one coordinate system axis. Another coordinate axis is perpendicular to the pelvic plane. The third coordinate axis is computed to be orthogonal to the first two:

1. Subtract vector **RASIS** from vector **LASIS**,

$$\textbf{LASIS} - \textbf{RASIS} = (-0.831 - (-0.850))\mathbf{i} + (-0.651 - (-0.802))\mathbf{j} + (0.652 - 0.652)\mathbf{k}$$

to find

$$\mathbf{r}_1 = 0.0190\mathbf{i} + 0.1510\mathbf{j} + 0.0000\mathbf{k}$$

and its associated unit vector:

$$\mathbf{e}_{r1} = \frac{0.019\mathbf{i} + 0.151\mathbf{j} + 0.000\mathbf{k}}{\sqrt{0.019^2 + 0.151^2 + 0.000^2}}$$

$$\mathbf{e}_{r1} = 0.125\mathbf{i} + 0.992\mathbf{j} + 0.000\mathbf{k}$$

Unit vector $\mathbf{e}_{r1}$ represents the medial-lateral direction or y-axis for the pelvic anatomical coordinate system $\mathbf{e}_{pay}$ (Figure 4.29).
2. A second vector in the pelvic plane is required to compute the coordinate axis that is perpendicular to the plane. Consequently, subtract vector **RASIS** from vector **PSIS** to find

$$\mathbf{r}_2 = -0.165\mathbf{i} + 0.098\mathbf{j} + 0.034\mathbf{k}$$

3. Take the vector cross product $\mathbf{e}_{pay} \times \mathbf{r}_2$ to yield

$$\mathbf{r}_3 = \begin{vmatrix} \mathbf{i} & \mathbf{j} & \mathbf{k} \\ 0.125 & 0.992 & 0.000 \\ -0.165 & 0.098 & 0.034 \end{vmatrix}$$

$$= [(0.992)(0.034) - (0.000)(0.098)]\mathbf{i}$$

$$+ [(0.000)(-0.165) - (0.125)(0.034)]\mathbf{j}$$

$$+ [(0.125)(0.098) - (0.992)(-0.165)]\mathbf{k}$$

$$= 0.034\mathbf{i} - 0.004\mathbf{j} + 0.176\mathbf{k}$$

and its associated unit vector:

$$\mathbf{e}_{r3} = \mathbf{e}_{paz} = 0.188\mathbf{i} - 0.024\mathbf{j} + 0.982\mathbf{k}$$

Unit vector $\mathbf{e}_{r3}$ represents the anterior-superior direction or z-axis of the pelvic anatomical coordinate system $\mathbf{e}_{paz}$ (Figure 4.29).
4. The third coordinate axis is computed to be orthogonal to the first two. Take the vector cross product $\mathbf{e}_{pay} \times \mathbf{e}_{paz}$ to compute the fore-aft direction, or x-axis, of the pelvic anatomical coordinate system:

$$\mathbf{e}_{pax} = 0.974\mathbf{i} - 0.123\mathbf{j} - 0.190\mathbf{k}$$

For this example, the anatomical coordinate system for the pelvis can be expressed as follows:

$$\{e_{pa}\} = \begin{bmatrix} e_{pax} \\ e_{pay} \\ e_{paz} \end{bmatrix} = \begin{bmatrix} 0.974 & -0.123 & -0.190 \\ 0.125 & 0.992 & 0.000 \\ 0.188 & -0.024 & 0.982 \end{bmatrix} \begin{bmatrix} i \\ j \\ k \end{bmatrix}$$

Note that the coefficients associated with these three axes represent the direction cosines that define the orientation of the pelvic coordinate system relative to the laboratory coordinate system.

In summary, by monitoring the motion of the three pelvic markers, the instantaneous orientation of an anatomical coordinate system for the pelvis, $\{e_{pa}\}$, comprising axes e_{pax}, e_{pay}, and e_{paz}, can be determined. The absolute angular displacement of this coordinate system can then be computed via Euler angles as pelvic tilt, obliquity, and rotation using Eqs. (4.32)–(4.34). An example of these angle computations is presented later in this section.

Thigh Anatomical Coordinate System

The thigh presents a more significant challenge than the pelvis because three bony anatomical landmarks are not readily available as reference points during gait. A model based on markers placed over the medial and lateral femoral condyles and the greater trochanter is appealing but ill-advised. A marker placed over the medial femoral condyle is not always feasible during gait—for example, with patients whose knees make contact while walking. A marker placed over the greater trochanter is often described in the literature but should not be used as a reference because of its significant movement relative to the underlying greater trochanter during gait—that is, skin motion artifact [3].

In general, the approach used to quantify thigh motion, and the shank and foot, is to place additional anatomical markers on the segments during a static subject calibration process. Then the relationship between these static anatomical markers, which are removed before gait data collection, and the motion markers that remain on the patient during gait data collection may be calculated. It is assumed that this mathematical relationship remains constant during gait—that is, the instrumented body segments are assumed to be rigid. This process is illustrated in the Example Problem 4.11.

EXAMPLE PROBLEM 4.11

Given the following marker coordinate data that have been acquired while the patient stands quietly, also in meters,

$$\text{lateral femoral condyle marker } \mathbf{LK} = -0.881i - 0.858j + 0.325k$$
$$\text{medial femoral condyle marker } \mathbf{MK} = -0.855i - 0.767j + 0.318k$$

compute an anatomical coordinate system for the thigh.

Solution

A thigh plane is formed based on three anatomical markers or points: the hip center, the lateral femoral condyle marker **LK**, and the medial femoral condyle marker **MK**. The knee center location can then be estimated as the midpoint between **LK** and **MK**. With these points, the vector

Continued

from the knee center to the hip center represents the longitudinal axis of the coordinate system. A second coordinate axis is perpendicular to the thigh plane. The third coordinate axis is computed to be orthogonal to the first two.

The location of the knee center of rotation may be approximated as the midpoint between the medial and lateral femoral condyle markers,

$$\frac{\mathbf{LK} + \mathbf{MK}}{2} = \frac{(-0.881) + (-0.855)}{2}\mathbf{i} + \frac{(-0.858) + (-0.767)}{2}\mathbf{j} + \frac{(0.325) + (0.318)}{2}\mathbf{k}$$

yielding

$$\text{knee center location } \mathbf{K} = -0.868\mathbf{i} - 0.812\mathbf{j} + 0.321\mathbf{k}$$

The location of the center of the head of the femur, referred to as the hip center, is approximated based either on patient anthropometry and a statistical model of pelvic geometry [6] or from data collected while the subject executes a specific hip movement [8]. In this example, the hip center can be located at approximately

$$\text{hip center location } \mathbf{H} = -0.906\mathbf{i} - 0.763\mathbf{j} + 0.593\mathbf{k}$$

Now the anatomical coordinate system for the thigh may be computed as follows:

1. Subtract the vector $\mathbf{K}$ from $\mathbf{H}$, giving

$$\mathbf{r}_4 = -0.038\mathbf{i} + 0.049\mathbf{j} + 0.272\mathbf{k}$$

and its associated unit vector

$$\mathbf{e}_{r4} = \mathbf{e}_{taz} = -0.137\mathbf{i} + 0.175\mathbf{j} + 0.975\mathbf{k}$$

Unit vector $\mathbf{e}_{r4}$ represents the longitudinal direction, or z-axis, of the thigh anatomical coordinate system $\mathbf{e}_{taz}$.
2. As with the pelvis, a second vector in the thigh plane is required to compute the coordinate axis that is perpendicular to the plane. Consequently, subtract vector $\mathbf{LK}$ from $\mathbf{MK}$:

$$\mathbf{r}_5 = 0.026\mathbf{i} + 0.091\mathbf{j} - 0.007\mathbf{k}$$

3. Form the vector cross product $\mathbf{r}_5 \times \mathbf{e}_{taz}$ to yield

$$\mathbf{r}_6 = 0.090\mathbf{i} - 0.024\mathbf{j} + 0.017\mathbf{k}$$

and its associated unit vector

$$\mathbf{e}_{r6} = \mathbf{e}_{tax} = 0.949\mathbf{i} - 0.258\mathbf{j} + 0.180\mathbf{k}$$

Unit vector $\mathbf{e}_{r6}$ represents the fore-aft direction, or x-axis, of the thigh anatomical coordinate system $\mathbf{e}_{tax}$.
4. Again, the third coordinate axis is computed to be orthogonal to the first two. Determine the medial-lateral or y-axis of the thigh anatomical coordinate system, $\mathbf{e}_{tay}$, from the cross product $\mathbf{e}_{taz} \times \mathbf{e}_{tax}$:

$$\mathbf{e}_{tay} = 0.284\mathbf{i} + 0.950\mathbf{j} - 0.131\mathbf{k}$$

For this example, the anatomical coordinate system for the thigh can be expressed as

$$\{e_{ta}\} = \begin{bmatrix} e_{tax} \\ e_{tay} \\ e_{taz} \end{bmatrix} = \begin{bmatrix} 0.949 & -0.258 & 0.180 \\ 0.284 & 0.950 & -0.131 \\ -0.137 & 0.175 & 0.975 \end{bmatrix} \begin{bmatrix} i \\ j \\ k \end{bmatrix}$$

This defines an anatomical coordinate system fixed to the thigh, $\{e_{ta}\}$, comprising axes e_{tax}, e_{tay}, and e_{taz}. Its basis, however, includes an external marker (medial femoral condyle **MK**) that must be removed before the walking trials. Consequently, the location of the knee center cannot be computed as described in the preceding example. This dilemma is resolved by placing another marker on the surface of the thigh such that it also forms a plane with the hip center and lateral knee marker. These three reference points can then be used to compute a "technical" coordinate system for the thigh to which the knee center location may be mathematically referenced.

EXAMPLE PROBLEM 4.12

Continuing Example Problem 4.11, and given the coordinates of another marker placed on the thigh but not anatomically aligned,

thigh wand marker $\mathbf{TW} = -0.890\mathbf{i} - 0.937\mathbf{j} + 0.478\mathbf{k}$

compute a technical coordinate system for the thigh.

Solution

A technical coordinate system for the thigh can be computed as follows:

1. Compute the longitudinal direction, or z-axis, of the technical thigh coordinate system e_{tt}. Start by subtracting vector **LK** from the hip center **H** to form

$$\mathbf{r_7} = -0.025\mathbf{i} + 0.094\mathbf{j} + 0.268\mathbf{k}$$

and its associated unit vector

$$\mathbf{e_{r7}} = \mathbf{e_{ttz}} = -0.088\mathbf{i} + 0.330\mathbf{j} + 0.940\mathbf{k}$$

Unit vector $\mathbf{e_{r7}}$ represents the z-axis of the thigh technical coordinate system, $\mathbf{e_{ttz}}$.

2. To compute the axis that is perpendicular to the plane formed by **LK**, **H**, and **TW**, subtract vector **LK** from **TW** to compute

$$\mathbf{r_8} = -0.009\mathbf{i} - 0.079\mathbf{j} + 0.153\mathbf{k}$$

3. Calculate the vector cross product $\mathbf{r_7} \times \mathbf{r_8}$ to yield

$$\mathbf{r_9} = 0.036\mathbf{i} + 0.001\mathbf{j} + 0.003\mathbf{k}$$

with its associated unit vector

$$\mathbf{e_{r9}} = \mathbf{e_{ttx}} = 0.996\mathbf{i} + 0.040\mathbf{j} + 0.079\mathbf{k}$$

Unit vector $\mathbf{e_{r9}}$ represents the fore-aft direction, or x-axis, of the thigh technical coordinate system e_{ttx}.

Continued

4. The third coordinate axis is computed to be orthogonal to the first two axes. Compute the vector cross product $\mathbf{e_{ttz}} \times \mathbf{e_{ttx}}$ to determine the medial-lateral direction, or y-axis, of the thigh technical coordinate system:

$$\mathbf{e_{tty}} = \mathbf{e_{ttz}} \times \mathbf{e_{ttx}} = -0.012\mathbf{i} + 0.943\mathbf{j} + 0.332\mathbf{k}$$

For this example, the technical coordinate system for the thigh can be expressed as

$$\{\mathbf{e_{tt}}\} = \begin{bmatrix} \mathbf{e_{ttx}} \\ \mathbf{e_{tty}} \\ \mathbf{e_{ttz}} \end{bmatrix} = \begin{bmatrix} 0.996 & 0.040 & 0.079 \\ -0.012 & 0.943 & 0.332 \\ -0.088 & 0.330 & 0.940 \end{bmatrix} \begin{bmatrix} \mathbf{i} \\ \mathbf{j} \\ \mathbf{k} \end{bmatrix}$$

Note that this thigh technical coordinate system $\{\mathbf{e_{tt}}\}$ computed during the standing subject calibration can also be computed from each camera frame of walking data. That is, its computation is based on markers (the lateral femoral condyle and thigh wand markers) and an anatomical landmark (the hip center) that are available for both the standing and walking trials. Consequently, the technical coordinate system $\{\mathbf{e_{tt}}\}$ becomes the embedded reference coordinate system to which other entities can be related. The thigh anatomical coordinate system $\{\mathbf{e_{ta}}\}$ can be related to the thigh technical coordinate system $\{\mathbf{e_{tt}}\}$ by using either direction cosines or Euler angles, as described in Section 4.2.2. Also, the location of markers that must be removed after the standing subject calibration (e.g., the medial femoral condyle marker MK), or computed anatomical locations (e.g., the knee center) can be transformed into the technical coordinate system $\{\mathbf{e_{tt}}\}$ and later retrieved for use in walking trial data reduction.

Segment and Joint Angles

Tracking the anatomical coordinate system for each segment allows for the determination of either the absolute angular orientation, or attitude, of each segment in space or the angular position of one segment relative to another. In the preceding example, the three pelvic angles that define the position of the pelvic anatomical coordinate system $\{\mathbf{e_{pa}}\}$ relative to the laboratory (inertially fixed) coordinate system can be computed from the Euler angles, as described in Section 4.2.2 with Eqs. (4.32)–(4.34). Note that in these equations the laboratory coordinate system represents the proximal (unprimed) coordinate system, and the pelvic anatomical coordinate system $\{\mathbf{e_{pa}}\}$ represents the distal (triple primed) coordinate system. Consequently, Eq. (4.32)

$$\theta_x = -\arcsin(\mathbf{k}''' \cdot \mathbf{j})$$

becomes

$$\begin{aligned} \theta_x &= -\arcsin(\mathbf{e_{paz}} \cdot \mathbf{j}) \\ &= -\arcsin((0.188\mathbf{i} - 0.024\mathbf{j} + 0.982\mathbf{k}) \cdot \mathbf{j}) \\ &= -\arcsin(-0.024) \\ &= 1° \text{of pelvic obliquity} \end{aligned}$$

Similarly, Eq. (4.33)

$$\theta_y = \arcsin\left(\frac{(\mathbf{k}''' \cdot \mathbf{i})}{\cos\theta_x}\right)$$

becomes

$$\theta_y = \arcsin\left(\frac{(\mathbf{e_{paz}} \cdot \mathbf{i})}{\cos\theta_x}\right)$$

$$= \arcsin\left(\frac{(0.188\mathbf{i} - 0.024\mathbf{j} + 0.982\mathbf{k}) \cdot \mathbf{i}}{\cos 1°}\right)$$

$$= \arcsin\left(\frac{0.188}{\cos 1°}\right)$$

$$= 11° \text{ of anterior pelvic tilt}$$

and Eq. (4.34)

$$\theta_z = \arcsin\left(\frac{(\mathbf{i}''' \cdot \mathbf{j})}{\cos\theta_x}\right)$$

becomes

$$\theta_z = \arcsin\left(\frac{(\mathbf{e_{pax}} \cdot \mathbf{j})}{\cos\theta_x}\right)$$

$$= \arcsin\left(\frac{(0.974\mathbf{i} - 0.123\mathbf{j} - 0.190\mathbf{k}) \cdot \mathbf{j}}{\cos 1°}\right)$$

$$= \arcsin\left(\frac{-0.123}{\cos 1°}\right)$$

$$= -7° \text{ of pelvic rotation}$$

This Euler angle computation may be repeated to solve for the three hip angles that define the position of the thigh anatomical coordinate system $\{\mathbf{e_{ta}}\}$ relative to the pelvic anatomical coordinate system $\{\mathbf{e_{pa}}\}$. For the hip angles, the proximal (unprimed) coordinate system is the pelvis and the distal (triple-primed) coordinate system is the thigh. Substituting the values of $\{\mathbf{e_{pa}}\}$ and $\{\mathbf{e_{ta}}\}$ from Example Problems 4.10 and 4.11 into Eq. (4.32) yields:

$$\theta_z = -\arcsin(\mathbf{e_{taz}} \cdot \mathbf{e_{pay}})$$

$$= -\arcsin((-0.137\mathbf{i} + 0.175\mathbf{j} + 0.975\mathbf{k}) \cdot (0.125\mathbf{i} + 0.992\mathbf{j} + 0.000\mathbf{k}))$$

$$= \arcsin(0.156)$$

$$= -9° \text{ of hip abduction-adduction}$$

The negative sign is associated with hip adduction of the left thigh or hip abduction of the right thigh.

Further substitution of values of $\{e_{pa}\}$ and $\{e_{ta}\}$ into Eqs. (4.33) and (4.34) yields

$$\text{hip flexion-extension } \theta_y = 20°$$
$$\text{hip internal-external rotation } \theta_z = -8°$$

For hip internal-external rotation, the negative sign is associated with hip internal rotation of the left thigh or hip external rotation of the right thigh. A negative hip flexion-extension angle corresponds to hip extension, independent of side. This process may be repeated for other body segments such as the shank (lower leg), foot, trunk, arms, and head with the availability of properly defined anatomical coordinate systems.

4.6.3 Kinetic Data Analysis

The marker displacement or motion data provide an opportunity to appreciate segment and joint kinematics. Kinematic data can be combined with ground reaction data—that is, forces and torques and their points of application, which are referred to as the centers of pressure. Combined with estimates of segment mass and mass moments of inertia, the net joint reaction forces and moments may then be computed.

To illustrate the details of this computational process, consider the following determination of the reactions at the ankle (Figure 4.30) for an individual with mass of 25.2 kg. Data for one instant in the gait cycle are shown in the following table.

	Symbol	Units	x_{lab}	y_{lab}	z_{lab}
Ankle center location	**A**	[m]	0.357	0.823	0.056
Toe marker location	**T**	[m]	0.421	0.819	0.051
Center of pressure location	**CP**	[m]	0.422	0.816	0.000
Ground reaction force vector	$\mathbf{F_g}$	[N]	3.94	−15.21	242.36
Ground reaction torque vector	$\mathbf{T_g}$	[N-m]	0.000	0.000	0.995
Foot anatomical coordinate system	$\mathbf{e_{fax}}$		0.977	−0.0624	−0.202
	$\mathbf{e_{fay}}$		0.0815	0.993	0.0877
	$\mathbf{e_{faz}}$		0.195	−0.102	0.975
Foot linear acceleration vector	$\mathbf{a_{foot}}$	[m/s^2]	2.09	−0.357	−0.266
Foot angular velocity vector	$\mathbf{\omega_{foot}}$	[rad/s]	0.0420	2.22	−0.585
Foot angular acceleration vector	$\mathbf{\alpha_{foot}}$	[rad/sec^2]	−0.937	8.85	−5.16
Ankle angular velocity vector	$\mathbf{\omega_{ankle}}$	[rad/s]	−0.000759	1.47	0.0106

Anthropomorphic relationships presented in Table 4.1 are used to estimate the mass and mass moments of inertia of the foot, as well as the location of its center of gravity. The mass of the foot, m_{foot}, may be estimated to be 1.45 percent of the body mass, or 0.365 kg, and the location of the center of gravity is approximated as 50 percent of the foot length. The length
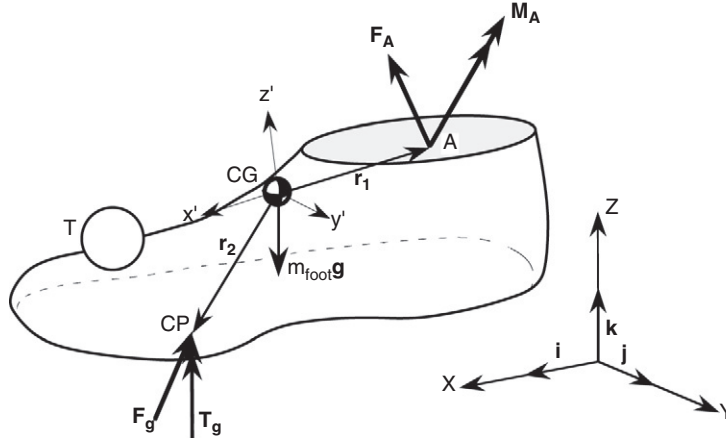
FIGURE 4.30 Ankle A and toe T marker data are combined with ground reaction force data $\mathbf{F_g}$ and segment mass and mass moment of inertia estimates to compute the net joint forces and moments.

of the foot ℓ_{foot} may be approximated as the distance between the ankle center and the toe marker, determined as follows:

$$\mathbf{T} - \mathbf{A} = (0.421 - 0.357)\mathbf{i} + (0.819 - 0.823)\mathbf{j} + (0.051 - 0.056)\mathbf{k}$$
$$= 0.064\mathbf{i} - 0.004\mathbf{j} - 0.005\mathbf{k}$$
$$\ell_{\text{foot}} = |\mathbf{T} - \mathbf{A}|$$
$$= \sqrt{(0.064)^2 + (-0.004)^2 + (-0.005)^2} = 0.064 \text{ m}$$

Then the location of the center of gravity can be determined relative to the ankle center as

$$\mathbf{A} + \frac{\ell_{\text{foot}}}{2}\frac{(\mathbf{T} - \mathbf{A})}{|\mathbf{T} - \mathbf{A}|} = (0.357\mathbf{i} + 0.823\mathbf{j} + 0.056\mathbf{k}) + \left[\frac{0.064}{2}\right]\left[\frac{0.064\mathbf{i} - 0.004\mathbf{j} - 0.005\mathbf{k}}{0.064}\right]$$

giving the location of the center of gravity:

$$\mathbf{CG} = 0.389\mathbf{i} + 0.821\mathbf{j} + 0.054\mathbf{k}$$

which allows computation of position vectors $\mathbf{r_1}$ and $\mathbf{r_2}$ (see Figure 4.30). With a foot length of 0.064 m, a foot mass of 0.365 kg, and a proximal radius of gyration per segment length of 0.690, the mass moment of inertia relative to the ankle center may be estimated with Eq. (4.40) as

$$I_{\text{foot/ankle}} = (0.365 \text{ kg})[(0.690)(0.064 \text{ m})]^2$$
$$= 7.12 \times 10^{-4}\text{kg m}^2$$

The centroidal mass moment of inertia, located at the foot's center of mass, may then be estimated using the parallel axis theorem (Eq. (4.41)):

$$I_{\text{foot/cm}} = I_{\text{foot/ankle}} - m_{\text{foot}}d^2$$

Note that the center of mass is equivalent to the center of gravity in a uniform gravitational field. In this case, d is the distance between the foot's center of mass and the ankle.

Table 4.1 shows the ratio of the foot center of mass location relative to its proximal end to be 0.5, so $d = 0.5(\ell_{\text{foot}}) = 0.032$ m. Therefore,

$$I_{\text{foot/cm}} = (7.12 \times 10^{-4} \text{ kg m}^2) - (0.365 \text{ kg})(0.032 \text{ m})^2$$
$$= 3.38 \times 10^{-4} \text{ kg m}^2$$

$I_{\text{foot/cm}}$ represents the centroidal mass moment of inertia about the transverse principal axes of the foot (y' and z' in Figure 4.30). Consequently,

$$I_{y'y'} = 3.38 \times 10^{-4} \text{ kg m}^2$$
$$I_{z'z'} = 3.38 \times 10^{-4} \text{ kg m}^2$$

The foot is approximated as a cylinder with a length to radius ratio of 6. The ratio of transverse to longitudinal (x') mass moments of inertia can be shown to be approximately 6.5. Then the longitudinal mass moment of inertia (about x' in Figure 4.30) may be estimated as

$$I_{x'x'} = 5.20 \times 10^{-5} \text{ kg m}^2$$

Having estimated the anthropomorphic values for the foot, the kinetic analysis may now begin. The unknown ankle reaction force, $\mathbf{F_A}$, is found by using Newton's Second Law, or $\sum \mathbf{F} = m\mathbf{a}$:

$$\mathbf{F_g} + \mathbf{F_A} - m_{\text{foot}} g\mathbf{k} = m_{\text{foot}} \mathbf{a_{foot}}$$
$$\mathbf{F_A} = m_{\text{foot}} \mathbf{a_{foot}} - \mathbf{F_g} + m_{\text{foot}} g\mathbf{k}$$
$$= (0.365 \text{ kg})[2.09\mathbf{i} - 0.357\mathbf{j} - 0.266\mathbf{k}] \text{ m/s}$$
$$- (3.94\mathbf{i} - 15.21\mathbf{j} + 242.4\mathbf{k}) \text{ N}$$
$$+ (0.365 \text{ kg})(9.81 \text{ m/s}^2)\mathbf{k}$$
$$= -3.18\mathbf{i} + 15.08\mathbf{j} - 238.9\mathbf{k} \text{ N}$$

Euler's equations of motion (Eqs. (4.44)–(4.46)) are then applied to determine the unknown ankle moment reaction $\mathbf{M_A}$. Euler's equations are defined relative to the principal axes fixed to the segment—that is, x', y', and z' fixed to the foot. It is noted, however, that the data required for the solution presented previously—for example, $\boldsymbol{\omega}_{\text{foot}}$ and $\boldsymbol{\alpha}_{\text{foot}}$—are expressed relative to the laboratory coordinate system (x, y, z). Consequently, vectors required for the solution of Euler's equations must first be transformed into the foot coordinate system. In the preceding data set, the foot anatomical coordinate system was given as

$$\mathbf{e_{fax}} = 0.977\mathbf{i} - 0.0624\mathbf{j} - 0.202\mathbf{k}$$
$$\mathbf{e_{fay}} = 0.0815\mathbf{i} + 0.993\mathbf{j} + 0.0877\mathbf{k}$$
$$\mathbf{e_{faz}} = 0.195\mathbf{i} - 0.102\mathbf{j} + 0.975\mathbf{k}$$

where $\mathbf{e_{fax}}$, $\mathbf{e_{fay}}$, and $\mathbf{e_{faz}}$ correspond to x', y', and z', or $\mathbf{i}'$, $\mathbf{j}'$, and $\mathbf{k}'$. Recall from the discussion in Section 4.2.2 that coefficients in the expression for $\mathbf{e_{fax}}$ represent the cosines of the angles between x' and x, x' and y, and x' and z, respectively. Similarly, the coefficients in the expression for $\mathbf{e_{fay}}$ represent the cosines of the angles between y' and x, y' and y, and y' and z, and

the coefficients in the expression for $\mathbf{e}_{faz}$ represent the cosines of the angles between z' and x, z' and y, and z' and z. Consequently, these relationships can be transposed as

$$\mathbf{i} = 0.977\mathbf{i}' + 0.0815\mathbf{j}' + 0.195\mathbf{k}'$$
$$\mathbf{j} = -0.0624\mathbf{i}' + 0.993\mathbf{j}' - 0.102\mathbf{k}'$$
$$\mathbf{k} = -0.202\mathbf{i}' + 0.0877\mathbf{j}' + 0.975\mathbf{k}'$$

In this form, these relationships can be used to transform vectors expressed in terms of lab coordinates:

$$\mathbf{A} = A_x\mathbf{i} + A_y\mathbf{j} + A_z\mathbf{k}$$

into foot coordinates:

$$\mathbf{A} = A_x\mathbf{i}' + A_y\mathbf{j}' + A_z\mathbf{k}'$$

To demonstrate this process, consider the foot angular velocity vector

$$\boldsymbol{\omega}_{foot} = 0.042\mathbf{i} + 2.22\mathbf{j} - 0.585\mathbf{k} \text{ rad/s}$$

Substituting the relationships for the lab coordinate system in terms of the foot coordinate system, $\boldsymbol{\omega}_{foot}$ becomes

$$\boldsymbol{\omega}_{foot} = 0.042(0.977\mathbf{i}' + 0.0815\mathbf{j}' + 0.195\mathbf{k}')$$
$$+ 2.22(-0.0624\mathbf{i}' + 0.993\mathbf{j}' - 0.102\mathbf{k}')$$
$$- 0.585(-0.202\mathbf{i}' + 0.0877\mathbf{j}' + 0.975\mathbf{k}')$$
$$= 0.0210\mathbf{i}' + 2.16\mathbf{j}' - 0.789\mathbf{k}' \text{ rad/s}$$

In a similar manner, the other vectors required for the computation are transformed into the foot coordinate system:

$$\mathbf{r}_1 = -0.032\mathbf{i} + 0.002\mathbf{j} + 0.002\mathbf{k}$$
$$= -0.032\mathbf{i}' - 0.004\mathbf{k}'\text{m}$$
$$\mathbf{r}_2 = 0.033\mathbf{i} - 0.005\mathbf{j} - 0.054\mathbf{k}$$
$$= 0.0435\mathbf{i}' - 0.007\mathbf{j}' - 0.0457\mathbf{k}' \text{ m}$$
$$\mathbf{F}_g = 3.94\mathbf{i} - 15.21\mathbf{j} + 242.36\mathbf{k}$$
$$= -44.16\mathbf{i}' + 6.47\mathbf{j}' + 238.62\mathbf{k}' \text{ N}$$
$$\mathbf{T}_g = 0.995\mathbf{k}$$
$$= -0.201\mathbf{i}' + 0.0873\mathbf{j}' + 0.970\mathbf{k}' \text{ N m}$$
$$\mathbf{F}_A = -3.18\mathbf{i} + 15.1\mathbf{j} - 239\mathbf{k}$$
$$= 44.2\mathbf{i}' - 6.23\mathbf{j}' - 235\mathbf{k}'\text{N}$$
$$\boldsymbol{\omega}_{foot} = 0.0420\mathbf{i} + 2.22\mathbf{j} - 0.585\mathbf{k}$$
$$= 0.021\mathbf{i}' + 2.16\mathbf{j}' - 0.789\mathbf{k}'\text{rad/s}$$
$$\boldsymbol{\alpha}_{foot} = -0.937\mathbf{i} + 8.85\mathbf{j} - 5.16\mathbf{k}$$
$$= -0.425\mathbf{i}' + 8.26\mathbf{j}' - 6.116\mathbf{k}'\text{rad/s}^2$$

Expanding Euler's equations of motion (Eqs. (4.44)–(4.46)),

$$\mathbf{M_{Ax'}} + (\mathbf{r}_1 \times \mathbf{F_A})_{x'} + (\mathbf{r}_2 \times \mathbf{F_g})_{x'} + \mathbf{T_{gx'}} = I_{x'x'}\alpha_{\mathbf{x'}} + (I_{z'z'} - I_{y'y'})\omega_{y'}\omega_{z'}$$
$$\mathbf{M_{Ay'}} + (\mathbf{r}_1 \times \mathbf{F_A})_{y'} + (\mathbf{r}_2 \times \mathbf{F_g})_{y'} + \mathbf{T_{gy'}} = I_{y'y'}\alpha_{\mathbf{y'}} + (I_{x'x'} - I_{z'z'})\omega_{z'}\omega_{x'}$$
$$\mathbf{M_{Az'}} + (\mathbf{r}_1 \times \mathbf{F_A})_{z'} + (\mathbf{r}_2 \times \mathbf{F_g})_{z'} + \mathbf{T_{gz'}} = I_{z'z'}\alpha_{\mathbf{z'}} + (I_{y'y'} - I_{x'x'})\omega_{x'}\omega_{y'}$$

where $(\mathbf{r}_1 \times \mathbf{F_A})_{x'}$ represents the $\mathbf{x'}$ component of $\mathbf{r}_1 \times \mathbf{F_A}$, $(\mathbf{r}_2 \times \mathbf{F_g})_{x'}$ represents the $\mathbf{x'}$ component of $\mathbf{r}_2 \times \mathbf{F_g}$, and so forth.

Substitution of the required values and arithmetic reduction yields

$$\mathbf{M_{A'}} = 1.50\mathbf{i'} + 15.9\mathbf{j'} - 1.16\mathbf{k'} \text{ N m}$$

which can be transformed back into fixed lab coordinates,

$$\mathbf{M_A} = 2.54\mathbf{i} + 15.9\mathbf{j} - 0.037\mathbf{k} \text{ N m}$$

By combining the ankle moment with the ankle angular velocity, the instantaneous ankle power may be computed as

$$\mathbf{M_A} \cdot \boldsymbol{\omega}_{\mathbf{ankle}} = (2.54\mathbf{i} + 15.9\mathbf{j} - 0.037\mathbf{k} \text{ N m}) \cdot (-0.000759\mathbf{i} + 1.47\mathbf{j} + 0.0106\mathbf{k} \text{ rad/s})$$
$$= 23.3 \text{ Watts}$$

or

$$\mathbf{M_{A'}} \cdot \boldsymbol{\omega}_{\mathbf{ankle'}} = (1.50\mathbf{i'} + 15.9\mathbf{j'} - 1.16\mathbf{k'} \text{ N m}) \cdot (-0.0946\mathbf{i'} + 1.46\mathbf{j'} - 0.140\mathbf{k'} \text{ rad/s})$$
$$= 23.3 \text{ Watts}$$

which is thought to represent a quantitative measure of the ankle's contribution to propulsion.

4.6.4 Clinical Gait Interpretation

The information and data provided for treatment decision making in clinical gait analysis include not only the quantitative variables described previously—3-D kinematics such as angular displacement of the torso, pelvis, hip, knee and ankle/foot, and 3-D kinetics, such as moments and power of the hip, knee, and ankle—but the following as well:

- Clinical examination measures
- Biplanar video recordings of the patient walking
- Stride and temporal gait data such as step length and walking speed
- Electromyographic (EMG) recordings of selected lower extremity muscles

Generally, the interpretation of gait data involves the identification of abnormalities, the determination of the causes of the apparent deviations, and the recommendation of treatment alternatives. As each additional piece of data is incorporated, a coherent picture of the patient's walking ability is developed by correlating corroborating data sets and resolving apparent contradictions in the information. Experience allows the team to distinguish a gait anomaly that presents the difficulty for the patient from a gait compensatory mechanism that aids the patient in circumventing the gait impediment to some degree.

To illustrate aspects of this process, consider the data presented in Figures 4.31–4.33, which were measured from a 9-year-old girl with cerebral palsy spastic diplegia. Cerebral
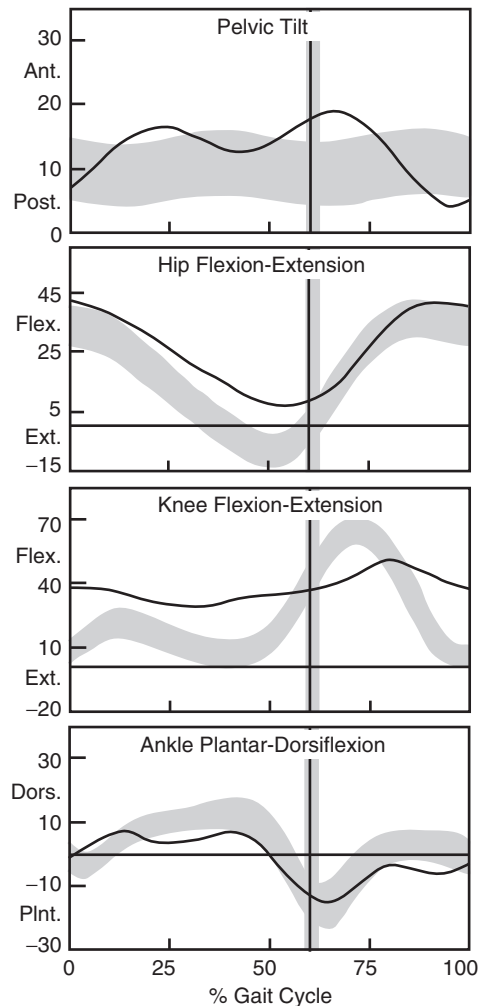
FIGURE 4.31 Sagittal plane kinematic data for the left side of a 9-year-old patient with cerebral palsy spastic diplegia (solid curves). Shaded bands indicate $+/-$ one standard deviation about the performance of children with normal ambulation. Stance phase is 0–60 percent of the gait cycle, and swing phase is 60–100 percent, as indicated by the vertical solid lines.

palsy is a nonprogressive neuromuscular disorder that is caused by an injury to the brain during or shortly after birth. The neural motor cortex is most often affected. In the ambulatory patient, this results in reduced control of the muscles required for balance and locomotion, causing overactivity, inappropriately timed activity, and muscle spasticity. Treatment options include physical therapy, bracing (orthoses), spasmolytic medications such as botulinum toxin and Baclofen, and orthopedic surgery and neurosurgery.

The sagittal plane kinematics for the left side of this patient (Figure 4.31) indicate significant involvement of the hip and knee. Her knee is effectively "locked" in an excessively
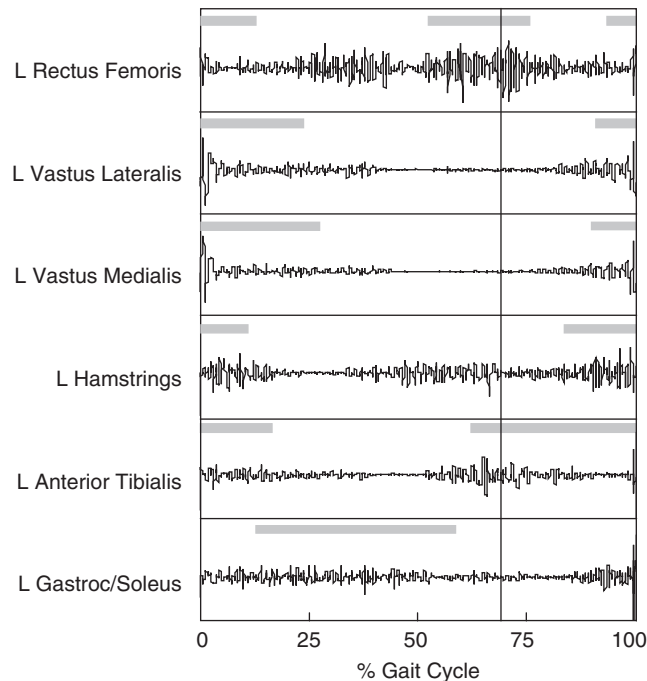
FIGURE 4.32 Electromyogram (EMG) data for the same cerebral palsy patient as in Figure 4.31. Plotted are EMG activity signals for each of six left lower extremity muscles, each plotted as functions of percent of gait cycle. Gray bars represent mean normal muscle activation timing.

flexed position throughout stance phase (0–60 percent of the gait cycle) when her foot is contacting the floor. Knee motion in swing phase (60–100 percent) is also limited, with the magnitude and timing of peak knee flexion in swing reduced and delayed. The range of motion of her hip during gait is less than normal, failing to reach full extension at the end of stance phase. The motion of her pelvis is significantly greater than normal, tilting anteriorly in early stance coincident with extension of the hip, and tilting posteriorly in swing coincident with flexion of the hip.

The deviations noted in these data illustrate neuromuscular problems commonly seen in this patient population. Inappropriate hamstring tightness, observed during the clinical examination, and inappropriate muscle activity during stance, seen in Figure 4.32, prevent the knee from properly extending. This flexed knee position also impedes normal extension of the hip in stance due to hip extensor weakness, also observed during the clinical examination. Hip extension is required in stance to allow the thigh to rotate under the advancing pelvis and upper body. To compensate for her reduced ability to extend the hip, she rotates her pelvis anteriorly in early stance to help move the thigh through its arc of motion. The biphasic pattern of the pelvic curve indicates that this is a bilateral issue to some degree.

The limited knee flexion in swing combines with the plantar flexed ankle position to result in foot clearance problems during swing phase. The inappropriate activity of the rectus femoris muscle (Figure 4.32) in midswing suggests that spasticity of that muscle, a
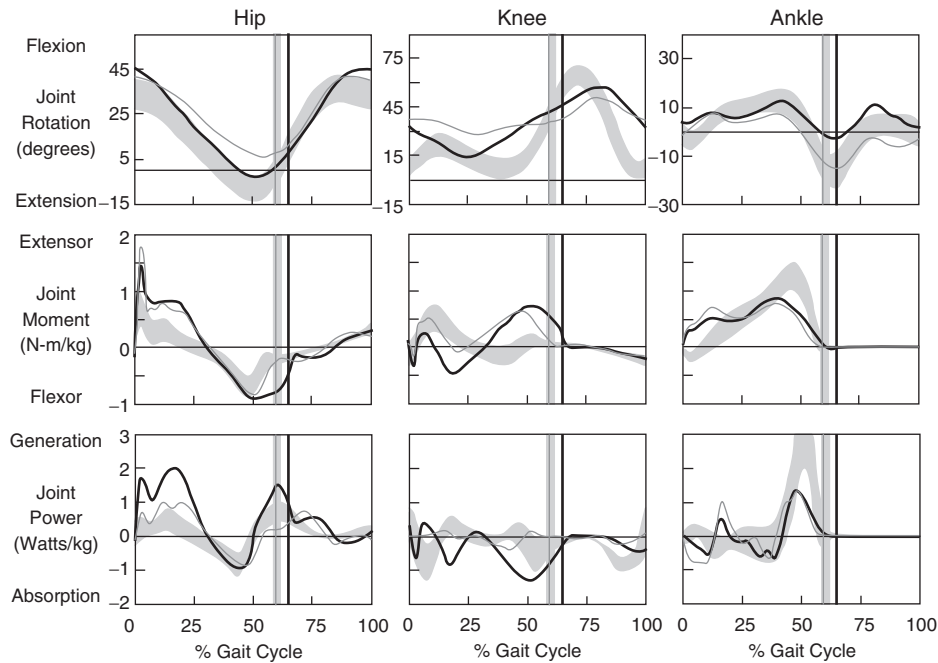
FIGURE 4.33 Sagittal joint kinetic data for the same cerebral palsy patient of Figure 4.31. Joint rotation, joint moment, and joint power are plotted as functions of percent of gait cycle for the hip, knee, and ankle. Dark and light solid curves denote right and left sides, respectively. Bands indicate $+/-$ one standard deviation of the normal population.

knee extensor (also observed during clinical examination), impedes knee flexion. Moreover, the inappropriate activity of the ankle plantar flexor, primarily the gastrocnemius muscle, in late swing suggests that it is overpowering the pretibial muscles, primarily the anterior tibialis muscle, resulting in plantar flexion of the ankle or "foot drop."

The sagittal joint kinetics for this patient (Figure 4.33) demonstrate asymmetrical involvement of the right and left sides. Of special note is that her right knee and hip are compensating for some of the dysfunction observed on the left side. Specifically, the progressively increasing right knee flexion beginning at midstance (first row, center) and continuing into swing aids her contralateral limb in forward advancement during swing—that is, her pelvis can rock posteriorly along with a flexing hip to advance the thigh. One potentially adverse consequence of this adaptation is the elevated knee extensor moment in late stance that increases patella-femoral loading with indeterminate effects over time. The asymmetrical power production at the hip also illustrates clearly that the right lower extremity, in particular the muscles that cross the hip, provides the propulsion for gait with significant power generation early in stance to pull the body forward and elevate its center of gravity. Moreover, the impressive hip power generation, both with respect to magnitude and timing, at toe-off accelerates the stance limb into swing and facilitates knee flexion in spite of the elevated knee extensor moment magnitude. This is important to appreciate given the bilateral spastic response of the plantar flexor muscles, as evidenced by the premature ankle power

generation and the presentation of a spastic stretch reflex in the clinical examination. This girl uses her hip musculature, right more than left, to a much greater degree than her ankle plantar flexors to propel herself forward during gait.

This cursory case examination illustrates the process whereby differences from normal gait are recognized and the associated biomechanical etiology is explored. Some of the effects on gait of neuromuscular pathology in the sagittal plane have been considered in this discussion. Clinical gait analysis can also document and elucidate gait abnormalities associated with static bony rotational deformities. It also is useful in areas of clinical research by documenting treatment efficacy associated with bracing, surgery, and so forth. It should be noted, however, that although engineers and applied physicists have been involved in this work for well over a hundred years, there remains significant opportunity for improvement in the biomechanical protocols and analytical tools used in clinical gait analysis; in other words, there remains much to learn.

4.7 CARDIOVASCULAR DYNAMICS

One major organ system benefiting from the application of mechanics principles is car-diovascular system dynamics, or *hemodynamics*, the study of the motion of blood. From a functional point of view, the cardiovascular system is driven by a complex pump, the heart, that generates pressure resulting in the flow of a complex fluid, blood, through a complex network of complex pipes, the blood vessels. Cardiovascular dynamics focuses on the measurement and analysis of blood pressure, volume, and flow within the cardiovascular system. The complexity of this elegant system is such that mechanical models, typically formulated as mathematical equations, are relied on to understand and integrate experi-mental data, to isolate and identify physiological mechanisms, and to lead ultimately to new clinical measures of heart performance and health and guide clinical therapies.

As described in Chapter 3, the heart is a four-chambered pump connected to two main col-lections of blood vessels: the systemic and pulmonary circulations. This pump is electrically triggered and under neural and hormonal control. One-way valves control blood flow. Total human blood volume is approximately 5.2 liters. The left ventricle, the strongest chamber, pumps 5 liters per minute at rest, almost the body's entire blood volume. With each heart-beat, the left ventricle pumps 70 ml, with an average of 72 beats per minute. During exercise, left ventricular output may increase sixfold, and heart rate more than doubles. The total com-bined length of the circulatory system vessels is estimated at 100,000 km, a distance two and one half times around the earth. The left ventricle generates approximately 1.7 watts of mechanical power at rest, increasing threefold during heavy exercise. One curious constant is the total number of heartbeats in a lifetime, around one billion in mammals [31]. Larger ani-mals have slower heart rates and live longer lives, and vice versa for small animals.

4.7.1 Blood Rheology

Blood is composed of fluid, called plasma, and suspended cells, including erythrocytes (red blood cells), leukocytes (white cells), and platelets. From a mechanical point of view, a fluid is distinguished from a solid as follows. Figure 4.34 shows a two-dimensional block of solid material (left panel) subjected to two opposite, parallel, transverse external forces, depicted by the solid arrows at the top and bottom surfaces. This applied shear force is resisted by
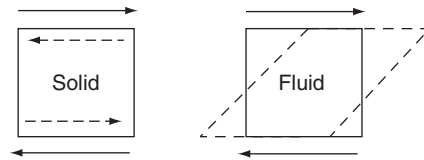
FIGURE 4.34 (Left) A solid material resists applied external shear stress (solid vectors) via internally generated reaction shear stress (dashed vectors). (Right) A fluid subjected to applied shear stress is unable to resist and instead flows (dashed lines).

the solid via internally generated reaction forces, depicted by the dashed arrows. When applied to a fluid (right panel), the fluid cannot resist the applied shear but rather flows.

The applied shear forces lead to shear stresses, force per area, and the measure of flow can be quantified by the resulting shear strain rate. In essence, the harder one pushes on a fluid (higher shear stress), the faster the fluid flows (higher shear strain rate). The relationship between shear stress, τ, and shear strain rate, $\dot{\gamma}$, is the fluid's viscosity, μ. Viscosity is sometimes written as η in biomedical applications. As shown in Figure 4.35, many fluids, including water, are characterized by a constant, linear viscosity and are called Newtonian. Others possess nonlinear shear stress-strain rate relations, and are non-Newtonian fluids. For example, fluids that behave more viscously as shear strain rate increases are called dilatant, or shear thickening. One example of dilatant behavior is Dow Corning 3179 dilatant compound, a silicone polymer commonly known as "Silly Putty." When pulled slowly, this fluid stretches (plastic deformation); when pulled quickly, it behaves as a solid and fractures. Fluids that appear less viscous with higher shear strain rates are called pseudoplastic, or shear thinning. For example, no-drip latex paint flows when applied with a brush or roller that provides shear stress, but it does not flow after application.
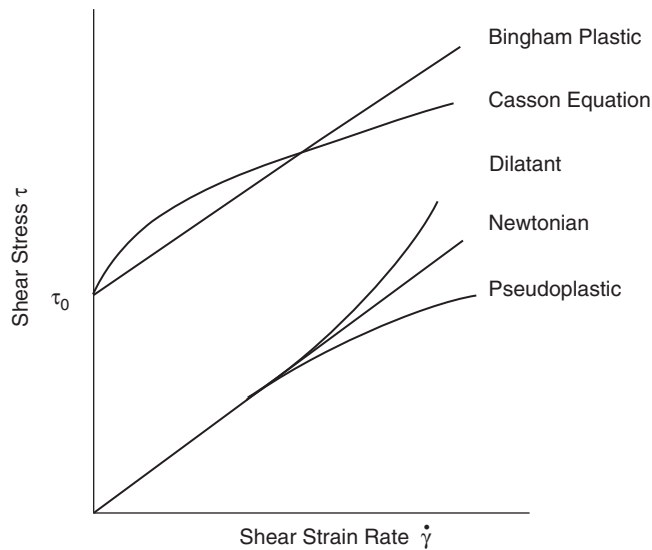

FIGURE 4.35 Newtonian fluids exhibit a constant viscosity $\mu = \tau/\dot{\gamma}$, arising from the linear relation between shear stress and shear strain rate. Non-Newtonian fluids are nonlinear. Blood is often characterized with a Casson equation but under many conditions may be described as Newtonian.

Biological fluids are typically non-Newtonian. Blood plasma is Newtonian and is very similar in physical properties to water. Whole blood behaves as a Bingham plastic, whereby a nonzero shear stress, denoted yield stress τ_0, is required before this fluid begins to flow. Blood is often characterized by a power law function, of the form

$$\tau = k\dot{\gamma}^n \tag{4.57}$$

where k and n are constants derived from a straight-line fit of $\ln \tau$ plotted as a function of $\ln \dot{\gamma}$, since

$$\ln \tau = \ln k + n \ln \dot{\gamma}$$

Another common description of blood's viscosity is the Casson equation:

$$\tau^{\frac{1}{2}} = \tau_0^{\frac{1}{2}} + k\dot{\gamma}^{\frac{1}{2}} \tag{4.58}$$

From a Casson plot, the yield stress τ_0 can be measured. Rheology, the study of deformation and flow of fluids, focuses on these often complex viscous properties of fluids. Textbooks with rheological data for biofluids include *Basic Transport Phenomena in Biomedical Engineering* by Fournier [9] and *Biofluid Mechanics* by Chandran and colleagues [4].

EXAMPLE PROBLEM 4.13

The following rheological data were measured on a blood sample:

Shear Strain Rate [s^{-1}]	Shear Stress [dyne/cm^2]
1.5	12.5
2.0	16.0
3.2	25.2
6.5	40.0
11.5	62.0
16.0	80.5
25.0	120
50.0	240
100	475

Fit the data to a power law function using a MATLAB m-file.

Solution

```
% Power Law Fit of Blood Data
%
% Store shear strain rate and stress data in arrays
alpha = [1.5,2,3.2,6.5,11.5,16,25,50,100];
T = [12.5,16,25.2,40,62,80.5,120,240,475];
% Take natural logs of both
x = log(alpha);
y = log(T);
```

```
% Use MATLAB's polyfit function to do linear curve fit
coeff = polyfit(x,y,1)
% Write curve fit coefficients as a new x-y function for plotting
x1=[0;0.01;5]
y1=polyval(coeff,x1)
% Plot the original data as 'o' points
plot(x,y,'o')
hold on
% Overlay a plot of the curve-fit line
plot(x1,y1)
grid on
title('Power Law Function')
xlabel('ln Strain Rate  [ln(1/s)]')
ylabel('ln Shear Stress  [ln dyne/cm2]')
%
```
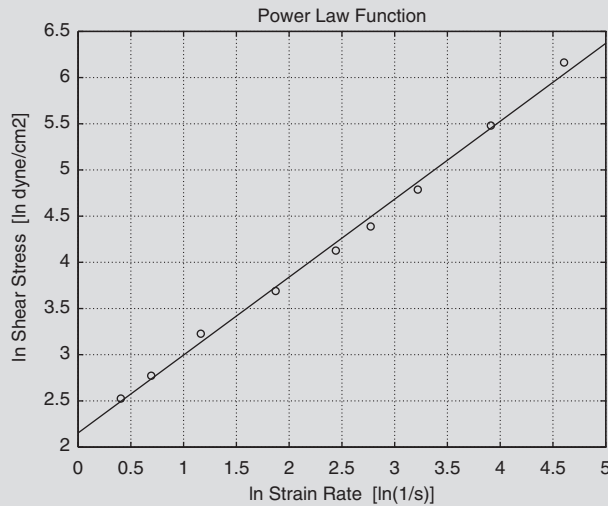
The resulting plot appears in Figure 4.36.

FIGURE 4.36 The power law curve-fit using MATLAB of the rheological blood data in Example Problem 4.13.

When subjected to very low shear rates, blood's apparent viscosity is higher than expected. This is due to the aggregation of red blood cells, called rouleaux. Such low shear rates are lower than those typically occurring in major blood vessels or in medical devices. In small tubes of less than 1 mm diameter, blood's apparent viscosity at high shear rates is smaller than in larger tubes. This Fahraeus-Lindquist effect arises from plasma–red blood cell dynamics. Beyond these two special cases, blood behaves as a Newtonian fluid and is widely accepted as such. We shall see that the assumption of Newtonian fluid greatly simplifies mechanical description of the circulation.

4.7.2 Arterial Vessels

Mechanical description of blood vessels has a long and somewhat complicated history. Much of the advanced mathematics and applied mechanics associated with this work is beyond the scope of this textbook. This section will therefore give an overview of some of the main developments and will present a simplified, reduced arterial system model for use in the following subsection. The reader is referred to the following textbooks for more in-depth coverage: *Circulatory System Dynamics* [21] by Noordergraaf, *Hemodynamics* [15] by Milnor, and *Biofluid Mechanics* [4] by Chandran and colleagues, and for basic fluid mechanics, *Fluid Mechanics* [30] by White.

Study of the mechanical properties of the heart as a pump requires the computation of pressures and flows arising from forces and motion of the underlying heart muscle. Consequently, general equations of motion in the cardiovascular system typically arise from the conservation of linear momentum. The Reynold's transport theorem, a conservation equation from fluid mechanics, applied to linear momentum yields the following general equation of motion for any fluid:

$$\rho \mathbf{g} - \nabla p + \nabla \cdot \boldsymbol{\tau}_{ij} = \rho \frac{d\mathbf{V}}{dt} \tag{4.59}$$

where ρ is fluid density (mass/volume), p is pressure, $\boldsymbol{\tau}_{ij}$ are viscous forces, and $\mathbf{V}$ is velocity. ∇ is the differential operator

$$\nabla = \mathbf{i} \frac{\partial}{\partial x} + \mathbf{j} \frac{\partial}{\partial y} + \mathbf{k} \frac{\partial}{\partial z}$$

The general velocity $\mathbf{V}$ is a vector function of position and time and is written

$$\mathbf{V}(x, y, z, t) = u(x, y, z, t)\mathbf{i} + v(x, y, z, t)\mathbf{j} + w(x, y, z, t)\mathbf{k}$$

where u, v, and w are the local velocities in the x, y, and z directions, respectively.

Equation (4.59) comprises four terms: *gravitational*, *pressure*, and *viscous forces*, plus a time-varying term. Note that this is a *vector* equation and so can be expanded in x, y, and z components as the set of three equations:

$$\rho g_x - \frac{\partial p}{\partial x} + \frac{\partial \tau_{xx}}{\partial x} + \frac{\partial \tau_{yx}}{\partial y} + \frac{\partial \tau_{zx}}{\partial z} = \rho \left(\frac{\partial u}{\partial t} + u \frac{\partial u}{\partial x} + v \frac{\partial u}{\partial y} + w \frac{\partial u}{\partial z} \right) \tag{4.60}$$

$$\rho g_y - \frac{\partial p}{\partial y} + \frac{\partial \tau_{xy}}{\partial x} + \frac{\partial \tau_{yy}}{\partial y} + \frac{\partial \tau_{zy}}{\partial z} = \rho \left(\frac{\partial v}{\partial t} + u \frac{\partial v}{\partial x} + v \frac{\partial v}{\partial y} + w \frac{\partial v}{\partial z} \right) \tag{4.61}$$

$$\rho g_z - \frac{\partial p}{\partial z} + \frac{\partial \tau_{xz}}{\partial x} + \frac{\partial \tau_{yz}}{\partial y} + \frac{\partial \tau_{zz}}{\partial z} = \rho \left(\frac{\partial w}{\partial t} + u \frac{\partial w}{\partial x} + v \frac{\partial w}{\partial y} + w \frac{\partial w}{\partial z} \right) \tag{4.62}$$

This set of nonlinear, partial differential equations is general but not solvable; solution requires making simplifying assumptions. For example, if the fluid's viscous forces are neglected, Eq. (4.59) reduces to Euler's equation for inviscid flow. The latter, when integrated along a streamline, yields the famous Bernoulli equation relating pressure and flow. In application, Bernoulli's inviscid, and consequently frictionless, origin is sometimes forgotten.

If flow is steady, the right-hand term of Eq. (4.59) goes to zero. For incompressible fluids, including liquids, density ρ is constant, which greatly simplifies integration of the

gravitational and time-varying terms that contain ρ. Similarly, for Newtonian fluids, viscosity μ is constant. In summary, although we can write perfectly general equations of motion, the difficulty of solving these equations requires making reasonable simplifying assumptions.

Two reasonable assumptions for blood flow in major vessels are those of Newtonian and incompressible behavior. These assumptions reduce Eq. (4.59) to the Navier-Stokes equations:

$$\rho g_x - \frac{\partial p}{\partial x} + \mu\left(\frac{\partial^2 u}{\partial x^2} + \frac{\partial^2 u}{\partial y^2} + \frac{\partial^2 u}{\partial z^2}\right) = \rho\frac{du}{dt} \tag{4.63}$$

$$\rho g_y - \frac{\partial p}{\partial y} + \mu\left(\frac{\partial^2 v}{\partial x^2} + \frac{\partial^2 v}{\partial y^2} + \frac{\partial^2 v}{\partial z^2}\right) = \rho\frac{dv}{dt} \tag{4.64}$$

$$\rho g_z - \frac{\partial p}{\partial z} + \mu\left(\frac{\partial^2 w}{\partial x^2} + \frac{\partial^2 w}{\partial y^2} + \frac{\partial^2 w}{\partial z^2}\right) = \rho\frac{dw}{dt} \tag{4.65}$$

Blood vessels are more easily described using a cylindrical coordinate system rather than a rectangular one. Hence, the coordinates x, y, and z may be transformed to radius r, angle θ, and longitudinal distance x. If we assume irrotational flow, $\theta = 0$ and two Navier-Stokes equations suffice:

$$-\frac{dP}{dx} = \rho\left(\frac{dw}{dt} + u\frac{dw}{dr} + w\frac{dw}{dx}\right) - \mu\left(\frac{d^2 w}{dr^2} + \frac{1}{r}\frac{dw}{dr} + \frac{d^2 w}{dx^2}\right) \tag{4.66}$$

$$-\frac{dP}{dr} = \rho\left(\frac{du}{dt} + u\frac{du}{dr} + w\frac{du}{dx}\right) - \mu\left(\frac{d^2 u}{dr^2} + \frac{1}{r}\frac{du}{dr} + \frac{d^2 u}{dx^2} - \frac{u}{r^2}\right) \tag{4.67}$$

where w is longitudinal velocity dx/dt, and u is radial velocity dr/dt. Most arterial models also use the continuity equation, arising from the conservation of mass:

$$\frac{du}{dr} + \frac{u}{r} + \frac{dw}{dx} = 0 \tag{4.68}$$

In essence, the net rate of mass storage in a system is equal to the net rate of mass influx minus the net rate of mass efflux.

Noordergraaf and his colleagues [20] rewrote the Navier-Stokes Eq. (4.66) as

$$-\frac{dP}{dx} = RQ + L\frac{dQ}{dt} \tag{4.69}$$

where P is pressure, Q is the volume rate of flow, R is an equivalent hydraulic resistance, and L is fluid inertance. The Navier-Stokes equations describe fluid mechanics within the blood vessels. Since arterial walls are elastic, equations of motion for the arterial wall are also required. The latter have evolved from linear elastic and linear viscoelastic, to complex viscoelastic (see [21]). The most general mechanical description of linear anisotropic arterial wall material requires 21 parameters (see [10]), most of which have never been measured. Noordergraaf and colleagues divided the arterial system into short segments and combined the fluid mechanical equation (Eq. (4.69)) with the continuity equation for each vessel segment. The arterial wall elasticity leads to a time-varying amount of blood stored in the

vessel as it bulges with each heartbeat. For a segment of artery, the continuity equation becomes

$$-\frac{dQ}{dx} = GP + C\frac{dP}{dt} \tag{4.70}$$

where G is leakage through the blood vessel wall. This pair of hydraulic equations— Eqs. (4.69) and (4.70)—was used to describe each of 125 segments of the arterial system and was the first model sufficiently detailed to explain arterial pressure and flow wave reflection. Arterial branching leads to reflected pressure and flow waves that interact in this pulsatile system. Physical R-L-C circuits were constructed and built into large transmission line networks with measured voltages and currents corresponding to hydraulic pressures and flows, respectively. If distributed arterial properties such as pulse wave reflection are not of interest, the arterial system load seen by the heart can be much reduced, as an electrical network may be reduced to an equivalent circuit.

The most widely used arterial load is the three-element model shown in Figure 4.37. The model appears as an electrical circuit due to its origin prior to the advent of the digital computer. Z_0 is the characteristic impedance of the aorta, in essence the aorta's flow resistance. C_s is transverse arterial compliance, the inverse of elastance, and describes stretch of the arterial system in the radial direction. R_s is the peripheral resistance, describing the systemic arteries' flow resistance downstream of the aorta. This simple network may be used to represent the systemic arterial load seen by the left ventricle. The following ordinary differential equation relates pressure at the left-hand side, $p(t)$, to flow, $Q(t)$:

$$C_s\frac{dp}{dt} + \frac{1}{R_s}p(t) = Q(t)\left(1 + \frac{Z_0}{R_s}\right) + Z_0C_s\frac{dQ}{dt} \tag{4.71}$$
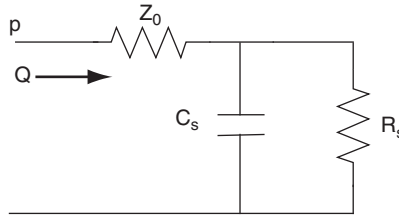

FIGURE 4.37   Equivalent systemic arterial load. Circuit elements are described in the text.

EXAMPLE PROBLEM 4.14

Using basic circuit theory, derive the differential equation (Eq. (4.71)) from Figure 4.37.

Solution

Define node 1 as shown in Figure 4.38. By Kirchoff's current law, the flow Q going into node 1 is equal to the sum of the flows Q_1 and Q_2 coming out of the node:

$$Q = Q_1 + Q_2$$

We can write Q_1 and Q_2 as
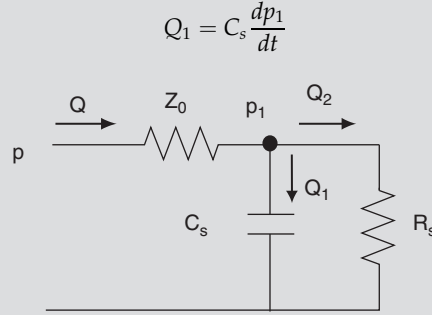
$$Q_1 = C_s \frac{dp_1}{dt}$$

FIGURE 4.38   Nodal analysis of three-element arterial load.

$$Q_2 = \frac{p_1}{R_s}$$

so

$$Q = C_s \frac{dp_1}{dt} + \frac{p_1}{R_s}$$

From Ohm's law,

$$p - p_1 = QZ_0$$

Solving the last expression for p_1 and substituting back into the flow expression:

$$Q = C_s \frac{d}{dt}[p - QZ_0] + \frac{1}{R_s}[p - QZ_0]$$

$$= C_s \frac{dp}{dt} - Z_0 C_s \frac{dQ}{dt} + \frac{1}{R_s}p - \frac{Z_0}{R_s}Q$$

Grouping terms for Q on the left and p on the right gives

4.7.3 Heart Mechanics

Mechanical performance of the heart, more specifically the left ventricle, is typically characterized by estimates of ventricular elastance. The heart is an elastic bag that stiffens and relaxes with each heartbeat. Elastance is a measure of stiffness, classically defined as the differential relation between pressure and volume:

$$E_v = \frac{dp_v}{dV_v} \tag{4.72}$$

Here, p_v and V_v denote ventricular pressure and volume, respectively. For any instant in time, ventricular elastance E_v is the differential change in pressure with respect to volume. Mathematically, this relation is clear. Measurement of E_v is much less clear.

In the 1970s Kennish and colleagues tried to estimate the differential relation of Eq. (4.72) using the ratio of finite changes in ventricular pressure and volume:

$$E_v = \frac{\Delta p_v}{\Delta V_v} \tag{4.73}$$

This approach leads to physically impossible results. For example, before the aortic valve opens, the left ventricle is generating increasing pressure while there is not yet any change in volume. The ratio in Eq. (4.73) gives an infinite elastance when the denominator is zero. Suga and Sagawa [28] used the ratio of pressure to volume itself, rather than differential or discrete changes, to estimate elastance:

$$E_v(t) = \frac{p_v(t)}{V_v(t) - V_d} \tag{4.74}$$

In this equation, V_d is a dead volume that remains constant. All the other terms are allowed to be varying with time. Ventricular elastance measured in this way leads to elastance curves as depicted in Figure 4.39. These curves show wide variation, as suggested by the large error bars. The distinctive asymmetric shape leads to a major contradiction. A simple experiment involves clamping the aorta, thereby preventing the left ventricle from ejecting blood, denoted an *isovolumic* beat. Equation (4.74) shows that under isovolumic conditions (V_v is constant) ventricular pressure p_v must have the same shape as elastance $E_v(t)$. However, experiments show that isovolumic pressure curves are symmetric, unlike Figure 4.39. A further complication is the requirement of ejecting beats for measuring $E_v(t)$, which requires not only the heart (a ventricle) but also a circulation (blood vessels). Hence, time-varying elastance curves such as Figure 4.39 are measures of both a particular heart, the source, combined with a particular circulation, its load. Experiments show that elastance curves measured in this way are subject to vascular changes, as well as the desired ventricular properties. As such, this approach cannot uniquely separate out ventricular from vascular properties. Consequently, a new measure of the heart's mechanical properties is required.

The problems just described—inconsistent isovolumic and ejecting behavior and combined heart-blood vessel properties—led to the development of a new mechanical description of the
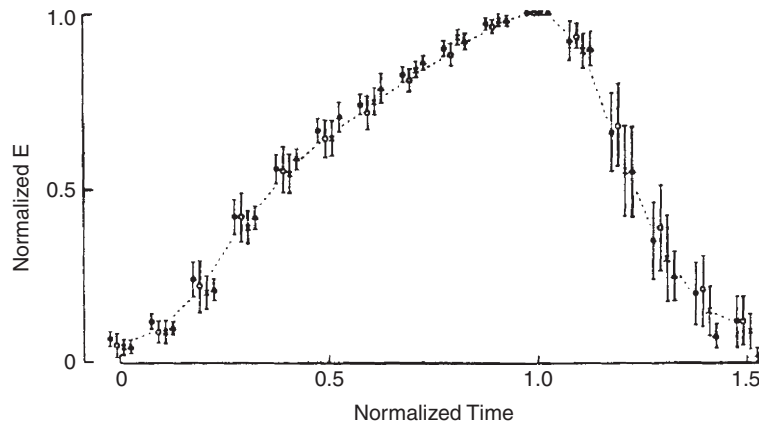

FIGURE 4.39   Time-varying ventricular elastance curves measured using the definition in Eq. (4.74). Measured elastance curves exhibit distinctive asymmetry. *Adapted from [28].*
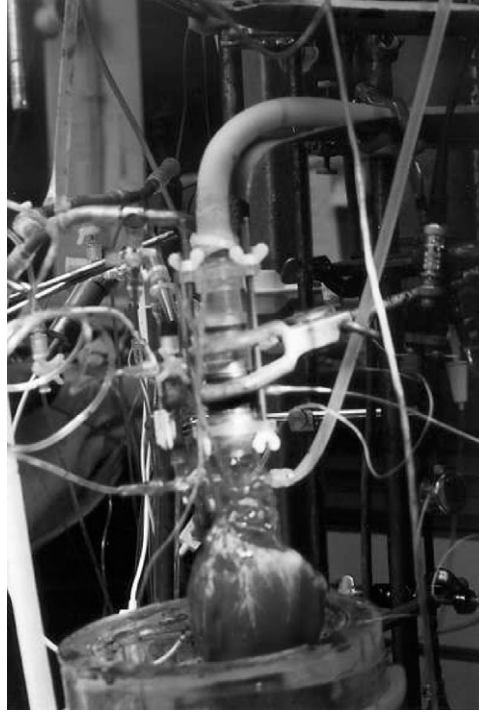
FIGURE 4.40 Isolated canine left ventricle used to develop a new biomechanical model of the heart. *Photo courtesy of Dr. Jan Mulier, Leuven, Belgium.*

left ventricle [17, 24, 23]. This model should be simple and versatile and should have direct physiological significance, in contrast with simulations, which merely mimic physiological behavior. The model was developed using isolated canine heart experiments, as depicted in Figure 4.40. The left ventricle was filled with an initial volume of blood, subjected to different loading conditions, stimulated, and allowed to beat. Ventricular pressure, and in some experiments ventricular outflow, was then measured and recorded.

Experiments began with measurement of isovolumic ventricular pressure. For each experiment the isolated left ventricle was filled with an initial end-diastolic volume and the aorta was clamped to prevent outflow of blood. The ventricle was stimulated, and generated ventricular pressure was measured and recorded. The ventricle was then filled to a new end-diastolic volume and the experiment was repeated. As in the famous experiments of Otto Frank (c. 1895), isovolumic pressure is directly related to filling. Figure 4.41 shows a set of isovolumic pressure curves measured on a normal canine left ventricle.

These isovolumic pressure curves were then described by the following equation. Ventricular pressure p_v is a function of time t and ventricular volume V_v according to

$$p_v = a(V_v - b)^2 + (cV_v - d)\left[\frac{(1 - e^{-(\frac{t}{\tau_c})^\alpha})e^{-(\frac{t-t_b}{\tau_r})^\alpha}}{(1 - e^{-(\frac{t_p}{\tau_c})^\alpha})e^{-(\frac{t_p-t_b}{\tau_r})^\alpha}}\right] \tag{4.75}$$

or written more compactly,

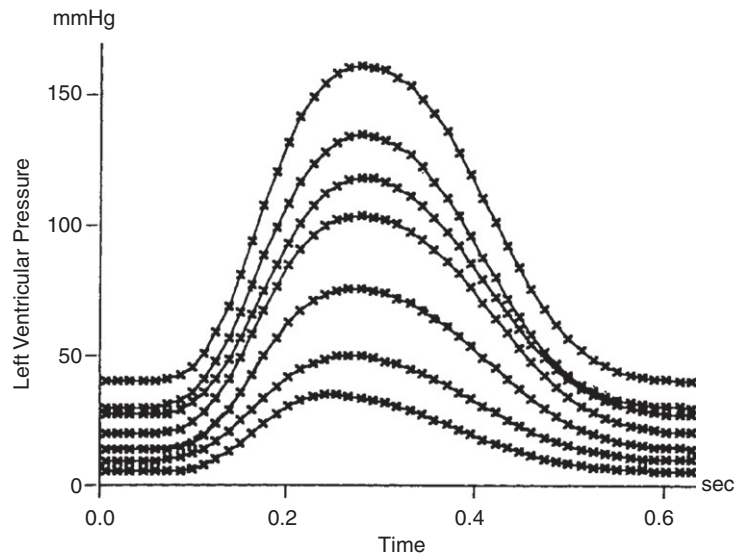$$p_v(t, V_v) = a(V_v - b)^2 + (cV_v - d)f(t) \tag{4.76}$$

FIGURE 4.41	Isovolumic ventricular pressure curves. For each curve, the left ventricle is filled with a fixed initial volume, the heart is stimulated, and generated ventricular pressure is measured with respect to time. Other curves arise from different fixed initial volumes.

where $f(t)$ is the activation function in square brackets in Eq. (4.75). The constants a, b, c, d, t_p, τ_c, τ_r, and α were derived from the isolated canine ventricle experiments. Physiologically, Eq. (4.76) says that the ventricle is a time- and volume-dependent pressure generator. The term to the left of the plus sign, including constants a and b, describes the ventricle's passive elastic properties. The term to the right, including c and d, describes its active elastic properties, arising from the active generation of force in the underlying heart muscle. Representative model quantities measured from canine experiments are given in Table 4.3. This model was adapted to describe the human left ventricle using quantities in the right-hand column [24, 25].

TABLE 4.3	Ventricle Model Quantities Measured from Animal Experiments and Adapted for the Human Analytical Model

Quantity	Dog (Measured)	Human (Adapted)
a	0.003 [mmHg/ml^2]	0.0007
b	1.0 [ml]	20.0
c	3.0 [mmHg/ml]	2.5
d	20.0 [mmHg]	80.0
τ_c	0.164 [s]	0.264
t_P	0.271 [s]	0.371
τ_r	0.199 [s]	0.299
t_b	0.233 [s]	0.258
α	2.88	2.88

EXAMPLE PROBLEM 4.15

Solve Eq. (4.75) and plot ventricular pressure $p_v(t)$ for one human heartbeat. Use initial ventricular volume of 150 ml and the parameter values in Table 4.3.

Solution

The following MATLAB m-file will perform the required computation and plot the results, shown in Figure 4.42.
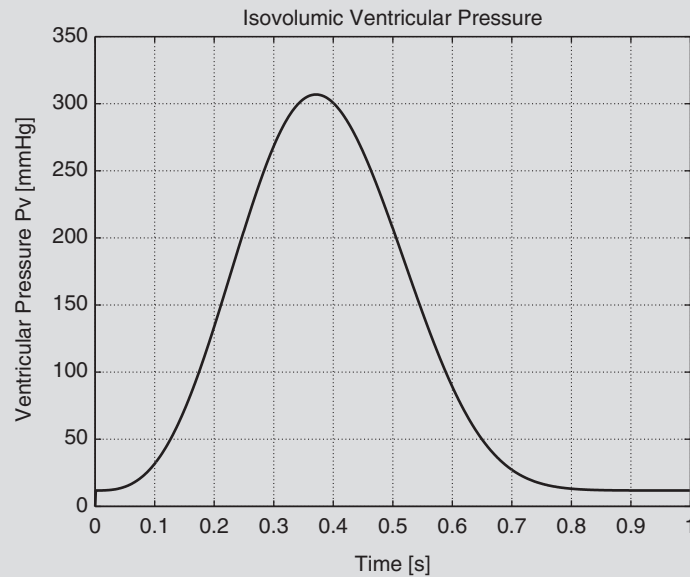

FIGURE 4.42   Isovolumic ventricular pressure computed for a human heartbeat.

```
% ventricle.m
%
% MATLAB m-file to compute isovolumic pressure using ventricle model
%
% Initial conditions:
%
delt = 0.001; % The iteration time step delta t
a = 7e-4;
b = 20.;
c = 2.5;
d = 80.;
tc = 0.264;
tp = 0.371;
tr = 0.299;
tb = 0.258;
alpha = 2.88;
```

Continued

```matlab
Vv0 = 150; % Initial (end-diastolic) ventricular volume
%
% Compute intermediate term denom
% to simplify computations:
%
   denom = ((1.-exp(-(tp/tc)^alpha))*exp(-((tp-tb)/tr)^alpha));
%
% Compute for initial time t=0 (MATLAB does not allow 0 index)
%
   t(1) = 0.;
   Vv(1) = Vv0;
   edp = a*((Vv0 -b))^2;
   pdp = c*Vv0 - d;
   pp = pdp/denom;
   t1 = 0.; % Time step for first exponential
   t2 = 0.; % Time step for second exponential
   e1 = exp(-(t1/tc)^alpha);
   e2 = exp(-(t2/tr)^alpha);
   pv0 = edp + pp*((1.-e1)*e2);
%
% Main computation loop:
%
   for j=2:1000
   t(j) = t(j-1) + delt;
   Vv(j) = Vv(j-1);
%
   edp = a*((Vv(j) -b))^2;
   pdp = c*Vv(j) - d;
   pp = pdp/denom;
   t1 = t(j);
% Second exponential begins at t > tb
   t2 = t(j) - tb;
   if (t2 < 0.) ;
   t2 = 0.;
   end
   e1 = exp(-(t1/tc)^alpha);
   e2 = exp(-(t2/tr)^alpha);
   pv(j) = edp + pp*((1.-e1)*e2);
   end
%
plot(t,pv)
grid on
title('Isovolumic Ventricular Pressure')
xlabel('Time [s]')
ylabel('Ventricular Pressure Pv [mmHg]')
```

4.7.4 Cardiovascular Mechanics

This concise generalized pressure model of the left ventricle (Eq. (4.75)) was coupled to the reduced arterial load model of Figure 4.37 and allowed to eject blood. Model parameter values for a normal arterial load are given in Table 4.4. Figure 4.43 shows results for a normal canine left ventricle ejecting into a normal arterial system. The solid curves (left ordinate) describe ventricular pressure p_v and root aortic pressure as functions of time. Clinically, arterial pressure is reported as two numbers—for example, 110/60. This corresponds to the maximum and minimum root arterial pulse pressures—in this case, about 120/65 mmHg. The dashed curve (right ordinate) shows ventricular outflow. The ventricle was filled with an end-diastolic volume of 45 ml, and it ejected 30 ml (stroke volume), giving an ejection fraction of 66 percent, which is about normal for this size animal.

The same ventricle may be coupled to a pathological arterial system—for example, one with doubled peripheral resistance R_s. This change is equivalent to narrowed blood vessels.

TABLE 4.4 Representative Systemic Arterial Model Element Values

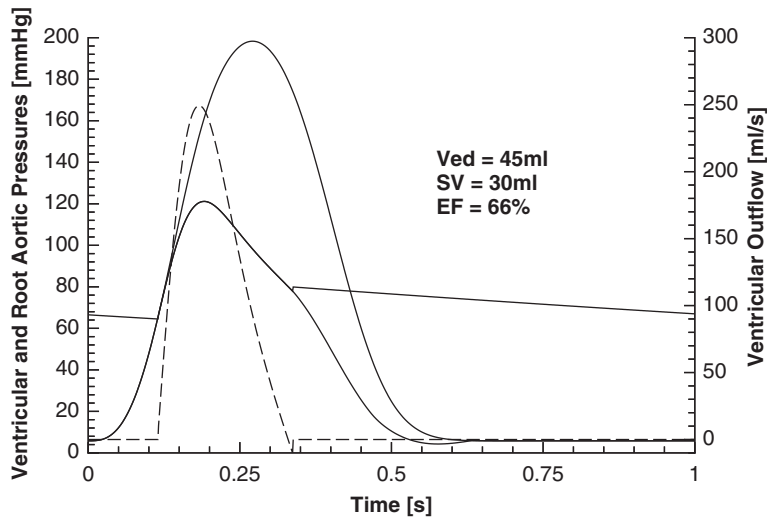| Element	Symbol	Control Value
Characteristic aorta impedance	Z_0	0.1 mmHg-s/ml
Systemic arterial compliance	C_s	1.5 ml/mmHg
Peripheral arterial resistance	R_s	1.0 mmHg-s/ml

FIGURE 4.43   Ventricular and root aortic pressures (solid curves, left ordinate) and ventricular outflow (dashed curve, right ordinate) computed using the model of Eq. (4.75) for a normal canine left ventricle pumping into a normal arterial circulation. The topmost solid curve corresponds to a clamped aorta (isovolumic). The ventricle has initial volume of 45 ml and pumps out 30 ml, for an ejection fraction of 66 percent, which is about normal.
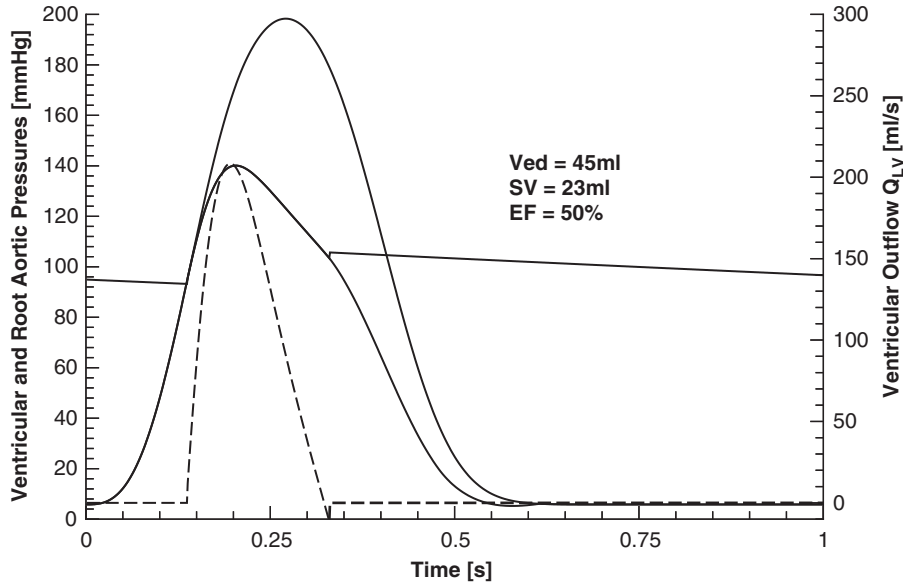
FIGURE 4.44 The same normal canine ventricle of Figure 4.43 now pumping into an arterial system with doubled peripheral (flow) resistance. As expected, increased resistance, corresponding to narrowed vessels, leads to increased arterial pulse pressure. Stroke volume is reduced from 66 to to 50 percent.

As expected, increased peripheral resistance raises arterial blood pressure to 140/95 mmHg and impedes the ventricle's ability to eject blood (Figure 4.44). The ejection fraction decreases to 50 percent in this experiment. Other experiments, such as altered arterial stiffness, may be performed. The model's flexibility allows description of heart pathology as well as changes in blood vessels. This one ventricular equation with one set of measured parameters is able to describe the wide range of hemodynamics observed experimentally [24, 23].

The previous expressions for ventricular elastance defined in Eqs. (4.73) and (4.74) have the same units as elastance defined classically as Eq. (4.72), but are mathematically not the same. Since ventricular pressure is defined as an analytical function (Eq. (4.75)), ventricular elastance, E_v, defined in the classical sense, may now be calculated as $\partial p_v / \partial V_v$:

$$E_v(t, V_v) = 2a(V_v - b) + c \left[\frac{(1 - e^{-(\frac{t}{\tau_c})^\alpha}) e^{-(\frac{t-t_b}{\tau_r})^\alpha}}{(1 - e^{-(\frac{t_p}{\tau_c})^\alpha}) e^{-(\frac{t_p-t_b}{\tau_r})^\alpha}} \right] \quad (4.77)$$

or

$$E_v(t, V_v) = 2a(V_v - b) + cf(t) \quad (4.78)$$

Figure 4.45 shows ventricular elastance curves computed using this new analytical definition of elastance (Eq. (4.77)). Elastance was computed for a wide range of ventricular and arterial states, including normal and pathological ventricles, normal and pathological arterial systems, and isovolumic and ejecting beats. These elastance curves are relatively
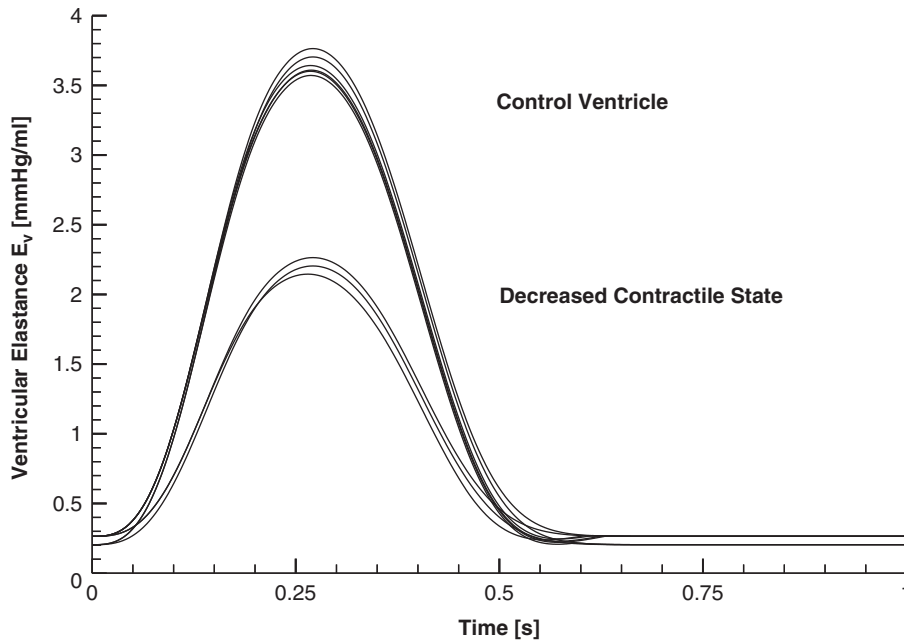
FIGURE 4.45 Ventricular elastance curves computed using the new analytical function of Eq. (4.77). Elastance curves computed in this way are representative of the ventricle's contractile state—that is, its ability to pump blood.

invariant and cluster in two groups: either normal or weakened ventricle contractile state. Consequently, this new measure of elastance may now effectively assess the health of the heart alone, separate from blood vessel pathology.

Chapter 3 gives a brief overview of the circulatory system, a mass and heat transfer system that circulates blood throughout the body. Figure 3.18 shows the four chambers of the heart, the major blood vessels, and valves between the two. From a mechanical point of view, the contracting heart chambers generate pressures that propel blood into the downstream blood vessels. This process is depicted in detail for the most important chamber, the left ventricle, in Figure 4.46. Plotted are representative waveforms for an isolated canine left ventricle, with ventricular pressure and root aortic pressure (top), ventricular volume (middle) and ventricular outflow (bottom), all as functions of time. The numbers 1–4 at the top of the figure correspond to four major phases of the contraction cycle, marked by dashed lines. At time 1, filling is complete, the mitral valve closes, and the ventricle begins to contract isovolumically (no change in volume). At time 2, ventricular pressure exceeds root aortic pressure, the aortic valve opens, and blood ejection begins. Heart valves are passive, and the outflow of blood results simply from the pressure difference across the valve. When ventricular pressure falls below aortic pressure, the aortic valve closes (time 3) and outflow ends. The initial volume (time 1) is denoted end-diastolic volume, EDV, and the volume at the end of ventricular ejection (time 3) is end-systolic volume, ESV. At time 4, ventricular pressure falls below left atrial pressure (not shown), the mitral valve opens, and filling begins in preparation for the next heartbeat. The difference between
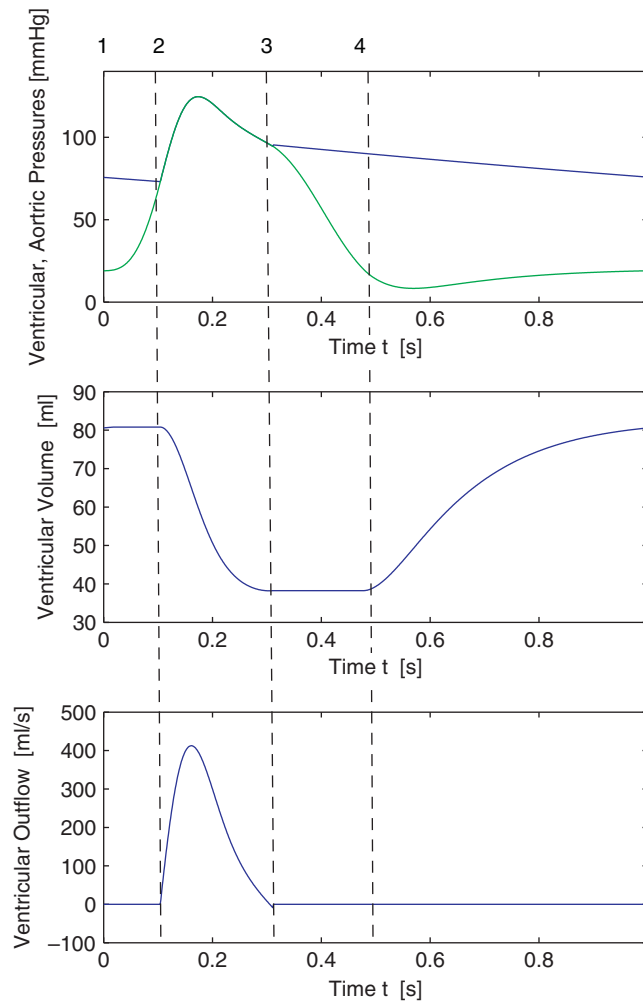
FIGURE 4.46 Representative left ventricular and root aortic pressures (top), ventricular volume (middle), and ventricular outflow (bottom) for an isolated canine heart. The numbers 1–4 at top correspond to distinct phases of the cardiac cycle, described in the text.

end-diastolic and end-systolic volumes, EDV-ESV, is denoted stroke volume, SV, and is the amount of blood pumped in one heartbeat. The ratio SV/EDV is the ejection fraction, EF, and is approximately 50 percent in this example. Clinical blood pressure corresponds to the maximum and minimum arterial pressures—in this example, around 125/75 mmHg.

Clinicians often study heart performance via pressure-volume work loops, plotting ventricular pressure as a function of ventricular volume, as in Figure 4.47. The four phases of the heart cycle just described are plotted for the same heart as in Figure 4.46, with isovolumic contraction between points 1 and 2, ejection from 2 to 3, isovolumic relaxation between 3 and 4, and
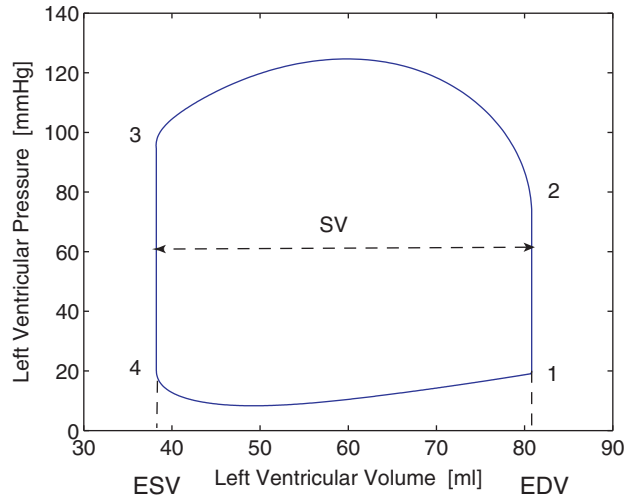
FIGURE 4.47   Pressure-volume work loop corresponding to the left ventricular data in Figure 4.46.

refilling from 4 to 1. Also shown are volumes EDV, ESV, and SV. The area bounded by the work loop corresponds to mechanical work performed by the left ventricle.

Figure 4.48 shows work loops calculated from the generalized pressure model of the left ventricle (Eq. (4.75)) pumping into the three-element arterial load model (Figure 4.37) using human parameter values for both the ventricle and arterial load. The left ventricle was filled from a constant pressure reservoir. The control work loop (center) may be compared to those corresponding to a 10 percent increase and 10 percent decrease in filling pressure.
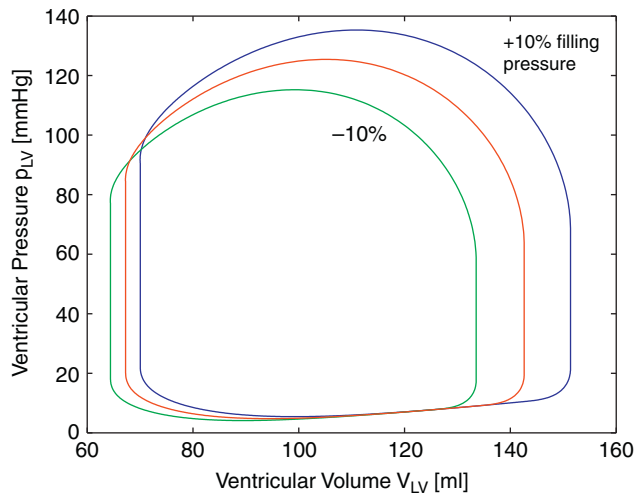

FIGURE 4.48   Pressure-volume work loops computed for the human left ventricle (Eq. (4.75)) and arterial load (Figure 4.37) for control (middle curve) and varied preload (filling) conditions.

These changes directly affect the amount of filling of the ventricle, denoted *preload*. Stroke volume increases with increased preload, and vice versa. As the ventricle is filled more, the end-diastolic volume shifts to the right and the work loop area increases due to the Frank-Starling mechanism. In essence, increased filling stretches the constituent heart muscle, which allows the muscle to generate more force via the force-length relation, the direct relation between muscle length and maximum force of contraction (up to a point). There is also a small shift of end-systolic volume to the right with increased preload. As the heart ejects more blood (SV), the load against which the heart must work is increased.

Figure 4.49 shows work loops for the same ventricle and arterial load for direct variations in *afterload*, the load against which the ventricle pumps. Afterload changes were achieved by varying the value of arterial peripheral resistance R_S. Stroke volume decreases as afterload is increased due to the underlying force-velocity relation of muscle. Higher peripheral resistance forces muscle to operate at a lower velocity of shortening, so less time is available for the ventricle to eject blood. Figure 4.49 shows a small shift of end-diastolic volume to the right with increased afterload. Since stroke volume is reduced, there is remaining blood available for the next heartbeat. This effect is more pronounced in the natural system, which can be examined by extending the model as follows.

The left ventricle model of Eq. (4.75) was used to describe each of the four chambers of the human heart, depicted in Figure 4.50 [25, 23]. This complete model of the circulatory system displays a remarkable range of cardiovascular physiology with a small set of equations and parameters. Changes in blood vessel properties may be studied alone or in combination with altered heart properties. Other system parameters such as atrial performance, as well as other experiments, may be examined. The modular form of this model allows its expansion for more detailed studies of particular sites in the circulatory system.

Figure 4.51 shows work loops computed for the left ventricle in the complete circulatory system model for three different preloads, achieved by increasing and decreasing total
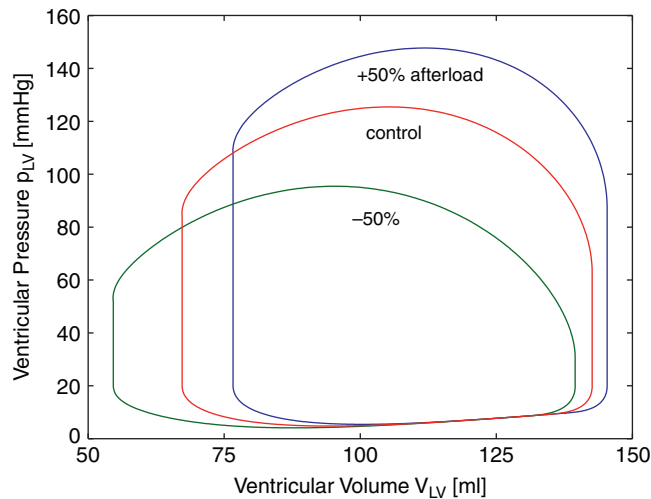

FIGURE 4.49   Pressure-volume work loops computed for the human left ventricle (Eq. (4.75)) and arterial load (Figure 4.37) for control and varied afterload, achieved by varying peripheral resistance R_S.
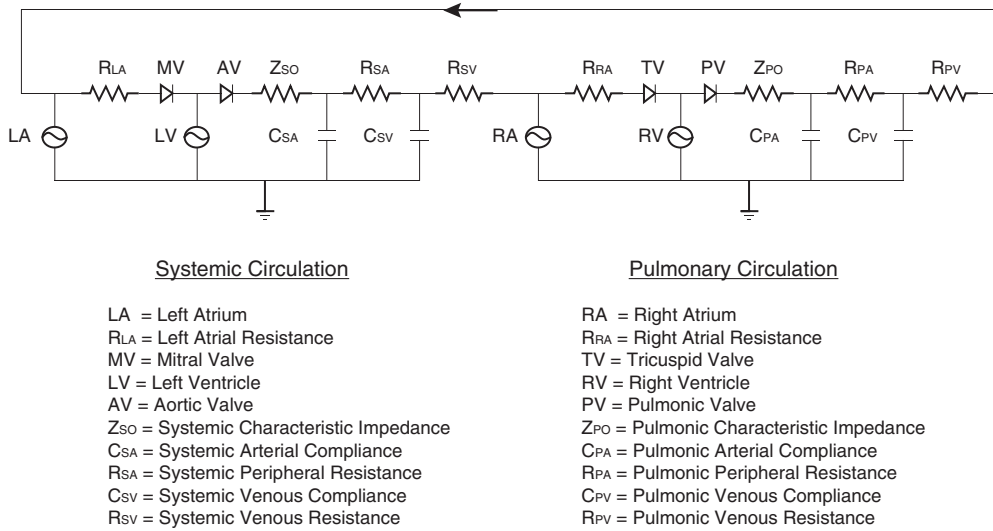
Systemic Circulation   Pulmonary Circulation

LA = Left Atrium   RA = Right Atrium
R_{LA} = Left Atrial Resistance R_{RA} = Right Atrial Resistance
MV = Mitral Valve   TV = Tricuspid Valve
LV = Left Ventricle   RV = Right Ventricle
AV = Aortic Valve   PV = Pulmonic Valve
Z_{SO} = Systemic Characteristic Impedance Z_{PO} = Pulmonic Characteristic Impedance
C_{SA} = Systemic Arterial Compliance C_{PA} = Pulmonic Arterial Compliance
R_{SA} = Systemic Peripheral Resistance R_{PA} = Pulmonic Peripheral Resistance
C_{SV} = Systemic Venous Compliance C_{PV} = Pulmonic Venous Compliance
R_{SV} = Systemic Venous Resistance R_{PV} = Pulmonic Venous Resistance

FIGURE 4.50 Application of the canine left ventricle model to hemodynamic description of the complete human cardiovascular system. *Adapted from [25].*
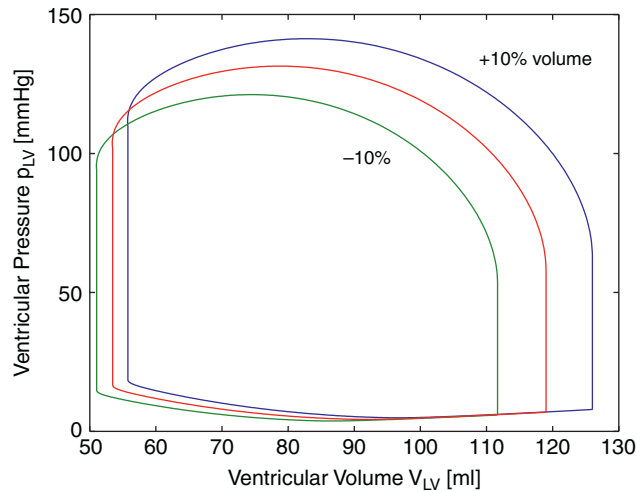

FIGURE 4.51 Left ventricular pressure-volume work loops computed for the complete human circulation model (Figure 4.50) for control (middle curve) and varied preload, achieved by varying total blood volume (5 liters) ±10 percent.

blood volume, 5 liters, by 10 percent. As for the isolated left ventricle model, stroke volume increases with increased preload via the Frank-Starling mechanism, and this increase is moderated by increased end-systolic volume due to increased afterload. Preload may be increased in the natural system by increased central venous pressure, resulting from decreased venous compliance caused by sympathetic venoconstriction, or by augmented
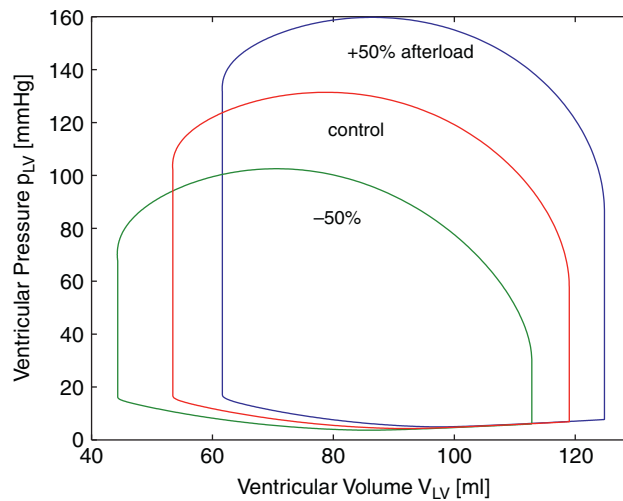
FIGURE 4.52 Left ventricular pressure-volume work loops computed for the complete human circulation model (Figure 4.50) for control and varied afterload, achieved by changing both systemic (R_{SA}) and pulmonic (R_{PA}) peripheral resistances ±50 percent.

venous return due, for example, to gravity via head-down tilt. Preload may also change with total blood volume, which may, for example, decrease as the direct consequence of hemorrhage, or change with renal regulation.

Figure 4.52 shows work loops computed for the left ventricle in the complete circulation model for three different values of afterload, achieved by varying both systemic peripheral resistance, R_{SA}, and pulmonic peripheral resistance, R_{PA}. Stroke volume is inversely related to peripheral resistance, but the Frank-Starling mechanism partially compensates. For increased afterload, smaller SV results in increased filling for the subsequent beat, and this increased EDV moderates the reduction in SV. This compensatory mechanism is more pronounced in the full circulation model than for the isolated left ventricle (Figure 4.49). Afterload commonly increases in the natural system via increased aortic pressure with increased systemic vascular resistance. The latter occurs, for example, when arterial vessel diameter is reduced associated with chronic hypertension. Afterload also increases with aortic valve stenosis, the narrowing of the valve orifice.

The interdependence of preload and afterload is manifested in treatment of heart failure with vasodilator drugs. These drugs decrease afterload, allowing the ventricle to eject blood more rapidly via muscle's force-velocity relation, which increases stroke volume. As SV increases, less blood remains to fill the ventricle for the next beat, but this decrease in EDV is less than the reduction of ESV, resulting in a net increase in stroke volume.

The heart's contractile state may be changed by varying the parameter c in the model (Eq. (4.75)). Figure 4.53 shows left ventricular work loops for such variations in inotropy, executed by changing the contractile parameter c for each of the four heart chambers. Increased inotropy causes an increase in stroke volume, with a decrease in end-systolic volume due to the more strongly contracting heart. End-diastolic volume decreases a small amount
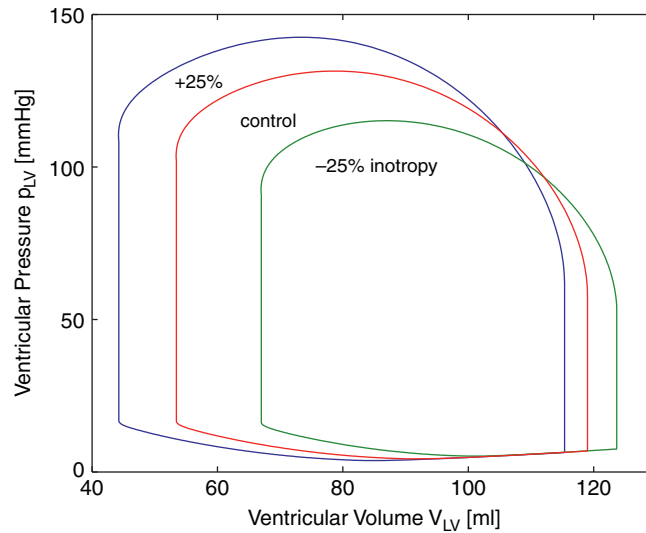
FIGURE 4.53 Left ventricular pressure-volume work loops computed for the complete human circulation model (Figure 4.50) for control and varied inotropy, achieved by changing the contractile parameter c in Eq. (4.75) for each heart chamber ±25 percent.

since the more forcefully ejecting heart leaves less volume available for the subsequent heartbeat. Inotropy is regulated by the autonomic nerves, augmented by sympathetic adrenergic effects of circulating catecholamines, such as epinephrine, the so-called "fight or flight" response to stress. Inotropic drugs used clinically to stimulate the heart in acute and chronic heart failure include digoxin and the beta-adrenoceptor agonists dopamine, dobutamine, epinephrine, and isoproterenol.

The complete circulatory system model may be used to study interactions between left (systemic) and right (pulmonary) circulations. Figure 4.54 shows left and right ventricle work loops for the normal heart ejecting into the normal (control) circulatory system, depicted by solid curves. The right ventricle work loop is smaller, as expected, than the left. Figure 4.54 also shows the same two work loops for a weakened left ventricle (dashed curves). As expected, this left ventricle work loop is diminished in size and shifts to the right on the volume axis. Since the weaker ventricle ejects less blood, more remains to fill the heart more for the subsequent beat (EDV of 192 instead of 119 ml). This increased filling partially compensates for the weakened ventricle via Starling's law (increased pressure for increased filling).

Table 4.5 shows examples of congestive heart failure, resulting from decreases in c for the left ventricle and for the right ventricle. Decreasing left ventricular contractile state to one-third of the control value lowers the left ventricular ejection fraction from 55 to 27 percent, and root aortic pulse pressure decreases from 131/58 to 102/47 mmHg. Left ventricular stroke volume decreases less, from 66 to 53 ml, since it is compensated for by the increased left enddiastolic volume (192 ml) via Starling's law. Decreasing left ventricular contractile state is equivalent to left congestive heart failure. Consequently, pulmonary venous volume increases from 1,540 ml to 2,057 ml (not shown), indicating pulmonary congestion for this case.
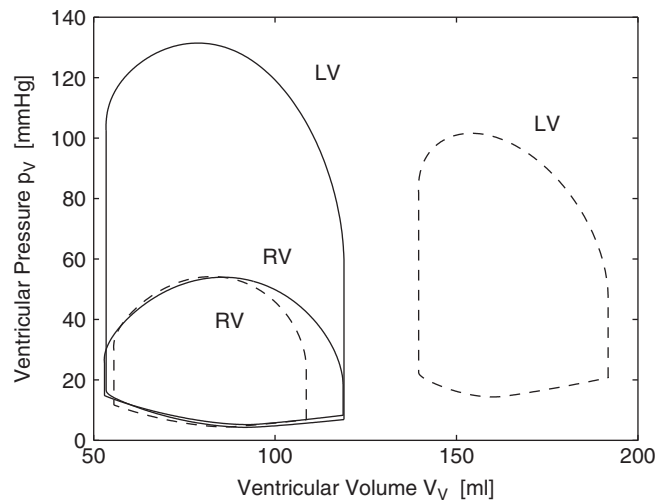
FIGURE 4.54 Computed work loops for the left and right ventricles under control conditions (solid curves) and for the case of a weakened left ventricle (dashed curves).

Similar changes are noted when the right ventricle's contractile state is halved. The right ventricular ejection fraction drops from 55 to 37 percent, root pulmonary artery pulse pressure decreases from 54/18 to 40/15 mmHg, and right stroke volume decreases from 66 to 56 ml, with an increased end-diastolic volume of 153 ml, from 119 ml. Conversely, c can be increased in any heart chamber to depict administration of an inotropic drug. Although not plotted, pressures, flows, and volumes are available at any circuit site, all as functions of time.

In summary, the left ventricle may be described as a dynamic pressure generator. A small number of experimentally derived parameters are sufficient to describe the wide range of observed cardiovascular dynamics. This approach links experiment and theory, leading to new ideas and experiments. It also links underlying muscle dynamics to heart performance. Work is under way to devise a new measure of cardiovascular health using this model.

TABLE 4.5   Cardiovascular Performance for a Normal Heart and for Weakened Left and Right Ventricles

	SV [ml]		EDV [ml]		EF [%]		p_{AO} [mmHg]	p_{PU}
	LV	RV	LV	RV	LV	RV		
Control	66	66	119	119	55	55	131/58	54/18
Weak LV	53	53	192	109	27	49	102/47	54/24
Weak RV	56	56	106	153	53	37	117/54	40/15

Note: SV denotes stroke volume, EDV denotes end-diastolic volume, EF is ejection fraction, and p_{AO} and p_{PU} are root aorta and root pulmonary artery pressures, respectively, for the left (LV) and right (RV) ventricles. Note that SV left and right are equal under all conditions.

The field of biomechanics applies physical principles to living systems using the language of mathematics. Hemodynamics studies the human cardiovascular system, which comprises a complex pump moving complex fluid around an extensive network of complex pipes. In developing hemodynamic principles, experiments and analysis go hand-in-hand, ensuring the validity of principles with experiments and with analysis clarifying, modifying, and often preceding experiments. In this fashion, interpretations of cardiovascular health are further defined.

4.8 EXERCISES

1. Write and evaluate all the vector expressions of Eqs. (4.1) through (4.14) using MATLAB.
2. The measurement error associated with the pointer marker data presented in Example Problem 4.2 is ±0.5 mm in all three coordinate directions. Given the geometry of the pointer in the example problem, what is the measurement error associated with the pointer tip, point T? If you wanted to minimize the measurement error at point T, how would you design the pointer with respect to the distances between markers A and B, and between marker B and the pointer tip T?
3. Repeat Example Problem 4.3 using a z-x-y rotation sequence.
4. Write the free-body diagrams for each of the three orientations of the humerus in Figure 3.36. For a particular load and fixed position, write and solve the equations of static equilibrium.
5. The force plate in Figure 4.11 is 70 cm wide in the x-direction and 80 cm long in the y-direction. At a particular instant of the gait cycle each transducer reads $F_1 = 150$ N, $F_2 = 180$ N, $F_3 = 220$ N, and $F_4 = 210$ N. Compute the resultant force and its location.
6. Solve Example Problem 4.8 for forearm orientations angled θ from the horizontal position. Let θ vary from 0° to 70° down from the horizontal in 5° increments. Using MATLAB, plot the required biceps muscle force F_B for static equilibrium as a function of θ. By how much does this force vary over this range?
7. Repeat Problem 6, this time plotting forces F_A, F_B, and F_C over the same range of angles θ.
8. Considering the previous problem, explain why Nautilus weight machines at the gym use asymmetric pulleys.
9. Solve Example Problem 4.7 using the moment of inertia of the thigh with respect to the knee.
10. For your own body, compute the mass moment of inertia of the body segments: Forearm, Total Arm, Thigh, Foot, and Trunk in Table 4.1 with respect to their centers of mass.
11. Repeat Example Problem 4.9 using a cobalt alloy rod with circular cross-sectional diameter of 10 mm.
12. Write the Simulink models of the three-element Kelvin viscoelastic description and perform the creep and stress relaxation tests, the results of which appear in Figures 4.26 and 4.27.
13. Use the three-element Kelvin model to describe the stress relaxation of a biomaterial of your choice. Using a stress response curve from the literature, find the model spring constants K_1 and K_2, and the viscous damping coefficient β.
14. Write and solve the kinematic equations defining an anatomically referenced coordinate system for the pelvis, $\{\mathbf{e_{pa}}\}$, using MATLAB.
15. Using the kinetic data of Section 4.6.3, compute the instantaneous ankle power of the 25.2 kg patient using MATLAB.

Continued

16. Pelvic obliquity is commonly associated with an angular displacement of the pelvis as seen from the front of the patient and is estimated as the angle formed between the vector from right to left anterior superior iliac spine (ASIS) and the horizon. Given the pelvic position data below, calculate the clinician's estimate of pelvic obliquity. Note: The clinician would be looking down the x-axis of the global coordinate system at the pelvic data in the y-z plane.

Right ASIS	=	$0.400\mathbf{i} + 0.400\mathbf{j} + 0.580\mathbf{k}$ m
Left ASIS	=	$0.390\mathbf{i} + 0.435\mathbf{j} + 0.600\mathbf{k}$ m
PSIS	=	$0.100\mathbf{i} + 0.418\mathbf{j} + 0.820\mathbf{k}$ m

Which Euler angle algorithm, one based on a y-x-z rotation sequence or one based on a z-x-y rotation sequence, would provide a value of pelvic tilt that would best match the clinician's estimate in this case?

17. Given the pelvis and thigh anatomical coordinate systems defined in Example Problems 4.10 and 4.11, compute the pelvis tilt, obliquity, and rotation angles using a z-x-y rotation sequence.

18. Repeat Problem 17 (using a z-x-y rotation sequence) solving for hip flexion/extension, hip abduction/adduction, and internal/external hip rotation. Hint: $\{\mathbf{e_{ta}}\}$ is the triple-primed coordinate system, and $\{\mathbf{e_{pa}}\}$ is the unprimed system in this case.

19. Using MATLAB, determine the effect that a 10 mm perturbation in each coordinate direction would have on ankle power amplitude (Section 4.6.3). Hint: Increase the foot anatomical coordinate system $\{\mathbf{e_{fa}}\}$ by 0.010 m in each direction.

20. Reflective markers placed over the anterior superior iliac spine (ASIS) and the posterior superior iliac spine (PSIS) define the pelvic anatomical coordinate system. An easy mistake to make in the placement of these markers on an overweight or obese subject is to place the ASIS marker(s) at the horizontal level of the ASIS, but not in the pelvic plane, as shown in the figure below. The same type of error can be made with the placement of the PSIS. If the actual pelvic tilt for a patient is 34° and reflective markers are placed in the following pelvic locations relative to the fixed laboratory coordinate system, what is the magnitude of the error in pelvic tilt, if any?
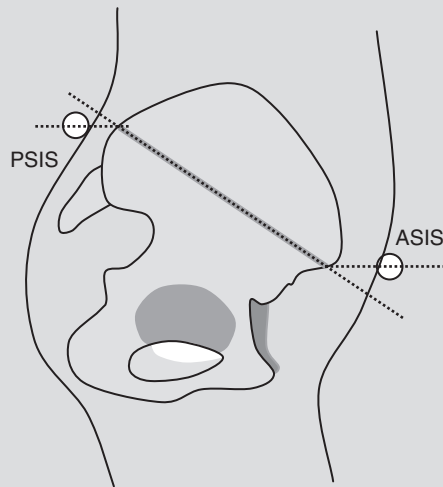
21. Fit the blood rheological data of Example Problem 4.13 to a Casson model and find the yield stress τ_0 for blood.
22. Solve Eq. (4.71) for pressure $p(t)$ when the aortic valve is closed. Using the parameter values in Table 4.4, plot p as a function of time for one heartbeat (t = 0 − 1 sec).
23. Compute isovolumic ventricular pressure $p_v(t)$ for the canine heart with initial volumes $V_v = 30, 40, 50, 60, 70$ ml. Overlay these plots as in Figure 4.41.
24. Write a MATLAB m-file to compute ventricular elastance using Eq. (4.77). Compute and plot $E_v(t)$ for the parameter values in Example Problem 4.15.
25. For the three pressure-volume work loops in Figure 4.52, measure end-diastolic volume EDV, end-systolic volume ESV, stroke volume SV, and ejection fraction EF. Estimate the total mechanical power done by the ventricle in units of watts.

References

[1] R. Baker, Pelvic angles: a mathematically rigorous definition which is consistent with a conventional clinical understanding of the terms, Gait Posture 13 (2001) 1–6.
[2] A.H. Burstein, T.M. Wright, Fundamentals of Orthopaedic Biomechanics, Williams & Wilkins, Baltimore, MD, 1994.
[3] A. Cappozzo, Gait analysis methodology, Hum. Mov. Sci. 3 (1984) 27–50.
[4] K.B. Chandran, S.E. Rittgers, A.P. Yoganathan, Biofluid Mechanics: The Human Circulation, CRC Taylor & Francis Group, Boca Raton, FL, 2007.
[5] R.B.D. Davis III, Musculoskeletal biomechanics: Fundamental measurements and analysis, Chpt. 6 in: J.D. Bronzino (Ed.), Biomedical Engineering and Instrumentation, PWS Engineering, Boston, MA, 1986.
[6] R.B. Davis, S. Õunpuu, D.J. Tyburski, J.R. Gage, A gait analysis data collection and reduction technique, Hum. Mov. Sci. 10 (1991) 575–587.
[7] R. Dugas, A History of Mechanics, Dover Publications, New York, NY, 1988, reprinted from a 1955 text.
[8] R.M. Ehrig, W.R. Taylor, G.N. Duda, M.O. Heller, A survey of formal methods for determining functional joint axes, J. Biomech. 40 (2007) 2150–2157.
[9] R.L. Fournier, Basic Transport Phenomena in Biomedical Engineering, Taylor & Francis, Philadelphia, PA, 1999.
[10] Y.C. Fung, A First Course in Continuum Mechanics, second ed., Prentice-Hall, Englewood Cliffs, NJ, 1977.
[11] Y.C. Fung, Biomechanics: Mechanical properties of living tissues, second ed., Springer-Verlag, New York, NY, 1993.
[12] D.T. Greenwood, Principles of Dynamics, second ed., Prentice-Hall, Englewood Cliffs, NJ, 1988.
[13] A.F. Huxley, Muscle structure and theories of contraction, Prog. Biophys. 7 (1957) 255–318.
[14] A. Kennish, E. Yellin, R.W. Frater, Dynamic stiffness profiles in the left ventricle, J. Appl. Physiol. 39 (1975) 665.
[15] W.R. Milnor, Hemodynamics, second ed., Williams and Wilkins, Baltimore, MD, 1989.
[16] V.C. Mow, W.C. Hayes, Basic Orthopaedic Biomechanics, second ed., Lippencott-Rave, Philadelphia, PA, 1997.
[17] J.P. Mulier, Ventricular pressure as a function of volume and flow, Ph.D. dissertation, Univ. of Leuven, Belgium, 1994.
[18] D.M. Needham, Machina Carnis: The Biochemistry of Muscular Contraction in its Historical Development, Cambridge University Press, Cambridge, U.K., 1971.
[19] B.M. Nigg, W. Herzog, Biomechanics of the Musculo-Skeletal System, third ed., John-Wiley, New York, NY, 2007.
[20] A. Noordergraaf, Hemodynamics, Chpt. 5 in: H.P. Schwan (Ed.), Biological Engineering, McGraw-Hill, New York, NY, 1969.
[21] A. Noordergraaf, Circulatory System Dynamics, Academic Press, New York, NY, 1978.

[22] J.L. Palladino, A. Noordergraaf, Muscle contraction mechanics from ultrastructural dynamics, Chpt. 3 in: G.M. Drzewiecki, J.K.J. Li (Eds.), Analysis and Assessment of Cardiovascular Function, Springer-Verlag, New York, NY, 1998.

[23] J.L. Palladino, A. Noordergraaf, Functional requirements of a mathematical model of the heart, in: Proc. IEEE Eng. Med. Biol. Conf., Minneapolis, MN, 2009, pp. 4491–4494.

[24] J.L. Palladino, J.P. Mulier, A. Noordergraaf, Closed-loop circulation model based on the Frank mechanism, Surv. Math. Ind 7 (1997) 177–186.

[25] J.L. Palladino, L.C. Ribeiro, A. Noordergraaf, Human circulatory system model based on Frank's mechanism, in: J.T. Ottesen, M. Danielsen (Eds.), Mathematical Modelling in Medicine, IOS Press, Amsterdam, Netherlands, 2000, pp. 29–39.

[26] R.J. Roark, Formulas for Stress and Strain, sixth ed., McGraw-Hill, New York, NY, 1989.

[27] C. Singer, E.A. Underwood, A Short History of Medicine, second ed., Oxford Univ. Press, New York, NY, 1962.

[28] H. Suga, K. Sagawa, Instantaneous pressure-volume relationship under various enddiastolic volume, Circ. Res. 35 (1974) 117–126.

[29] E. Weber, B.R. Wagner (Eds.), Handwörterbuch der Physiologie, vol. 3, Vieweg, Braunschweig, 1846.

[30] F.M. White, Fluid Mechanics, sixth ed., McGraw-Hill, New York, NY, 2008.

[31] S. Vogel, Vital Circuits: On Pumps, Pipes, and the Workings of Circulatory Systems, Oxford Univ. Press, New York, NY, 1992.

Suggested Readings

P. Allard, I.A.F. Stokes, J.P. Blanchi (Eds.), Three-Dimensional Analysis of Human Movement, Human Kinetics, Champagne, IL, 1995.

R. Davis, P. DeLuca, Clinical Gait Analysis: Current Methods and Future Directions, in: G. Harris, P. Smith (Eds.), Human Motion Analysis: Current Applications and Future Directions, IEEE Press, Piscataway, NJ, 1996, pp. 17–42.

J.R. Gage, M.H. Schwartz, S.E. Koop, T.F. Novacheck, The Identification and Treatment of Gait Problems in Cerebral Palsy, MacKeith Press, London, U.K., 2009.

W.F. Ganong, Review of Medical Physiology, twenty-second ed., McGraw-Hill, New York, NY, 2005.

J.L. Meriam, L.G. Kraige, Engineering Mechanics, sixth ed., John Wiley, New York, NY, 2008.

W.R. Milnor, Cardiovascular Physiology, Oxford Univ. Press, New York, NY, 1990.

A.D. McCulloch, Cardiac Biomechanics, Chpt. 8 in: D.R. Peterson, J.D. Bronzino (Eds.), Biomechanics Principles and Applications, CRC Taylor & Francis Group, Boca Raton, FL, 2008.

W.W. Nichols, M.F. O'Rourke, McDonald's Blood Flow in Arteries: Theoretical, Experimental and Clinical Principles, third ed., Edward Arnold, London, U.K., 1990.

J. Rose, J.G. Gamble, Human Walking, Lippincott Williams & Wilkins, Philadelphia, PA, 2006.

N. Westerhof, A. Noordergraaf, Arterial Viscoelasticity: A Generalized Model, J. Biomech. 3 (1970) 357–379.

D.A. Winter, Biomechanics and Motor Control of Human Movement, fourth ed., John Wiley, New York, NY, 2009.